Magneto-transport properties of (multilayer) graphene

The lowest Landau level in high magnetic fields

Erik van Elferen

Magneto-transport properties of (multilayer) graphene:
The lowest Landau level in high magnetic fields
Henricus Johannes van Elferen
Thesis Radboud Universiteit Nijmegen - Illustrated
With references - With summary in Dutch
ISBN: 978-94-6191-481-1
Cover: (Multilayer) graphene on a 280 nm thick SiO_2-substrate, the illustration is approximately 1000× magnified. The yellow-black line is a typical HFML-benchmark, the inset of the yellow blocks illustrate the hexagonal lattice of graphene.
Design by the author.

Magneto-transport properties of (multilayer) graphene:

The lowest Landau level in high magnetic fields

Proefschrift

ter verkrijging van de graad van doctor
aan de Radboud Universiteit Nijmegen,
op gezag van de rector magnificus prof. mr. S.C.J.J. Kortmann,
volgens besluit van het college van decanen
in het openbaar te verdedigen op woensdag 9 januari 2013
om 15:30 uur precies

door

Henricus Johannes van Elferen

geboren op 2 april 1985
te Nijmegen

PROMOTOR:	PROF. DR. IR. J. C. MAAN
COPROMOTOR:	DR. U. ZEITLER
MANUSCRIPTCOMMISSIE:	PROF. DR. T.H.M. RASING
	PROF. DR. IR. B.J. VAN WEES (RIJKSUNIVERSITEIT GRONINGEN)
	DR.IR. C.F.J. FLIPSE (TECHNISCHE UNIVERSITEIT EINDHOVEN)

Het werk beschreven in dit proefschrift is uitgevoerd aan de faculteit der Natuurwetenschappen, Wiskunde en Informatica van de Radboud Universiteit Nijmegen en maakt deel uit van het onderzoeksprogramma van de 'Stichting voor Fundamenteel Onderzoek der Materie'(FOM), die financieel gesteund wordt door de Nederlandse Organisatie voor Wetenschappelijk Onderzoek (NWO).

Aan mijn familie

Geduld is zulk een schone zaak,
Om in een moeielijke taak
Zijn doelwit uit te voeren
Hieronymus van Alphen, 1778

Voorwoord

Ruim negen jaar geleden stond ik op de drempel om mij op de Radboud Universiteit Nijmegen in te schrijven voor de studie *Natuur- en sterrenkunde*. De laatste twijfels voor deze keuze werden weggenomen na een bezoek aan de publieke opening (juni 2003) van het HFML, het nieuwe magneten-laboratorium van de Radboud Universiteit. Sindsdien heeft dit laboratorium als een rode draad door mijn studie gelopen. Verschillende natuurkunde-colleges, rondleidingen en afdelingsbezoeken motiveerden mij in 2005 om nader kennis te maken met de mensen in het HFML en mijn Masterstage hier te doen. In het collegejaar 2007-2008 was het zover en bracht ik mijn afstudeerstage tot een goed einde. Bovendien bood het HFML mij de fantastische kans om mij hier persoonlijk verder te ontwikkelen en mijn promotie-onderzoek te gaan doen. Ik ben veel dank verschuldigd voor de kansen, het geduld en de creatieve vrijheid die ik heb gekregen. Deze vier jaren waren zowel werk-inhoudelijk als persoonlijk een weg van zowel hoogte- als dieptepunten. Echter, ik ben enorm trots dat ik jullie de gedrukte versie van dit boekje heb mogen overhandigen.

Al het werk dat ik publiceer in dit proefschrift is slechts een gedeelte van al het werk dat ik de afgelopen jaren heb verricht, en is vaak uitgevoerd door meer dan alleen mijzelf. Ik ben veel dank verschuldigd aan collega's, vrienden en familie die allemaal op hun eigen wijze hebben bijgedragen aan de totstandkoming van dit boekje. Ik maak graag van de gelegenheid gebruik om hier enkele mensen persoonlijk te bedanken.

Allereerst wil ik alle technici in het HFML bedanken voor hun vakkundige kennis van de installatie en het mogelijk maken van alle gewenste experimenten die ik in dit proefschrift presenteer. In het bijzonder wil ik Peter Albers bedanken voor zijn uitmuntende bijdrage aan de totstandkoming van onze eigen kleine cleanroom, ik denk nog vrijwel dagelijks met een brede glimlach terug aan het plakken van de gele raamfolie. Verder wil ik Lijnis bedanken voor zijn toegankelijkheid en vakkundigheid, altijd stond je klaar om een cryostaat voor

mij te plaatsen, een insert te maken of ergens wat extra gaatjes in te boren. Maar natuurlijk wil ik ook alle andere technici bedanken voor hun uitstekende zorg voor de magneten, koelinstallatie en inserts, maar ook voor hun geduld als ik in al mijn enthousiasme iets stuk had gemaakt. Heel veel dank Hung, Frits, Arjen, Jos van Velsen, Harry, Jos Rook en Ramon van Stijn.
Daarnaast wil ik natuurlijk Ine en Martin bedanken. Jullie waren er altijd bij hulp van bestellingen, vertraagde post, problemen met Oracle, en andere bureaucratische vertragingen; jullie hebben ongemerkt veel werk uit handen genomen.

Daarnaast wil ik mijn mede-PhD's, postdocs en studenten bedanken die allemaal op hun eigen manier een bijdrage hebben geleverd, wetenschappelijk dan wel bij de borrels en uitstapjes, nl. Alan, Ali, Alix, Andreas, Andres, Arend, Bhavtosh, Bhawana, Erik Kampert, Esther, Flavio, Francesca, Frank, Frans, Genia, Giorgio, Iris, Janneke, Jeroen, Jos Giesbers, Masoumeh, Laurens, Lyckle, Papori, Peter van Rhee, Ramon Veenstra, Roger, Sjoerd, Steffen, Suruchi, Szymon, Veerendra en Victor. In het bijzonder wil ik Erik Kampert bedanken voor zijn fantastische hulp gedurende mijn afstudeerstage die mij uiteindelijk startklaar hebben gemaakt voor mijn PhD. Andres, I would like to thank you for your never ending support in my office, you really helped me to pull me through the last part of my PhD. Hopefully I will have some more time in future to watch together football matches in the pub. Francesca, thank you for your fruitful time during your internship, I really liked it, I learned a lot of it and it gave me some nice work in this thesis. Laurens, de korte tijd die we samen hebben gewerkt was zeer plezierig. Ik heb met veel plezier mijn thesis even terzijde geschoven om jou op weg te helpen met jouw magnetisatie-metingen, ik ben blij dat het cantilever-project in zo'n goede handen is gekomen. Steffen I would like to thank you for all your positive input, drive to keep going for the papers/thesis, and of course for your excellent work you did for chapter 4. Especially I would like to thank Genia. We started our PhD together, both on graphene, and supposed to work day and night together. I really enjoyed measuring nights together, adjusting the sample angle for hours, discussing moving Landau levels, drawing all scenarios for the density of states, but also spending a nice time outside the lab. Genia, you can say with right that you contributed to the content of this thesis.

Furthermore I had a very pleasant collaboration with the university of Groningen. Alina, already from the first meeting in Bad Honnef I felt that there was growing a good connection between us. I admire your excellent explanation, help and patience in the Nanolab cleanroom. Furthermore we spend long measurement nights together in Nijmegen where we have shared both great results and big disappointments. We both found our way to the finish of this PhD, also you can say with right that you contributed to the content of this thesis. Besides that, I would like to thank everybody of the group of Nanodevices in Groningen for all help and nice evenings out. In particular I am thankfull for giving me the opportunity to use the fantastic equipment and great samples from Groningen.

Verder wil ik graag de groep van Applied Material Science bedanken voor de geboden hulp m.b.t. de opzet van onze clean-room, ik heb veel geleerd van jullie ervaring en gedetailleerd commentaar op de verschillende lithografie procedures. Met name wil ik Peter Mulder bedanken voor de verschillende keren dat je me hebt geholpen met vragen over draadbonders of het ontwerp van de optische maskers.

Ten slotte kom ik toe aan de mensen waaraan ik eeuwig dank ben verschuldigd. Allereerst wil ik Genia nogmaals bedanken, maar nu voor je geduld en liefde in de afgelopen jaren en met name ook voor je enorme steun in de laatste moeilijke maanden. Jouw vechtlust om mijn promotie af te ronden gaf mij de doorslaggevende zet in de goede richting! Verder wil ik Dorine, Harm en Mathijs bedanken voor alle liefde en begrip die ik heb gekregen gedurende deze vier jaar. Ten slotte ben ik veel dank verschuldigd aan mijn vader en moeder. Mama, jij hebt mij leren knokken, moed blijven houden en elke dag opnieuw leren beginnen. Papa, ik ben heel erg trots dat ik jouw optimisme en levensvreugde heb mogen krijgen; dit heeft mij erg geholpen om na een tegenvaller toch positief te blijven. Momenteel gaan we samen door ongekend moeilijke periode, maar niemand neemt ons alle fijne herinneringen af! De afgelopen jaren ben ik er voor jullie allemaal te weinig geweest, altijd was er wel weer een meting, artikel, proposal, etc. dat in de weg stond, maar uiteindelijk was het de moeite waard.

Erik van Elferen (Augustus 2012)

Contents

Chapter 1

Introduction

One of the most versatile elements in nature is carbon. Due to its large variety of electronic bonds it is an essential building block of many molecules, called together the organic chemistry. Already from prehistory days we know carbon, i.e. people were using it to make cave paintings. By drawing with a piece of charcoal they were mechanically breaking off small pieces of carbon, and most ultimately breaking off single sheets of carbon atoms, graphene. Graphene is the building block of the most pure form of carbon, graphite, a 3D-Bernal stacking of carbon. The strong intra-layer binding and the relatively weak inter-layer binding makes it easy to remove individual layers of graphite. Therefore artists of the prehistory were unintentionally the founders of graphene, but it took 40.000 more years for mankind to realize this.

In 1947 it was P.R. Wallace who theoretically predicted the existence of graphene and calculated its bandstructure.[1] Already then P.R. Wallace predicted graphene to behave as zero gap semiconductor where the conduction band and valence band touch in a diabolo shape. In the following 50 years graphene got much attention as the building block of folded graphene (1985, the buckyball[2]) and rolled graphene (1991, carbon nanotubes[3]). However, it took 57 more years to isolate a freestanding single sheet of graphene. In 2004 K.S. Novoselov and A.K. Geim from the University of Manchester managed to mechanically cleave graphite with a piece of Scotch tape until a single layer remained.[4]

Geim & Novoselov's first experimental results demonstrate that graphite of several layers thick can be used to build an ambipolar field effect transistor.[4] Experimentally it was shown that charge carriers in a single sheet of graphene behave as massless particles.[5] This causes the charge carriers to obey relativistic physics for massless Dirac fermions. This observation made graphene fundamentally unique and it became the rising star of the 21st century's physics.[6] The physical outstanding properties also attracted attention of the high tech industry, which has started in the last 8 years wafer scale production of graphene.[7] Hot industrial prospects are rising on the horizon by using graphene in flexible LCD displays (Samsung),[7] high frequency chips (IBM),[8] and many more applications. The discovery of graphene, the proof of its wide range of tremendous properties, and the promising industrial future were reason to award in 2010 the Nobel Prize of Physics to A.K. Geim and K.S. Novoselov.[9]

This thesis starts with a description of the general electronic properties of graphene [chapter 2], followed by the technology how to build the graphene based devices used in this thesis [chapter 3]. In these chapters we focus our attention on the behavior in magnetic fields, which forms a good basis for further understanding of the performed scientific research in chapters 4-7.
In 2007 it was demonstrated that already at room temperature we observe field induced quantized energy states.[10] This makes graphene unique in comparison to conventional semiconductors, which all need cryogenic temperatures and high magnetic fields to observe fully quantized energy states. In chapter 4 we study in more detail the appearance of these quantized energy-states by analyzing the transition from the classical to the quantum mechanical regime. In particular we study the nature of the charge neutrality point (CNP): the point at which theoretically no free charge carriers are present in the graphene. However, we will show experimentally that the transport around the CNP is dominated by the coexistence of holes and electrons, rather than a point without electrons and holes.

The study of single layer graphene is the first step in the understanding of the electronic behavior of bulk graphite. In chapter 2 we discuss the consequences to the electronic properties when adding an additional layer and creating bilayer graphene.
Further understanding of the magnetic properties in graphene and its multilayer-variants is limited by the maximum applied magnetic fields and the sample quality. Experimentally it is shown that the conductivity in pure bulk graphite is two orders of magnitude higher than in the standard graphene-devices we obtained, which suggests the possibilities to improve the electronic mobility at least by two orders of magnitude. The conductance properties are mainly limited by the scattering due the substrate and/or impurities.[11] In order to improve the sample quality the underlying substrate SiO_2 is replaced by a more suitable substrate,[12] or is even fully removed.[13]

The combination of high quality devices and high magnetic fields opens new opportunities to study the quantized energy states from lower fields and offers a more conclusive study of the manybody interactions in the graphene itself, e.g. displaying fractional quantum Hall effect,[14–16] broken symmetry states,[17] and a magnetic field induced insulating phase.[15,17] In chapters 5-7 we will study the intrinsic properties of high quality suspended bi- and tri-layer graphene in high magnetic fields. In particular in chapter 5 we study the broken symmetry states in the lowest Landau level of suspended bilayer graphene. The application of a perpendicular magnetic field resolves the full eightfold degenerated lowest Landau level, and shows a field induced insulating phase at the CNP. In chapter 6 we move our attention to another scenario where a suspended bilayer graphene is showing a diverging resistance at the CNP for zero magnetic field, which points to the formation of a gapped state. We will study in further detail the evolution of this gapped state by performing tilted magnetic field experiments. Finally in chapter 7 we study the lowest Landau level of trilayer graphene, showing for low fields a twelvefold degenerated lowest Landau level, which for high magnetic fields fully breaks into twelve individual energy levels. All these results provide a further understanding of the manybody phenomena present in (multilayer) graphene, and make an initial step towards the understanding of the behavior in bulk graphite.

References

[1] P. R. Wallace, “The Band Theory of Graphite”, *Physical Review* **71**, 622–634 (1947).

[2] H. W. Kroto, J. R. Heath, S. C. O’Brien, R. F. Curl, and R. E. Smalley, “C60: Buckminsterfullerene”, *Nature* **318**, 162–163 (1985).

[3] S. Iijima, “Helical microtubules of graphitic carbon”, *Nature* **354**, 56–58 (1991).

[4] K. S. Novoselov, A. K. Geim, S. V. Morozov, D. Jiang, Y. Zhang, S. V. Dubonos, I. V. Grigorieva, and A. A. Firsov, “Electric field effect in atomically thin carbon films”, *Science* **306**, 666–669 (2004).

[5] K. S. Novoselov, A. K. Geim, S. V. Morozov, D. Jiang, M. I. Katsnelson, I. V. Grigorieva, S. V. Dubonos, and A. A. Firsov, “Two-dimensional gas of massless Dirac fermions in graphene”, *Nature* **438**, 197–200 (2005).

[6] A. K. Geim and K. S. Novoselov, “The rise of graphene”, *Nature Materials* **6**, 183–191 (2007).

[7] S. Bae, H. Kim, Y. Lee, X. Xu, J.-S. Park, Y. Zheng, J. Balakrishnan, T. Lei, H. Ri Kim, Y. I. Song, Y.-J. Kim, K. S. Kim, B. Ozyilmaz, J.-H. Ahn, B. H. Hong, and S. Iijima, “Roll-to-roll production of 30-inch graphene films for transparent electrodes”, *Nature Nanotechnology* **5**, 574–578 (2010).

[8] Y.-M. Lin, A. Valdes-Garcia, S.-J. Han, D. B. Farmer, I. Meric, Y. Sun, Y. Wu, C. Dimitrakopoulos, A. Grill, P. Avouris, and K. A. Jenkins, “Wafer-Scale Graphene Integrated Circuit”, *Science* **332**, 1294–1297 (2011).

[9] The 2010 Nobel Prize in Physics - Press Release

[10] K. S. Novoselov, Z. Jiang, Y. Zhang, S. V. Morozov, H. L. Stormer, U. Zeitler, J. C. Maan, G. S. Boebinger, P. Kim, and A. K. Geim, “Room-Temperature Quantum Hall Effect in Graphene”, *Science* **315**, 1379 (2007).

[11] J.-H. Chen, C. Jang, S. Xiao, M. Ishigami, and M. S. Fuhrer, “Intrinsic and extrinsic performance limits of graphene devices on SiO_2”, *Nature Nanotechnology* **3**, 206–209 (2008).

[12] C. R. Dean, A. F. Young, I. Meric, C. Lee, L. Wang, S. Sorgenfrei, K. Watanabe, T. Taniguchi, P. Kim, K. L. Shepard, and J. Hone, "Boron nitride substrates for high-quality graphene electronics", *Nature Nanotechnology* **5**, 722–726 (2010).

[13] K. I. Bolotin, K. J. Sikes, Z. Jiang, M. Klima, G. Fudenberg, J. Hone, P. Kim, and H. L. Stormer, "Ultrahigh electron mobility in suspended graphene", *Solid State Communications* **146**, 351–355 (2008).

[14] K. I. Bolotin, F. Ghahari, M. D. Shulman, H. L. Stormer, and P. Kim, "Observation of the fractional quantum Hall effect in graphene", *Nature* **475**, 196–199 (2011).

[15] X. Du, I. Skachko, F. Duerr, A. Luican, and E. Y. Andrei, "Fractional quantum Hall effect and insulating phase of Dirac electrons in graphene", *Nature* **462**, 192–195 (2009).

[16] C. R. Dean, A. F. Young, P. Cadden-Zimansky, L. Wang, H. Ren, K. Watanabe, T. Taniguchi, P. Kim, J. Hone, and K. L. Shepard, "Multicomponent fractional quantum Hall effect in graphene", *Nature Physics* **7**, 693696 (2011).

[17] B. E. Feldman, J. Martin, and A. Yacoby, "Broken-symmetry states and divergent resistance in suspended bilayer graphene", *Nature Physics* **5**, 889–893 (2009).

Chapter 2

Theoretical aspects of graphene and its magnetotransport properties

Abstract

We present the basic electronic properties of a single sheet of graphene and explain why the charge carriers in graphene behave as massless relativistic fermions and demonstrate that magnetic fields are a powerful tool to study its energy levels. Additionally we review the change in the band-structure when we stack two layers of graphene, bilayer graphene, and make an initial step towards the understanding of the properties of graphite.

2.1 Introduction

Carbon is a very versatile element and is found in many different chemical compounds due the ability to form single, double, and triple bonds. Carbon is the building block of carbon-chains, carbon-rings, and its most stable form graphite, a 3D-Bernal stacking of carbon-atoms. Graphite is formed by the reduction of other sedimentary carbon compounds under high pressure conditions (1500 bar) and temperatures exceeding 200 °C. Under these conditions either diamond-structures or graphite are formed. However, the slightly bigger binding energy of graphite makes it the groundstate (7.349 eV/atom for diamond and 7.374 eV/atom for graphite). In the last decades several allotropes of carbon-atoms have been studied and identified, ranging from graphite (3D) to carbon-nanotubes[1] (1D) to buckyballs[2] (0D). The missing piece is a single layer of graphite (2D), graphene,[3] which is in fact the building block of graphite (piled layers of graphene), carbon nanotubes (rolled graphene), and buckyballs (folded graphene). Long time one thought that the pure graphene as a free-standing object does not exist, as it was expected to be thermodynamically unstable.[4] However in 2004 this was proven to be incorrect by the experimental observation of a single sheet of graphene.[5]

In graphite the atoms are bound in a hexagonally shaped lattice. The binding of the carbon-atoms in the (x,y)-plane is much stronger than the weakly van der Waals coupling between the two planes. Therefore one can use graphite as the basis of a pencil to use as a writing tool, the individual carbon-layers remove easily. The removal of these separate layers can be done more accurately by mechanical cleavage of the graphite with a piece of Scotch-tape,[5] in more detail discussed in section 3.3. In this chapter we will have a closer look at the band-structure of graphene and the implications for the conduction properties [section 2.2], in particular for experiments in magnetic fields [section 2.4.2]. Besides the study of the charge carriers in a single layer of graphene in section 2.3 we make an initial step towards the understanding of graphite by studying the band-structure of bilayer graphene and its magnetotransport-properties [section 2.4.3].

2.2 Band-structure of graphene

In graphene the carbon-atoms are bond in a sp^2-hybridization, which means that one s-orbital is hybridized with two p-orbitals. The sp^2-hybrids provide the binding between neighboring atoms. This makes the carbon-atoms ordered in a hexagonal lattice (or honeycomb lattice) with each carbon-atom bond to three neighboring carbon-atoms spaced by $a_0 = 1.42$ Å. The honeycomb lattice is not

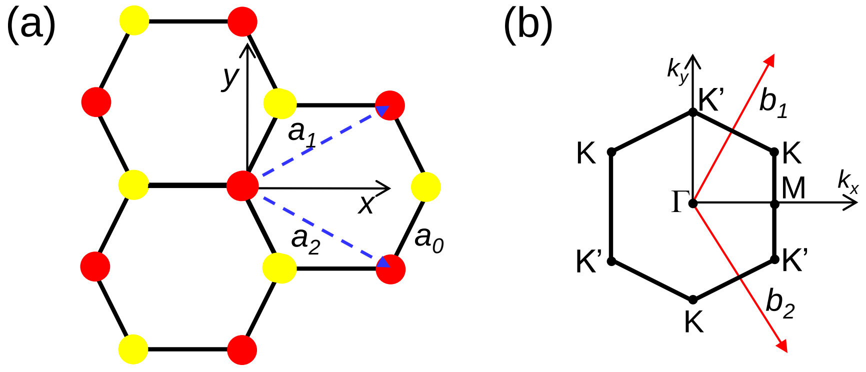

Figure 2.1: *(a) Hexagonally ordered graphene-lattice in the xy-plane with carbon-atoms spaced by a_0 and described by the primitive lattice vectors a_1 and a_2. The red and yellow carbons-atoms mark the two different trigonal sublattices that form the complete graphene-lattice. (b) Hexagonal Brillouin zone of graphene spanned by the lattice points Γ, K, and K' and by the reciprocal lattice vectors b_1 and b_2.*

a Bravais lattice, but it can be considered as a Bravais lattice with two-atom basis. These two atoms can be described in real space by two primitive lattice vectors $a_1 = \frac{a_0}{2}\left(3, \sqrt{3}\right)$ and $a_2 = \frac{a_0}{2}\left(3, -\sqrt{3}\right)$ [see Fig. 2.1(a)]. Consequently the lattice could be also considered as two triangular sublattices and demonstrate the existence of two sublattices [the yellow and red atoms in Fig. 2.1(a)]. The reciprocal vectors are: $b_1 = \frac{2\pi}{a_0}\left(\frac{1}{3}, \frac{1}{\sqrt{3}}\right)$ and $b_2 = \frac{2\pi}{a_0}\left(\frac{1}{\sqrt{3}}, -\frac{1}{\sqrt{3}}\right)$. Also in momentum space these vectors b_1 and b_2 describe a hexagonal honeycomb lattice and span the edge of the Brillouin zone Γ-K-K' [see Fig. 2.1(b)]. The two characteristic points K and K' describe the two points on the Bruillouin zone that correspond to the two sublattices. These two inequivalent corners at the Bruillouin zone are termed valleys.

Within a first order approximation of the tight-binding approach^6 the dispersion relation is calculated to be as Eq. (2.1). Here E_+ and E_- correspond to the conduction and valence bands respectively.

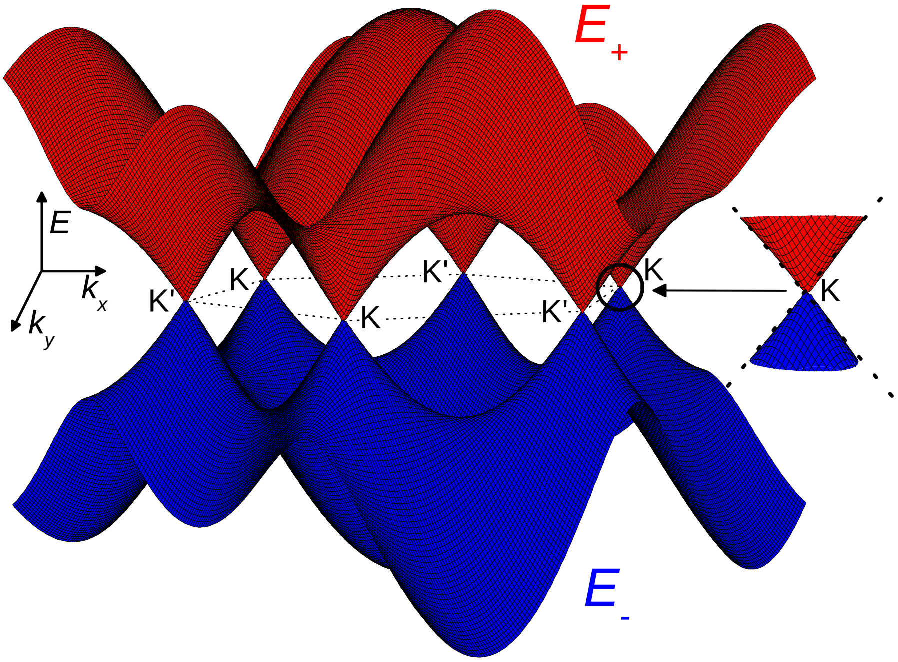

Figure 2.2: *The bandstructure of graphene, plotted are the conduction band* E_+ *and the valence band* E_- *in the momentum-space* (k_x,k_y) *determined by Eq. (2.1). Near the K(K')-points the conduction- and valence-band are touching each other [see right inset].*

$$E_\pm(k_x,k_y) = \pm\gamma_0\sqrt{3+4\cos\left(\frac{3k_xa_0}{2}\right)\cos\left(\frac{\sqrt{3}k_ya_0}{2}\right)+2\cos\left(\sqrt{3}k_ya_0\right)} \tag{2.1}$$

Here $\gamma_0 \approx 3.2$ eV is the nearest neighbor interaction, the interaction between two neighboring carbon-atoms. Fig. 2.2 shows the dispersion over the complete Brillouin zone. Near the K(K')-points the conduction and the valence band touch each other resulting in the typical conical dispersion in the (k_x,k_y)-space. The linear dependence of the dispersion around the K(K')-points is mathematically described by Eq. (2.2).

$$E_\pm = \pm\hbar\upsilon_F\,|q| \tag{2.2}$$

Here υ_F is the Fermi velocity $\frac{\sqrt{3}a_0}{2\hbar}\gamma_0 \approx 10^6$ m/s and $\mathbf{q} = \mathbf{k}\text{-}\mathbf{K}$ the wavevector that describes the linear dispersion near the K(K')-points [see dashed lines near the K-point, right inset Fig. 2.2].

In conventional semiconductors the conduction and the valence band are spaced by a gap and the dispersion near the bandgap depends quadratically on the momentum, $E(\mathbf{k}) = \frac{\hbar^2 k^2}{2m}$. In contrast to the quadratic dispersion of a conventional semiconductor (where $\upsilon_F = \frac{1}{\hbar}\frac{\delta E}{\delta k} = \frac{\hbar k_F}{m}$ and depends on E) the Fermi velocity υ_F of Eq. (2.2) is independent of the momentum $\mathbf{q}$. An important implication of the absence of a momentum-dependence of the Fermi-velocity is that the charge carriers have a zero effective mass[3,7] and makes the charge carriers behave as massless Dirac fermions and obey relativistic physics. The consequence is that fermions obey the relativistic variant of the Schrödingers equation, the Dirac-Weyl equation with the Hamiltonian of Eq. (2.3).

$$\hat{\mathbf{H}}_{SLG} = \upsilon_F \begin{pmatrix} 0 & p_x - ip_y \\ p_x + ip_y & 0 \end{pmatrix} = \upsilon_F \sigma \cdot \hat{\mathbf{p}} \tag{2.3}$$

Here σ are the spin Pauli matrices and $\hat{\mathbf{p}}$ the particle momentum. The use of the Dirac-Weyl Hamiltonian has also important consequences for the magneto-transport properties which we will discuss in more detail in section 2.4.

The linear dispersion near the K(K')-points indicates that for an uncharged system the zero Fermi energy E_F lies exactly in between the two cones. In this case there are effectively no free electrons or holes in the system. By increasing (decreasing) the Fermi energy we can induce more electrons (holes) in the graphene; experimentally achieved by capacitively inducing electrons (holes) in the sample [described in section 3.2]. In Fig. 2.3 we show how the conductance G of the sample decreases when we move from a hole-doped system (negative electron concentration n) to zero concentration ($n = 0$) and start to increase again when electrons are induced (positive n) in the sample.

From the data in Fig. 2.3 we extract the mobility μ, which gives an estimation about the free path length of charge carriers in the sample. We calculate the mobility by using the Drude model.[8]

$$\mu = \frac{1}{e}\frac{L}{w}\frac{\mathrm{d}G}{\mathrm{d}n} \tag{2.4}$$

Here is e the electron charge, G the conductance, n the charge carrier concentration, L the length of the sample, and w the width of the sample (L/w is also called the aspect ratio). By analyzing the slope $\frac{\mathrm{d}G}{\mathrm{d}n}$ at a concentration $n = \pm 5 \cdot 10^{16}$ m^{-2} we find a mobility $\mu = 0.6$ m^{2}V^{-1}s^{-1} for the sample shown

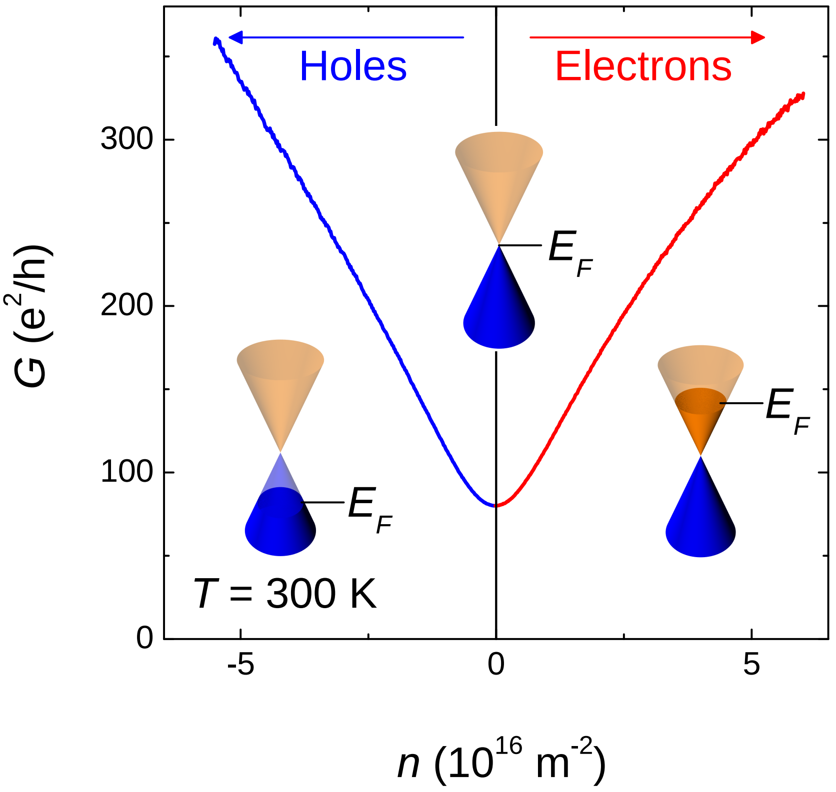

Figure 2.3: *Measured conductance G for a smooth change from hole-doped system (negative charge carrier concentration n), via undoped ($n = 0$) to electron doped (positive n). The insets show the change of the Fermi-energy position E_F in the conical dispersion to achieve a hole-doped system ($E_F < 0$), non-doped system ($E_F = 0$), or electron doped system ($E_F > 0$).*

in Fig. 2.3, which is comparable to the mobility of bulk Silicon[9,10] at room temperature. Higher quality devices (read: higher mobilities) were obtained by replacing the substrate by hexagonal boron nitride, here the mobility can go up to $\mu = 10$ m^{2}V^{-1}s^{-1},[11] or by suspending the graphene from the substrate,[12] e.g. underetching the substrate to make it fully freestanding [see section 3.6 for more technical details].

2.3 Bandstructure of bilayer graphene

The peculiar behaviour of the electronic transport of a single sheet of graphene is caused by the linear crossing of the valence and conduction band at the K(K')-points. The electronic transport in graphite is characterized by a non-linear dispersion,[13] meaning in graphite the charge carriers do not behave as massless Dirac-fermions. In this section we make an initial step towards the further understanding of the transport phenomena by stacking two layers of graphene, bilayer graphene, and study the theoretical consequences to the behavior of the charge carriers.

Bilayer graphene is a stacking of two layers of graphene energetically most favorable piled in the so-called AB-stacking,[14] shown in Fig. 2.4(a). The AB-stacking means that the top layer is shifted in the xy-plane by $\frac{a_0}{2}(\sqrt{3}, 1)$ with respect to the bottom layer. This shift is shown in Fig. 2.4(a) where we indicate with the dashed lines the projection of the top layer on the bottom layer. Here the carbon-atoms of the first sublattice (yellow atoms) are centered in the middle of the hexagon of the bottom layer, while the carbon-atoms of the second sublattice (red atoms) are lying on top of the atoms of the first sublattice (yellow atoms) in the bottom layer. The coupling is dominated by the coupling γ_1 between the two nearest neighbors from the two layers. γ_2 and γ_3 describe the coupling between the more distant atoms [see Fig. 2.4(a)].

Other stacking orders than the AB-stacking are energetically unfavorable and are barely observed in high quality graphite. This type of non-trivial stacking can only be obtained by folding graphene manually or aligning two individual graphene-flakes on top of each other, in literature known as double-layer graphene or twisted graphene.[15–17] Such a twisted graphene is so far seldomly explored by scientists since it is much more complicated to control the production and the orientation of the layers. However, new experimental techniques in graphene mass production[18,19] and the micromechanical alignement of graphene-flakes[11] will open a complete new field of research in the near future.[20] In this thesis we will focus our attention on AB-stacked bilayers, which we will introduce in more detail below.

We use again the tight-binding approach[14] to determine the exact shape of the dispersion relation close to the K(K')-points. In order to do this we use the new form of the Hamiltonian in Eq. (2.5) and obtain the eigenenergies of Eq. (2.6).

$$\hat{\mathbf{H}}_{BLG} = \frac{1}{2m^*}\begin{pmatrix} 0 & (p_x - ip_y)^2 \\ (p_x + ip_y)^2 & 0 \end{pmatrix} \tag{2.5}$$

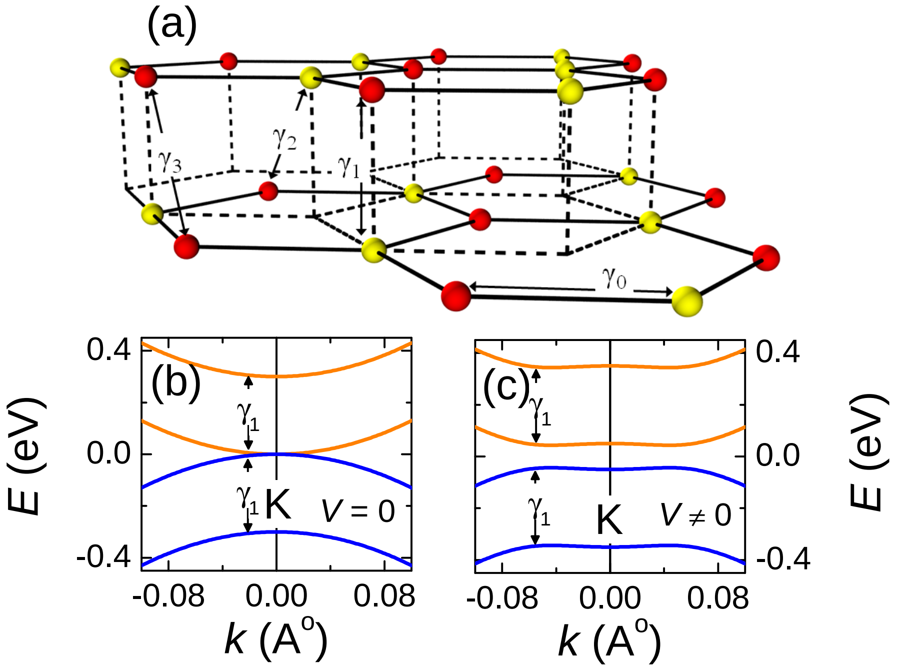

Figure 2.4: *(a) Two AB-stacked layers of graphene, bilayer graphene, with coupling constants* γ_1*,* γ_2*, and* γ_3*. The dashed line represent the projection of the shifted top layer on the bottom layer. (b) The dispersion close to the K(K')-points with an external potential* $V = 0$*. Formation of four subbands: inner and outer subband are spaced* γ_1 *and inner subbands touch each other at the K(K')-points. (c) The dispersion close to the K(K')-points for an external potential* $V \neq 0$*, a gap at* $k = \pm\sqrt{2}V/\upsilon$ *opens close to the K(K')-points.*

$$E_{\pm}(k) = \mp\frac{\gamma_1}{2} \pm \sqrt{\frac{\gamma_1^2}{4} + \hbar^2\upsilon^2k^2} \tag{2.6}$$

Here $\upsilon = \frac{\sqrt{3}a_0}{2\hbar}\gamma_0$ is the Fermi velocity in single layer graphene, and γ_1 the coupling between the two layers, p_x and p_y are the momenta and m^* the effective mass of the charge carriers. The two $\pm$-signs are an indication that both the valence and conduction band consist of two subbands, illustrated in Fig. 2.4(b). For $\gamma_1 << \hbar\upsilon k$ Eq. (2.6) reduces to the linear dispersion of a single layer in Eq. (2.2). However, in an AB-stacked bilayer $\gamma_1 \approx 0.4$ eV and therefore we have $\gamma_1 \approx \mathcal{O}(\hbar\upsilon k)$. With this we simplify Eq. (2.6) to Eq. (2.7) which shows in the low energy approximation a parabolic dispersion near the K(K')-points.

$$E_{\pm}(k) = \mp\frac{\gamma_1}{2} \pm \left(\frac{\gamma_1}{2} + \frac{\hbar^2 \upsilon^2 k^2}{4\gamma_1}\right) = \pm\frac{\hbar^2 \upsilon^2 k^2}{4\gamma_1} \pm \left\{ \begin{array}{ll} \gamma_1 & \text{outer bands} \\ 0 & \text{inner bands} \end{array} \right. \tag{2.7}$$

Here we recognize four different bands from which the two inner bands touch each other at the K(K')-points, while the two outer bands are spaced $2\gamma_1$ [see Fig. 2.4(b)].

Subsequently we introduce a potential difference V between the top and bottom layer, causing the top and bottom layer unequally charged. This is achieved by applying an external electric field,[21] or dopants on the sample.[22] The additional potential V causes a reconstruction of the bandstructure.

$$E_{\pm}(k)^2 = V^2 + \hbar^2 \upsilon^2 k^2 + \frac{\gamma_1^2}{2} \pm \sqrt{4V^2 \hbar^2 \upsilon^2 k^2 + \gamma_1^2 \hbar^2 \upsilon^2 k^2 + \frac{\gamma_1^4}{4}} \tag{2.8}$$

Here V is the potential difference between the top and bottom layer, υ the Fermi velocity of single layer graphene, γ_0 the coupling between two carbon-atoms in the (x,y)-plane, and γ_1 the coupling between the two layers. We now use that $\gamma_1 >> \hbar \upsilon k$, which reduces Eq. (2.8) to Eq. (2.9).

$$E_{\pm}(k)^2 = V^2 + \hbar^2 \upsilon^2 k^2 + \frac{\gamma_1^2}{2} \pm \frac{\gamma_1^2}{2}\left(1 + \left(\frac{4V^2}{\gamma_1^2} + 1\right)\frac{2\hbar^2 \upsilon^2 k^2}{\gamma_1^2}\right) \tag{2.9}$$

For a bilayer graphene at zero electric field, the potential V is negligible ($V \approx 0$) and Eq. (2.9) reduces to Eq. (2.7). In Fig. 2.4(c) we show the behavior of the bandstructure of a bilayer with $V \neq 0$ near the K(K')-points where the inner bands do not touch anymore and the opening of a gap at $k^2 \approx 2V^2/\upsilon^2$ appears. This gap is experimentally acchieved by applying an external potential V to the bilayer with a topgate,[21] but can also appear under influence of local doping.[22] The exact groundstate of bilayer graphene is under debate,[23, 24] which we will discuss in more detail in chapter 6, supported by experiments on a suspended bilayer graphene sample.

2.4 Magnetotransport experiments on single and bilayer graphene

By applying a perpendicular magnetic field $\mathbf{B} = (0, 0, B)$ to a standard two dimensional electron system the charge carriers in the classical regime feel a Lorentz-force $\mathbf{F_L} = \mathbf{qv} \times \mathbf{B}$ perpendicular to the magnetic field $\mathbf{B}$ and the current $q\mathbf{v}$ ($\mathbf{F_L} \perp \mathbf{B}$ and $\mathbf{F_L} \perp \mathbf{v}$). This force has an opposite direction for holes and electrons due to their opposite sign of the charge ($q = \pm e$). The charge separation causes a voltage drop across the sample, the Hall-voltage V_H. This Hall-voltage is directly proportional to the applied magnetic field B and inversely proportional to the charge carrier concentration n.

$$V_H = \frac{BI}{ne} \tag{2.10}$$

The Hall resistance can be formally determined as: $R_{xy} = \frac{V_H}{I} = \frac{B}{ne}$. By cooling down the sample to cryogenic temperature we observe that charge carriers follow closed cyclotron orbits. The radius of these orbits is quantized by an integer number of wavelengths that fit into the orbit. This quantizes the kinetic energy of the charge carriers and forms so-called Landau levels. In 1980 Klaus von Klitzing demonstrated[25] that these Landau levels result in the observation of the quantum Hall effect (QHE). In this section we will discuss the formation of Landau levels and the appearance of QHE in a conventional semiconductor [susbsection 2.4.1], in graphene [subsection 2.4.2], in bilayer graphene [subsection 2.4.3], and the peculiar differences between them.

2.4.1 Conventional semiconductor

The Landau levels in a conventional semiconductor are determined by the Schrödinger equation $\hat{H}\psi = E\psi$. Here $\hat{H}$ is the Hamiltonian, ψ the wavefunction and E the corresponding eigenenergy. The momentum-operator in a magnetic field is described by the spinless gauge transformation in Eq. (2.11).

$$\hat{\mathbf{p}} \rightarrow \hat{\mathbf{p}} - e\hat{\mathbf{A}} \tag{2.11}$$

Here $\hat{\mathbf{p}} = p_x - i \cdot p_y$ is the momentum operator, and $\hat{\mathbf{A}}$ the vector potential. The Hamiltonian has the form $\hat{\mathbf{H}} = \frac{(\hat{\mathbf{p}} - e\hat{\mathbf{A}})^2}{2m^*}$ and has an equivalent solution as the harmonic oscillator with equidistant Landau levels $E_{\mathcal{N}}$.

$$E_{\mathcal{N}} = \left(\mathcal{N} + \frac{1}{2}\right)\frac{\hbar eB}{m^*} \tag{2.12}$$

Here $\mathcal{N} = 0, 1, 2, ...$ is the Landau level index, B the magnetic field, and m^* the cyclotron effective mass of the charge carriers. All Landau levels $E_{\mathcal{N}}$ are equidistant spaced with $\Delta E = E_{\mathcal{N}+1} - E_{\mathcal{N}} = \frac{\hbar eB}{m^*}$.

2.4.2 Single layer graphene

In contrast to the parabolic dispersion of a conventional semiconductor in graphene the conduction and valence band touch each other at the K(K')-points [see section 2.2], forming a linear dispersion. In the presence of a magnetic field we can write the Hamiltonian $\hat{\mathbf{H}}_{\mathbf{SLG}}$ using the transformation in Eq. (2.11).

$$\hat{\mathbf{H}}_{\mathbf{SLG}} = \upsilon_F \begin{pmatrix} 0 & p_x - ip_y + ixeB \\ p_x + ip_y - ixeB & 0 \end{pmatrix} = \upsilon_F \sigma \cdot \hat{\mathbf{p}} \tag{2.13}$$

This leads to a ladder of eigenenergies $E_{\mathcal{N}}$, given by Eq. (2.14).

$$E_{\mathcal{N}} = \pm\hbar\upsilon_F \sqrt{\frac{2eB}{\hbar\upsilon_F}} \sqrt{\mathcal{N} + \frac{1}{2} \pm \frac{1}{2}} = \pm\hbar\omega_c \sqrt{\mathcal{N} + \frac{1}{2} \pm \frac{1}{2}} \text{ for } \mathcal{N} = 0, 1, 2, ... \tag{2.14}$$

We define $\omega_c = \sqrt{2}\frac{\upsilon_F}{l_B}$, the cyclotron frequency, with the magnetic length $l_B = \sqrt{\frac{\upsilon_F}{eB}}$, υ_F the Fermi velocity, and $\mathcal{N}$ the Landau level index. Due to the square root dependence of the level energies on $\mathcal{N}$ the Landau levels in graphene are not equidistantly spaced, but getting more densely packed for increasing $\mathcal{N}$, which is qualitatively shown in Fig. 2.5(a). Additionally, an extra $\pm\frac{1}{2}$ appears, compared to the conventional Landau level quantization as $\left(\mathcal{N} + \frac{1}{2}\right)$. This $\pm\frac{1}{2}$ factor comes from the so-called chirality, which is a degree of freedom taking into account the two different sublattices of the honeycomb lattice. It acts analogously to magnetic spin and is referred as pseudospin. This degree of freedom has its origin in the crossing of the linear bands of the two sublattices, so that electrons with energy E moving in positive direction belong to the same energy bands as holes with energy $-E$ moving in the opposite direction. Therefore electrons and holes owing opposite chirality. Unlike conventional Landau level quantization, presence of the pseudospin leads to half-integer quantization and therefore appearing of the zero energy Landau level. Spin and valley degeneracy make each Landau level four-fold degenerate.

From here we define $N = \mathcal{N} + \frac{1}{2} \pm \frac{1}{2}$, which quantitatively describes all possible energies $\mathcal{N}^{\pm}$, where the $\pm$-sign corresponds to the chirality. In Fig. 2.5(b) we show the energy levels at $N = 0$ (0^-), 1 $(0^+$ or $1^-)$, 2 $(1^+$ or $2^-)$, 3 $(2^+$ or $3^-)$, ... scaling with the square root of the magnetic field B. The highest energy levels E_N are occupied until the Fermi-energy E_F, subsequently followed by the occupation of the lower lying energy E_{N-1}, etc. The bold line in Fig. 2.5(b) shows for a given E_F at zero B the occupation of the different Landau levels: by increasing the magnetic field we fully occupy the energies which cross the dashed line of the Fermi energy and additionally fill up partially the next energy state. The filling of Landau levels can be described by the filling factor $\nu = \frac{n}{eB/h}$.

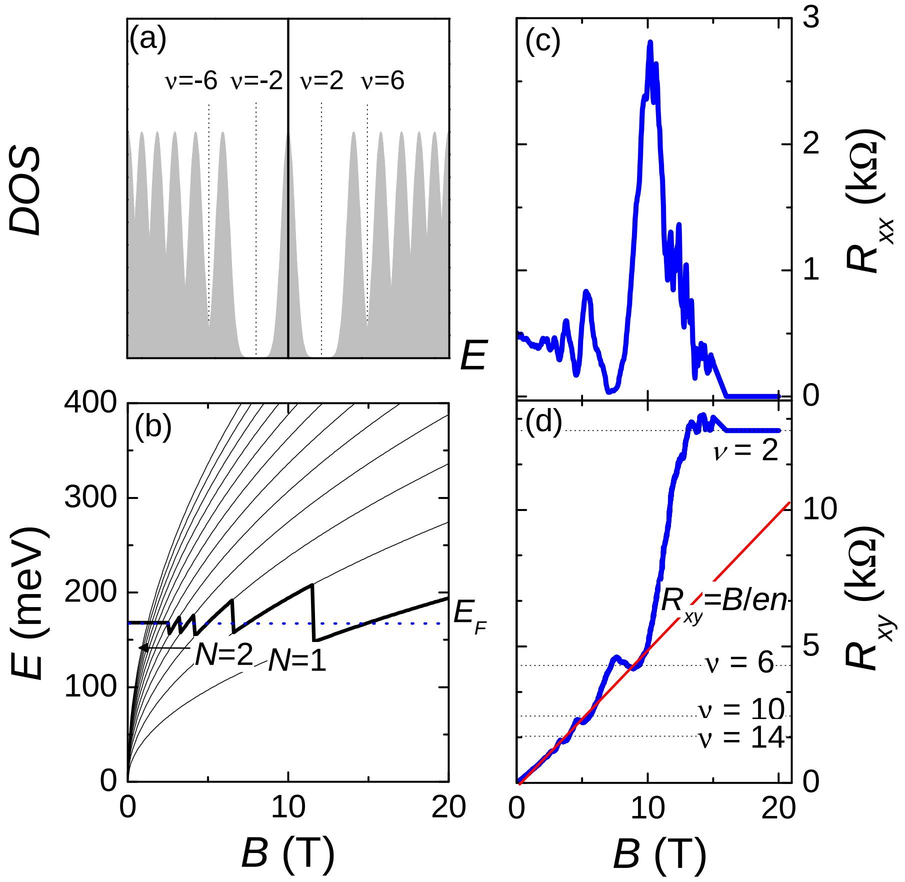

Figure 2.5: *(a) The density of states (DOS) for the Landau levels in single layer layer graphene. Dashed lines show filling factors, corresponding to fully occupied Landau levels. (b) DOS as a function of the applied magnetic field B for different energy levels N = 0, 1, 2, ... The bold line represents how the energy levels are occupied by increasing the magnetic field. (c) Oscillating magnetoresistance* R_{xx} *as a function of the magnetic field. (d) Quantized Hall resistance* R_{xy} *showing plateaus at filling factors* $\nu = 2, 6, 10, \ldots$.

Due to the four-fold degeneracy and half -integer quantization for fully occupied Landau levels correspond filling factors $\nu = 4 \times \left(\frac{1}{2}, \frac{3}{2}, \frac{5}{2}, \ldots\right) = (2, 6, 10, \ldots)$ [see Fig. 2.5(a)].

In Fig. 2.5(c) we visualize the stepwise filling of the energy-levels by the oscillating character of the magnetoresistance R_{xx} for $n = 1.4 \cdot 10^{16}$ m^{-2}. These so-called Shubikinov de Haas oscillations are a result of the stepwise occupation of the energy levels, moving through partially occupied energy levels with high conductivity and fully occupied energy levels with low conductivity. By increasing the magnetic field even further we separate the Landau levels enough that the transport is not dominated anymore by thermal activation, resulting in zero-minima in the resistance R_{xx} and quantized Hall plateaus R_{xy} for filling factors $\nu = 2$, 6, 10, ...

$$R_{xy} = \frac{B}{ne} = \frac{B}{\frac{\nu eB}{h} e} = \frac{1}{\nu} \frac{h}{e^2} \tag{2.15}$$

Here $\frac{h}{e^2}$ is the Hall resistance for $\nu = 1$, defined by the the two elementary constants e (the electron charge) and h (Planck's constant) and has a value $R_{xy} = 25812.80755718\ \Omega$. These quantized plateaus are illustrated in Fig. 2.6(d) compared to the classical Hall resistance from Eq. (2.10) for $n = 1.4 \cdot 10^{16}$ m^{-1} (straight line). For graphene the lowest Landau level is four-fold degenerated, leading to the observation of a half integer quantum Hall effect at filling factors $\nu = 2, 6, 10$. Further increase of the magnetic field leads to the breaking of this degeneracy, the appearance of quantized states at filling factors $\nu = 0$ ($B > 15$ T)[26] and $\nu = \pm 1$ ($B > 30$ T).[27] Full breaking of the lowest Landau level is in general only observed for fields exceeding 30 T,[27] or in high mobility samples, i.e. placed on hexagonal boron nitride,[28] or suspended from the substrate.[29] For these high mobility samples the quantum Hall effect appears already for much smaller fields which opens a new field of interest to study interaction induced phenomena.[29, 30]

A more direct way to study the DOS is to keep the magnetic field constant and change the Fermi energy by sweeping the carrier concentration n from the hole-doped regime (negative n) to the electron-doped regime (positive n) [see section 3.2 for more details]. In Fig. 2.6(b) we show the resistive behavior of R_{xx} and R_{xy} at a fixed magnetic field $B = 15$ T and a temperature $T = 4.2$ K as a function of charge carrier concentration n, swept from hole doping $n = -4.5 \cdot 10^{16}$ m^{-2} to electron doping $n = 4.5 \cdot 10^{16}$ m^{-2}. Zero-minima in R_{xx} and quantum Hall plateaus in R_{xy} appear at filling factors $\nu = \pm 2, \pm 6, \pm 10, ...$ corresponding to charge carrier concentrations $n = \left(\pm 2\frac{eB}{h}, \pm 6\frac{eB}{h}, \pm 10\frac{eB}{h}\right)$, when the next Landau level is fully occupied [compare Fig. 2.7(a) and Fig. 2.7(b)].

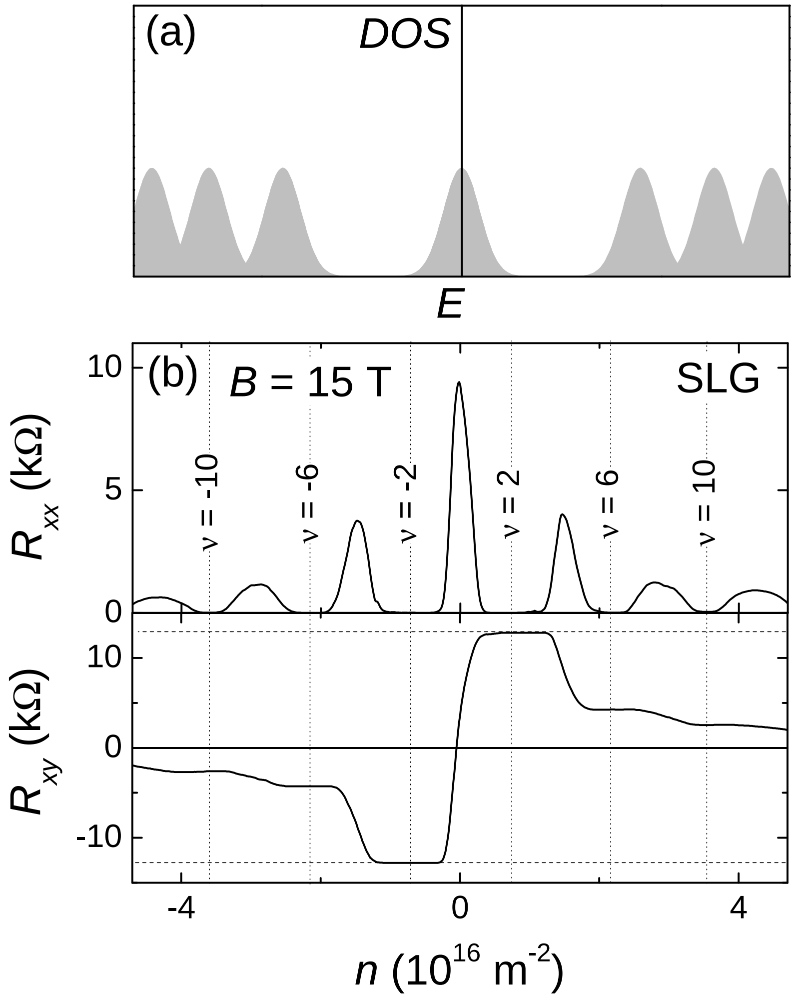

Figure 2.6: *(a) Density of states (DOS) as a function of the energy E for single layer graphene (SLG). Non-equidistant spaced Landau levels: denser packed Landau levels for increasing $\mathcal{N}$. (b) Experimental data of the magnetoresistance R_{xx} and the Hall-resistance R_{xy} as a function of the induced charge carrier concentration n at T = 4.2 K and constant magnetic field B = 15 T. R_{xx}-minima and R_{xy}-plateaus at filling factors $\nu = \pm 2$, ± 6, ± 10, etc.*

2.4.3 Bilayer graphene

In bilayer graphene the dispersion at the K(K')-points is not anymore linear [see section 2.3]. In the low energy approximation[14] we can describe the Landau level spectrum of bilayer graphene by Eq. (2.16).

$$E_N = \pm\hbar\omega_c\sqrt{N(N-1)} \tag{2.16}$$

Here $\omega_c = \frac{eB}{m^*}$ is the cyclotron frequency and N the Landau level index. Different from single layer graphene we see here that the high lying Landau levels $N >> 1$ are almost equidistant spaced [see Fig. 2.7(a)], i.e. $\Delta E_N \approx \hbar\omega_c$, similarly to the case of a conventional semiconductor. A closer look at Eq. (2.16) shows that apart from the spin and valley degeneracy we have an extra two-fold degeneracy in the zero energy levels for $N = 0, 1$, which make the zero energy in total eightfold degenerated. The implication for the appearance of the QHE is that the zero energy level in bilayer graphene is double occupied with respect to the QHE in single layer graphene. This double occupation can be observed by the much wider R_{xx}-peak around the CNP, and first non-degenerated quantum Hall levels at filling factors $\nu = \pm 4$ [see Fig. 2.7(b)]. In Fig. 2.7(b) we show the magnetoresistance R_{xx} and Hall resistance R_{xy} as a function of the charge carrier concentration n at $B = 15$ T and $T = 4.2$ K. Apart from the first quantum Hall levels at $\nu = \pm 4$ we see the appearance of quantum Hall levels at $\nu = \pm 8, \pm 12, ...$, etc. This shows that for non-zero energy the Landau levels are four-fold degenerated, owing to spin and valley, which follows from Eq. (2.16) since the non-zero energies ($N \neq 0, 1$) have unique values for each N.

2.5 Conclusion

In this chapter we presented the most relevant electronic properties of graphene with and without applied magnetic field, which form a proper basis to read also the upcoming chapters. The linear dispersion at the K(K')-points is responsible for the massless and relativistic character of the charge carriers and the observation of a half-integer unconventional quantum Hall effect. Additionally we introduced the concept of bilayer graphene, two stacked layers of graphene which have a coupling between the two layers and opens a new field of research. The dispersion at the K(K')-points modifies to a parabolic shape and implies the charge carriers have a finite effective mass and showing an integer unconventional quantum Hall effect.

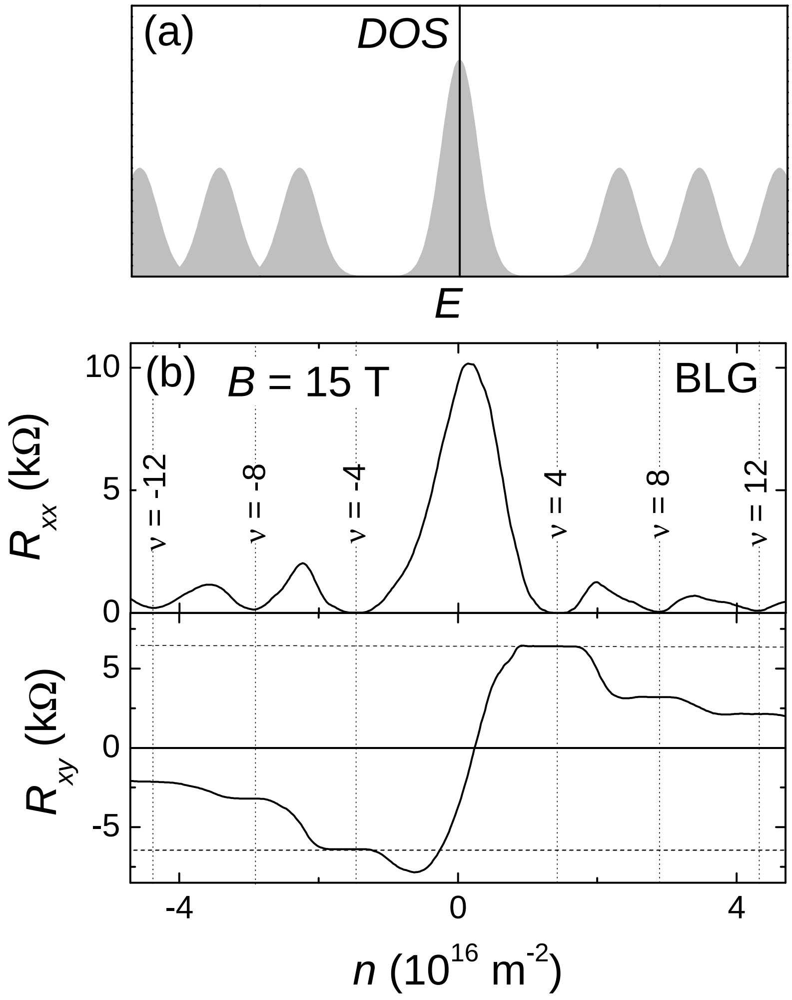

Figure 2.7: *(a) Density of states (DOS) as a function of the energy E for bilayer graphene (BLG). Double occupation of the zero energy level is due to spin, valley, and layer-degeneracy. (b) Experimental data of the magnetoresistance R_{xx} and the Hall-resistance R_{xy} as a function of the induced charge carrier concentration n at T = 4.2 K and constant magnetic field B = 15 T. R_{xx}-minima and R_{xy}-plateaus appear at filling factors $\nu = \pm 4$, ± 8, ± 12, etc.*

References

[1] S. Iijima, “Helical microtubules of graphitic carbon”, *Nature* **354**, 56–58 (1991).

[2] H. W. Kroto, J. R. Heath, S. C. O’Brien, R. F. Curl, and R. E. Smalley, “C60: Buckminsterfullerene”, *Nature* **318**, 162–163 (1985).

[3] K. S. Novoselov, A. K. Geim, S. V. Morozov, D. Jiang, M. I. Katsnelson, I. V. Grigorieva, S. V. Dubonos, and A. A. Firsov, “Two-dimensional gas of massless Dirac fermions in graphene”, *Nature* **438**, 197–200 (2005).

[4] N. D. Mermin, “Crystalline Order in 2 Dimensions”, *Physical Review* **176**, 250–254 (1968).

[5] K. S. Novoselov, A. K. Geim, S. V. Morozov, D. Jiang, Y. Zhang, S. V. Dubonos, I. V. Grigorieva, and A. A. Firsov, “Electric field effect in atomically thin carbon films”, *Science* **306**, 666–669 (2004).

[6] P. R. Wallace, “The Band Theory of Graphite”, *Physical Review* **71**, 622–634 (1947).

[7] Y. Zhang, Y.-W. Tan, H. L. Stormer, and P. Kim, “Experimental observation of the quantum Hall effect and Berry’s phase in graphene”, *Nature* **438**, 201–204 (2005).

[8] C. Kittel, “Introduction to solid state physics”, John Wiley and Sons Ltd. (2004).

[9] C. Canali, M. Martini, Ottavian.G, and K. Zanio, “Time of Flight Measurement of Differential Negative Mobility in Cdte”, *Physics Letters A* **A 33**, 241 (1970).

[10] F. J. Morin and J. P. Maita, “Conductivity and Hall Effect in the Intrinsic Range of Germanium”, *Physical Review* **94**, 1525–1529 (1954).

[11] C. R. Dean, A. F. Young, I. Meric, C. Lee, L. Wang, S. Sorgenfrei, K. Watanabe, T. Taniguchi, P. Kim, K. L. Shepard, and J. Hone, “Boron nitride substrates for high-quality graphene electronics”, *Nature Nanotechnology* **5**, 722–726 (2010).

[12] K. I. Bolotin, K. J. Sikes, Z. Jiang, M. Klima, G. Fudenberg, J. Hone, P. Kim, and H. L. Stormer, “Ultrahigh electron mobility in suspended graphene”, *Solid State Communications* **146**, 351–355 (2008).

[13] A. Grneis, C. Attaccalite, L. Wirtz, H. Shiozawa, R. Saito, T. Pichler, and A. Rubio, “Tight-binding description of the quasiparticle dispersion of graphite and few-layer graphene”, *Physical Review B* **78**, 205425 (2008).

[14] E. McCann, D. S. L. Abergel, and V. I. Fal’ko, “Electrons in bilayer graphene”, *Solid State Communications* **143**, 110–115 (2007).

[15] J. D. Sanchez-Yamagishi, T. Taychatanapat, K. Watanabe, T. Taniguchi, A. Yacoby, and P. Jarillo-Herrero, “Quantum Hall Effect, Screening, and Layer-Polarized Insulating States in Twisted Bilayer Graphene”, *Physical Review Letters* **108**, 076601 (2012).

[16] J. Zhang, J. Xiao, X. Meng, C. Monroe, Y. Huang, and J.-M. Zuo, “Free Folding of Suspended Graphene Sheets by Random Mechanical Stimulation”, *Physical Review Letters* **104**, 166805 (2010).

[17] K. Kim, Z. Lee, B. D. Malone, K. T. Chan, B. Alemn, W. Regan, W. Gannett, M. F. Crommie, M. L. Cohen, and A. Zettl, “Multiply folded graphene”, *Physical Review B* **83**, 245433 (2011).

[18] X. Li, W. Cai, J. An, S. Kim, J. Nah, D. Yang, R. Piner, A. Velamakanni, I. Jung, E. Tutuc, S. K. Banerjee, L. Colombo, and R. S. Ruoff, “Large-Area Synthesis of High-Quality and Uniform Graphene Films on Copper Foils”, *Science* **324**, 1312–1314 (2009).

[19] S. Bae, H. Kim, Y. Lee, X. Xu, J.-S. Park, Y. Zheng, J. Balakrishnan, T. Lei, H. Ri Kim, Y. I. Song, Y.-J. Kim, K. S. Kim, B. Ozyilmaz, J.-H. Ahn, B. H. Hong, and S. Iijima, “Roll-to-roll production of 30-inch graphene films for transparent electrodes”, *Nature Nanotechnology* **5**, 574–578 (2010).

[20] B. Fallahazad, Y. Hao, K. Lee, S. Kim, R. Ruoff, and E. Tutuc, “Quantum Hall Effect in Bilayer Graphene Grown on Cu by Chemical Vapor Deposition”, *Physical Review B* **85**, 201408(R) (2012).

[21] J. B. Oostinga, H. B. Heersche, X. Liu, A. F. Morpurgo, and L. M. K. Vandersypen, “Gate-induced insulating state in bilayer graphene devices”, *Nature Materials* **7**, 151–157 (2008).

[22] W. Zhang, C.-T. Lin, K.-K. Liu, T. Tite, C.-Y. Su, C.-H. Chang, Y.-H. Lee, C.-W. Chu, K.-H. Wei, J.-L. Kuo, and L.-J. Li, “Opening an Electrical Band Gap of Bilayer Graphene with Molecular Doping”, *Acs Nanotechnology* **5**, 7517–7524 (2011).

[23] F. Freitag, J. Trbovic, M. Weiss, and C. Schonenberger, “Spontaneously Gapped Ground State in Suspended Bilayer Graphene”, *Physical Review Letters* **108**, 076602 (2012).

[24] F. Zhang, H. Min, M. Polini, and A. H. MacDonald, “Spontaneous inversion symmetry breaking in graphene bilayers”, *Physical Review B* **81**, 041402 (2010).

[25] K. v. Klitzing, G. Dorda, and M. Pepper, “New Method for High-Accuracy Determination of the Fine-Structure Constant Based on Quantized Hall Resistance”, *Physical Review Letters* **45**, 494–497 (1980).

[26] A. J. M. Giesbers, L. A. Ponomarenko, K. S. Novoselov, A. K. Geim, M. I. Katsnelson, J. C. Maan, and U. Zeitler, “Gap opening in the zeroth Landau level of graphene”, *Physical Review B* **80**, 201403 (2009).

[27] Z. Jiang, Y. Zhang, H. L. Stormer, and P. Kim, “Quantum Hall States near the Charge-Neutral Dirac Point in Graphene”, *Physical Review Letters* **99**, 106802 (2007).

[28] C. R. Dean, A. F. Young, P. Cadden-Zimansky, L. Wang, H. Ren, K. Watanabe, T. Taniguchi, P. Kim, J. Hone, and K. L. Shepard, “Multicomponent fractional quantum Hall effect in graphene”, *Nature Physics* **7**, 693696 (2011).

[29] K. I. Bolotin, F. Ghahari, M. D. Shulman, H. L. Stormer, and P. Kim, “Observation of the fractional quantum Hall effect in graphene”, *Nature* **475**, 196–199 (2011).

[30] X. Du, I. Skachko, F. Duerr, A. Luican, and E. Y. Andrei, “Fractional quantum Hall effect and insulating phase of Dirac electrons in graphene”, *Nature* **462**, 192–195 (2009).

Chapter 3

From graphite to a carbon-based nanodevice

Abstract

This chapter describes the general techniques to fabricate graphene devices used in this thesis. In particular we discuss how to cleave a piece of graphite in order to exfoliate a single sheet of graphene and how to optically distinguish it from multilayer graphene. We discuss how to process a graphene-flake on a Si/SiO$_2$-wafer in order to make electronic contacts on top and make a field effect transistor of it. Finally we discuss how to improve the conduction-properties of graphene even more, i.e. suspending the membrane and annealing the device.

3.1 Introduction

In 2004 K.S. Novoselov et al. showed[1] how to make a high quality nanodevice based on a thin graphite layer from bulk-graphite that is suitable to use as a field effect transistor. Scotch-tape is used to cleave graphite down to a single layer of graphite, graphene. Lithography-techniques are used to build devices which are suitable to investigate the different properties of the samples (e.g. Hall-bars, quantum dots, Aharonov-Bohm rings, Corbino-disks, etc.).[1–3]
This chapter presents stepwise the processing of bulk graphite to a graphene-based device. First of all in section 3.2 we show how to study the electrical properties of a graphene-device by means of a back-gate-voltage. After this we discuss in section 3.3 in detail how to cleave a piece of graphite such that it leaves nice homogenous flakes of graphene and how to recognize them under an optical microscope. In sections 3.4 and 3.5 we focus our attention how to make electrical contacts to these graphene-flakes and how to clean chemical compounds remaining from the lithography-procedure by heat annealing. Finally we will discuss in section 3.6 how to improve the conduction-properties by suspending the sample from the substrate and remove the remaining inhomogeneities by using current annealing.

3.2 The device-requirements

In Fig. 3.1(a) we show the most basic form of an electronically connected graphene-flake: a single graphene flake is deposited on a Si/SiO$_2$-substrate and two gold-contacts are deposited on both sides of the flake. By using standard AC lock-in techniques we measure the resistance R of the graphene. The total resistance depends on the sample size, contact geometry and doping of the sample. We can control both the size and contact geometry by means of the lithography-procedure [described in section 3.4 and Appendix A], however, the doping depends strongly on the local potential caused by either an external potential or impurities. By applying a positive (negative) voltage V_G between the highly n^{++}-doped Si and the graphene we can capacitively induce electrons (holes) in the graphene. Here the SiO$_2$ plays the role as a dielectric with thickness $d = 300$ nm and dielectric constant $\epsilon_r = 3.9$. We approximate the graphene sheet on top of the Si/SiO$_2$ as a flat plate capacitor with capacitance C.

$$C = \frac{\epsilon_0 \epsilon_r A}{d} \tag{3.1}$$

Here ϵ_0 is the dielectric constant in vacuum, ϵ_r the dielectric constant of SiO$_2$, A the surface of the graphene, and d the thickness of the SiO$_2$. Subsequently

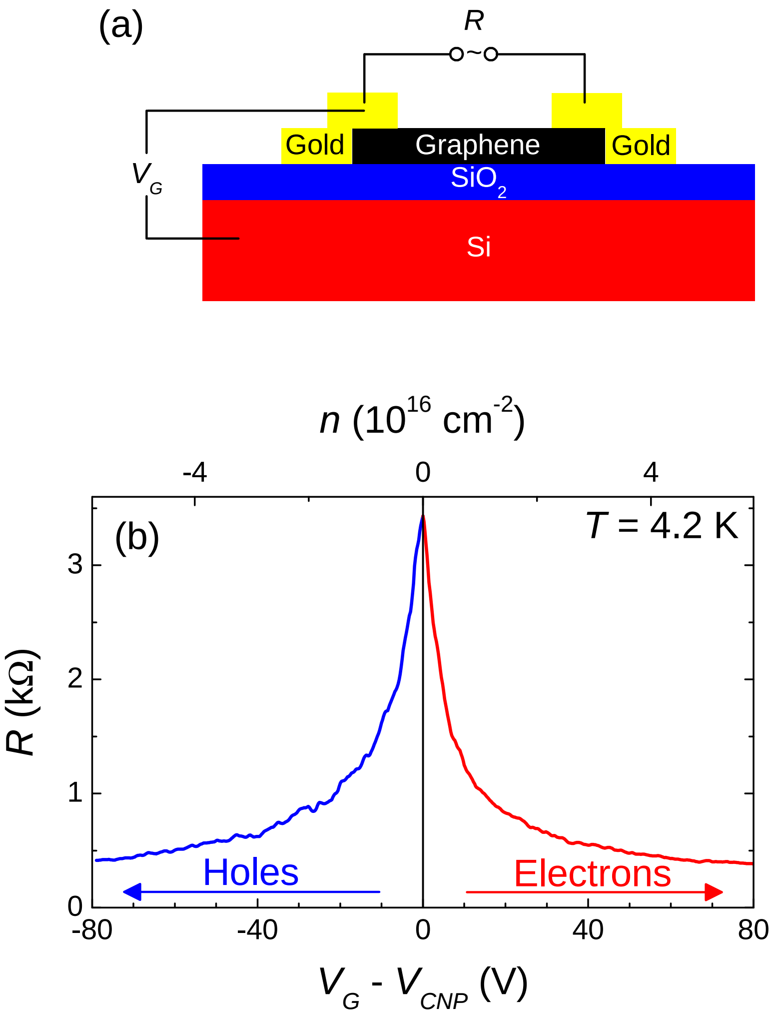

Figure 3.1: *(a) Side-view of a two terminal connected graphene-sample on top of a Si/SiO*$_2$*-substrate. With an applied gate-voltage* V_G *over the insulating SiO*$_2$ *we can induce capacitively holes and electrons in the graphene. (b) Longitudinal resistance* R *as a function of the gate-voltage* $V_G - V_{CNP}$ *(bottom axis) and the induced charge carrier concentration* n *(top axis) for a standard graphene device from Fig. 3.1(a); here* V_{CNP} *is the gate voltage where the carrier concentration in the graphene flake is zero. i.e. for* $V_G - V_{CNP} > 0$ *(*$V_G - V_{CNP} < 0$*) we induce electrons (holes) in the graphene.*

we calculate the capacitance by $C = \frac{Q}{V_G}$ with Q the total charge, and V_G the backgate applied voltage. The total charge Q in the two-dimensional sheet can be expressed as the product of the elementary charge of one electron e, the graphene surface area A, and the surface density of the charge carriers n, $Q = eAn$. This leads to a general equation Eq. (3.2) for the charge carrier concentration n.

$$n = \frac{\epsilon_0 \epsilon_r}{ed} \cdot V_G \tag{3.2}$$

Additionally we have to take account the impurities which causes a fixed voltage-offset V_{CNP} from the point where we effectively induce no charge carriers in the graphene, the charge neutrality point (CNP). This means that if we apply no gate-voltage V_G, there are effectively always electrons (or holes) present due to doping of the surface impurities. By applying a gate-voltage equal to the offset V_{CNP}, we will reach the CNP which changes Eq. (3.2) into Eq. (3.3)

$$n = \frac{\epsilon_0 \epsilon_r}{ed} \cdot (V_G - V_{CNP}) = \alpha \cdot (V_G - V_{CNP}) \tag{3.3}$$

Here we call α the leverage factor, which is a constant depending on the SiO_2 only, $\alpha = 7.2 \cdot 10^{14}$ m^{-2} for $d = 300$ nm and $\epsilon_r = 3.9$. In Fig. 3.1(b) we show the resistive behavior R as a function of $V_G - V_{CNP}$ (bottom axis), and the charge carrier concentration n (top axis). By applying a non-zero voltage $V_G - V_{CNP}$ we induce charge carriers in the graphene and the device gets more conducting, resulting in decreasing resistance R. At the CNP there are theoretically no charge carriers in the graphene, however the inhomogeneous distribution of impurities causes the existence of electron-hole puddles[4] and therefore a region around the CNP where electrons and holes coexist. In chapter 4 we will study the coexistence of electrons and holes near the CNP in more detail.

3.3 Micromechanical cleavage and identification of graphene-flakes

In graphite the atoms are bond in plane in a hexagonal lattice. The intra-layer binding of the carbon-atoms is much stronger (covalent binding) than the inter-layer binding of the planes (Van der Waals binding). Therefore we can use graphite as the basis of a pencil to write: the separate carbon-layers remove easily and leave traces on a paper. The removal of the separate layers can be done more accurately by mechanical cleavage of the graphite with a piece of Scotch-tape. We can continue this procedure until a single sheet of carbon-atoms, graphene, is remaining. In order to process high quality devices we use high quality starting material defined by the number of imperfections (< 50 ppm). We can distinguish roughly three different types of graphite we used for all devices in this thesis.

1. Natural graphite:[5] Natural graphite is graphite that is formed by nature and obtained of mines, million years of optimal growing conditions resulted in high purity graphite which is very suitable for cleaving single layers of graphene. The purity is varying from 5 ppm to 100 ppm.
2. Kish graphite:[6] Kish graphite is separated from kish, a byproduct of the steal industry, which is a mixture of graphite, desulphurization slag, and iron. Ultrapure kish graphite is obtained by heating the material up to temperatures of 2000 °C which leads ultimately to impurity levels down to 3 ppm.
3. Highly oriented pyrolytic graphite (HOPG):[7] Pyrolytic graphite is a graphite material with a high degree of preferred crystallographic orientation of the c-axes perpendicular to the surface of the substrate, obtained by graphitization heat treatment of pyrolytic carbon or by chemical vapor deposition at temperatures above 2800 °C. By annealing under compressive stress at approximately 3600 °C results in highly oriented pyrolytic graphite (HOPG) with an impurity level in the order of 10 ppm.

The processing of a sample starts with the cleavage of a single sheet of graphene; this process is performed by cleaving a bulk piece of graphite with a piece of Scotch tape. In general the best technique is to take a large flat piece of graphite[*] and press this with some force on the sticky side of the tape. After this the tape can be gently removed and a more remarkably thinner graphite-layer sticks to the tape. In addition some extra cleavage should be done on this thin layer by using a new tape or fold the tape several times. A fresh layer of graphite is stuck to the tape and we start to press this to the SiO_2-side of the Si/SiO_2. Very important is that we gently strike the backside of the tape in different orientations to increase the probability to leave some of the graphite at the SiO_2. A typical result of graphene-flakes on a Si/SiO_2-substrate is shown in Fig. 3.2. Here we observe graphene layers with different contrast, which is due to the direct relation between the contrast and the graphene-thickness [see more detailed description below].[9] We indicate with 1L-4L the number of layers of the different flakes, these assumptions are mainly based on the crossing of the layers; for example, two overlapping single layers cause a more darker area,

---

[*] See Appendix A and supplementary material of reference 8 for more detailed information how to cleave the best samples.

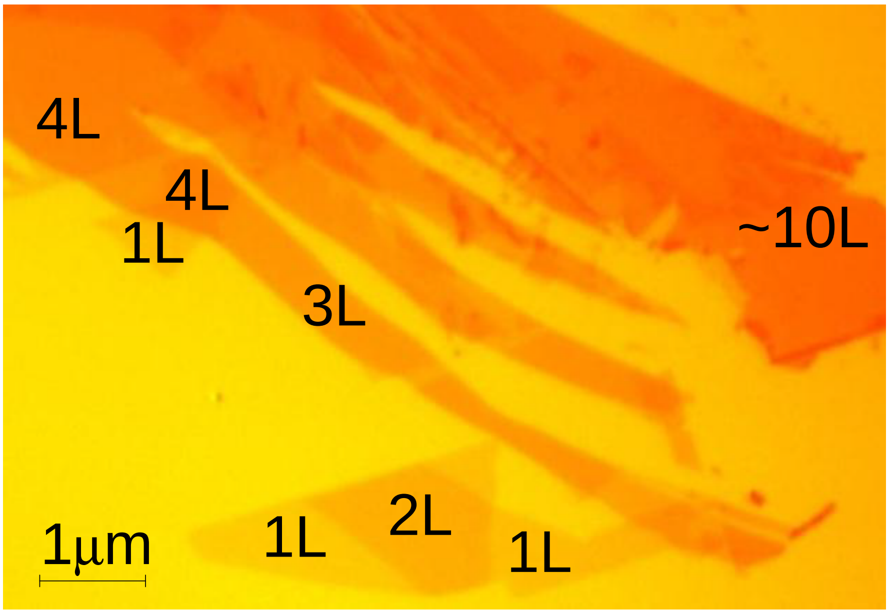

Figure 3.2: *Typical result after cleavage of graphite and depositing the graphene-layers on top of the Si/SiO$_2$-substrate. We mark with 1L-4L the layer thicknesses which we can distinguish by optical contrast.*

a double layer.

Fig. 3.2 shows how we can distinguish optically the layer thicknesses. In order to optimize the flake-selection we investigate here the optical parameters we use. In Fig. 3.3(a) we show the qualitative picture of the situation of a graphene layer on top of a Si/SiO$_2$-substrate. The incoming light I_0 is reflected by both the substrate and the graphene on top of the substrate. The refractive index of a graphene layer is approximated[10] to be $n \approx 2.0 - 1.1i$ and therefore the intensity of the reflected light of the graphene and the substrate is different. This difference is expressed by the contrast C in Eq. (3.4), the ratio between the reflection on the SiO$_2$, R_0, and with a graphene-flake on top, R_G.

$$C = \frac{R_0 - R_G}{R_0} \tag{3.4}$$

First of all we describe the reflectance R_G of a graphene-sheet (layer 1) on top of the Si/SiO$_2$-substrate (layer 3 and 2), from which we afterwards can derive the more easy reflectance R_0 without a graphene-layer on top. The three layers are characterized by their refraction indices n_1, n_2 and n_3 and their thicknesses d_1, d_2 and d_3, here d_3 approximated to be semi-infinitely thick. We start to describe the incoming (s,p)-polarized light with the Fresnel's amplitude coefficients for the reflection r_{ij} and the transmission t_{ij} on the interface (i,j).[11] Assuming a perfect reflection $t_{ij} = 1 - r_{ij}$ we describe all coefficients for both s- and p-polarized light at the interface (i, j) by Eq. (3.5) and Eq. (3.6).

$$r_{ij,s} = \frac{n_i \cos(\theta_i) - n_j \cos(\theta_j)}{n_i \cos(\theta_i) + n_j \cos(\theta_j)} \tag{3.5}$$

$$r_{ij,p} = \frac{n_i \cos(\theta_j) - n_j \cos(\theta_i)}{n_i \cos(\theta_j) + n_j \cos(\theta_i)} \tag{3.6}$$

Here θ_i and θ_j are the angles of the incoming and outgoing light with respect to the normal axis of the substrate (as defined in Fresnel's law). The observed intensity is a result of the interference between the reflected and transmitted beams. Every beam travelling through one layer experiences a phase shift β_i.

$$\beta_i = \frac{2\pi d_i}{\lambda} n_i \cos(\theta_i) \tag{3.7}$$

From this we obtain the reflection coefficients $r_{ijk,s}$ at the interface (1,2,3) (identical for p-polarized light by replacing s by p).

$$r_{0123,s} = \frac{r_{01,s} + r_{12,s}e^{-2i\beta_1} + (r_{01,s}r_{12,s} + e^{-2i\beta_1})r_{23,s}e^{-2i\beta_2}}{1 + r_{01,s}r_{12,s}e^{-2i\beta_1} + (r_{12,s} + r_{01,s}e^{-2i\beta_1})r_{23,s}e^{-2i\beta_2}} \tag{3.8}$$

For the simple case without graphene on top of the Si/SiO$_2$ ($d_1 = 0$ and $n_1 = n_0$) Eq. (3.8) reduces with $r_{01,s} = 0$ and $\beta_1 = 0$ to Eq. (3.9)

$$r_{023,s} = \frac{r_{12,s} + r_{23,s}e^{-2i\beta_2}}{1 + r_{12,s}r_{23,s}e^{-2i\beta_2}} \tag{3.9}$$

The total reflected intensity of Eq. (3.8) and Eq. (3.9) can be calculated by using $R_{tot} = \frac{R_s+R_p}{2}$ with $R_s = |r_{0123,s}|^2$ and $R_p = |r_{0123,p}|^2$. After calculating the total reflected intensity we determine the contrast C of Eq. (3.4) between the graphene and the uncovered Si/SiO$_2$. In Fig. 3.3(b) we show how the contrast strongly depends on both the wavelength λ and the SiO$_2$-thickness d. By choosing the right configuration of both the wavelength and SiO$_2$-thickness we optimize the contrast of the graphene with the SiO$_2$. An important factor to

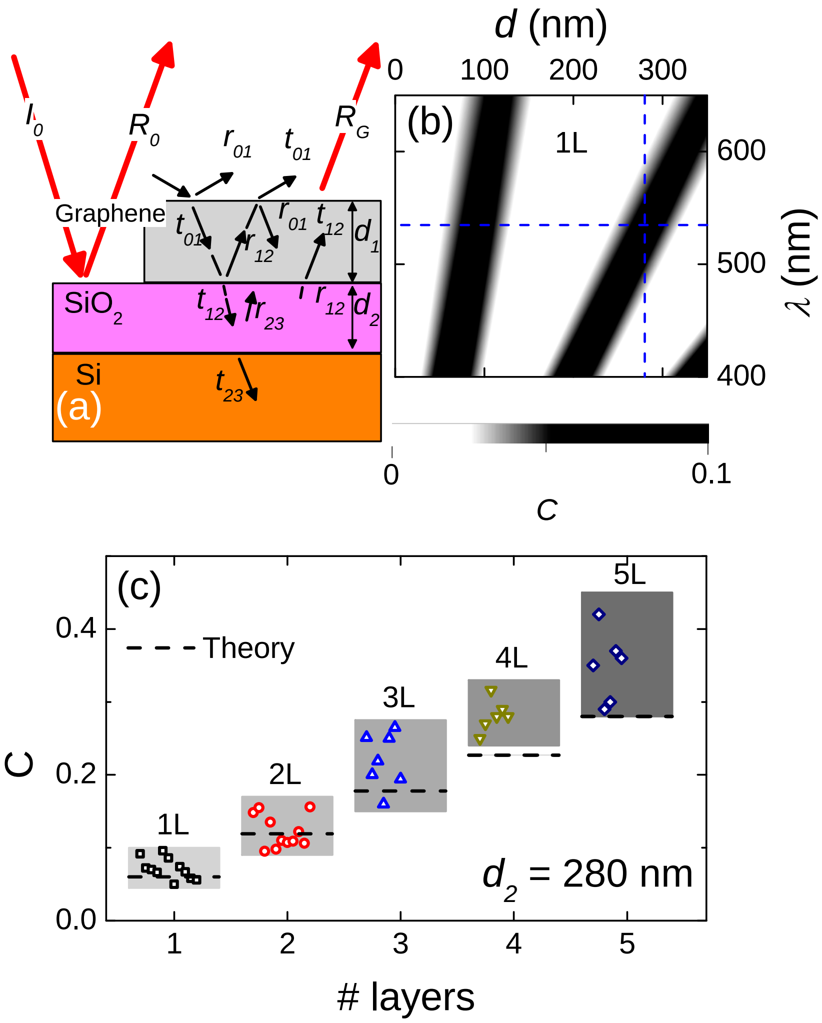

Figure 3.3: *(a) Qualitative picture of the reflection of the incoming light I_0 of a naked Si/SiO$_2$-substrate, R_0, and with a graphene layer on top, R_G. (b) Contrast C between the naked Si/SiO$_2$-substrate and the Si/SiO$_2$-graphene as a function of the SiO$_2$-thickness d and the incoming wavelength λ for one layer (1L) of graphene. (c) Contrast C for increasing numbers of layers graphene predicted by theory (dashed lines) and experimentally measured (dots in the grey boxes).*

take into account is the sensitivity of the human eye to particular wavelengths, maximum around 550 nm. In Fig. 3.3(b) we see that that the optimal thickness of the SiO_2 for $\lambda = 550$ nm is either $d = 90$ nm or $d = 280$ nm. † The aim of choosing the right SiO_2-thickness is to distinguish as accurate as possible a single layer from a double layer, a double layer from three layers, etc. In Fig. 3.3(c) the dotted lines represent the theoretically expected contrast for 1-5 layers if we take into account the refractive index of single layer graphene, $n \approx 2.0 - 1.1i$.[12] Besides the theoretical dotted lines we have experimentally measured the contrast for graphene-flakes with a layer thickness of 1-5 layers. These experimental dots are made on seven regions like in Fig. 3.2 where we can make clear distinction due to the overlapping of flakes. The grey boxes around the experimental values show the error-margin of the contrast-data we have obtained. These grey boxes demonstrate the uncertainty in the contrast and show that even under optimal conditions the optical recognition has a big error margin ($\approx 50\%$) in flake-selection of the right thickness. Definite conclusions can only be made after Raman spectroscopy,[13] and/or magnetotransport study, i.e. showing half integer or integer quantum Hall effect [see chapter 2]. Additionally we see that for thicker layers we deviate stronger from the theoretical model, which can be attributed to the approximation of the optical properties of graphite, which has a larger refractive index $n \approx 2.6 - 1.3i$ than single layer graphene.[12]

3.4 Lithography processing of electrical contacts

After identifying flakes with the correct number of layers and the right dimensions we would like to explore the electronic properties of the sample by processing electric contacts on it. In Fig. 3.4 we show a basic overview of the lithography steps we performed to make electric contacts to the samples we used in this thesis. In Appendix A we discuss all exact parameters and process steps of this lithography-procedure guided by experimental pictures. First of all we spincoat a transparent polymer on top of the Si/SiO_2/graphene (a → b), note that transparent here means that it should fulfill conditions of both the refractive index n and thickness d to keep the graphene optically visible underneath the polymer. Subsequently we perform either optical lithography or electron beam lithography to write a pattern in the polymer (b → c). Electron

---

[†] Another important biological property of the human eye is the increasing sensitivity for decreasing light-intensity. This in generally implies it is more easy to select the graphene layers in a pretty dark room with reduced power of the microscope-light.

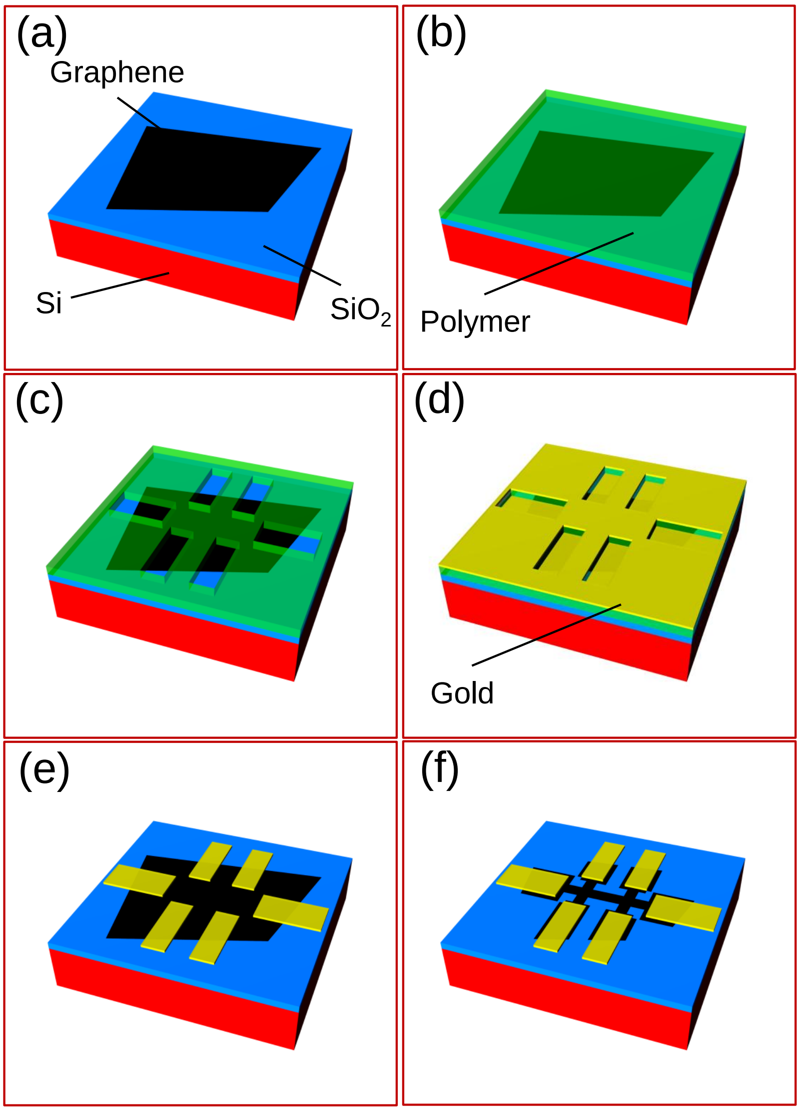

Figure 3.4: *Lithography processing steps of a graphene-device. (a) Deposited graphene on a Si/SiO_2-wafer. (b) Spincoated polymer on top of the Si/SiO_2/graphene. (c) We can create a pattern in the polymer by using either EBL or photolithography. (d) Evaporated titanium/gold on top of the created structure in (c). (e) Lift-off of the titanium/gold on top of the polymer. (f) Nanoscale patterning of the graphene to a Hall-bar geometry.*

beam lithography is much more accurate to write the pattern (structures down to 20-50 nm), however it is much more time consuming than the alignment of an optical mask above the sample. After we wrote the desired pattern in the polymer we evaporate 3 nm Ti and 35 nm Au on top of the sample (c → d) and perform the lift-off of the metal on the remaining polymer, i.e. solute the remaining polymer underneath the metal (d → e). After this step the sample is electrically connected and its electronic quality can be tested [see section 3.2]. In general the sample needs to be structured in a Hall-bar geometry (f) to simplify the experimental conditions. The most easy way to do this is to repeat the procedure to write a pattern in a spincoated polymer (b → d) and etch the structure in oxygen plasma. Deeper understanding and more experimental background on the sample fabrication can be found in Appendix A.

3.5 Heat-annealing of the device

In section 3.2 we have discussed that a graphene sample has ideally a charge neutrality point (CNP) centered around zero gate voltage. However the presence of impurities causes the sample to be either electron- or hole-doped, causing the offset V_{CNP} in Eq. (3.2). The lithography-processing [section 3.4] introduces extra impurities which make the sample even more doped. Several cleaning techniques are used to reduce the amount of inhomogeneities, e.g. cleaning with Ar-plasma,[14] mechanical cleaning with AFM,[15] etc. The most common method to clean samples is a heat-annealing in vacuum.[16,17] To illustrate this procedure we place a strongly electron-doped sample with $V_{CNP} = 55$ V into vacuum. In order to reduce the amount of impurities we pump and flush the space with helium-gas. Subsequently we perform a gatesweep [see A_0 in Fig. 3.5(a)] to study the characteristic conduction properties. In order to remove the impurities on the surface of the graphene we heat the graphene sample to a temperature T_A and impurities start to evaporate from the surface [see inset Fig. 3.5(a)]. In Fig. 3.5(b) we show that the resistance at $V_G = 0$V starts to increase rapidly after heating the sample at a temperature of 115 °C and results into a gatesweep centered around $V_{CNP} =$ -5 V (curve A_1, Fig. 3.5(a)). Further annealing (A_2) at a higher temperature $T = 165$ °C results in an even sharper gatesweep curve with $V_{CNP} = 1$ V with even higher mobility. These temperatures are in general high enough to remove most of the doping (like water). Even higher temperatures increases the sample quality even more, but is also harmful for the deposited gold-contacts and wiring.

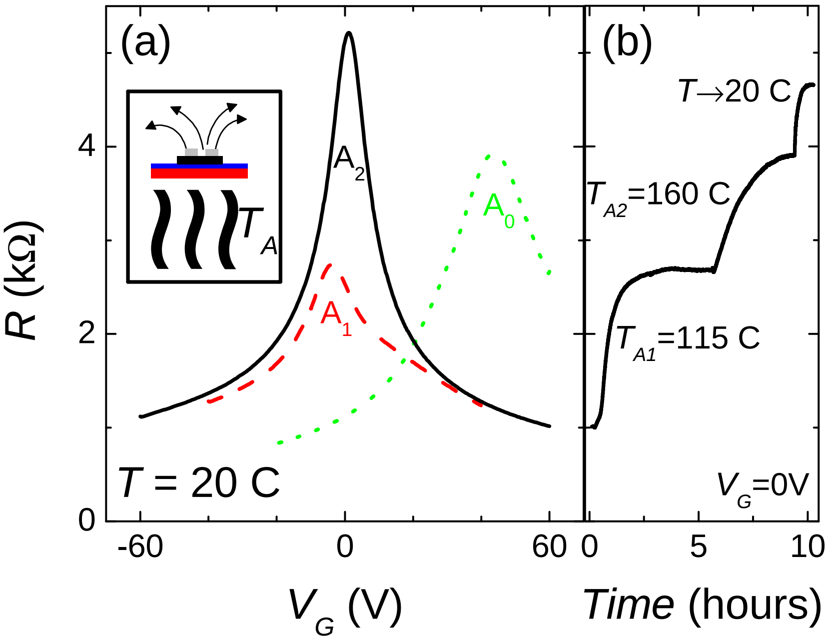

Figure 3.5: *(a) Gatesweep at room temperature before annealing (A0), after annealing at 115 °C (A1), and after annealing at 165 °C (A2). inset: schematic overview of the annealing procedure under vacuum condition and temperature* T_A*. (b) Resistance R at* $V_G = 0$ *V for annealing temperatures 115 °C (A1) and 165 °C (A2), followed by the cooling down to room temperature.*

3.6 Suspending graphene from the substrate

Further optimization of the electronic properties of the graphene-sheet can be achieved by replacing the SiO_2-substrate.[18] The lattice mismatch and impurities between the SiO_2 and the graphene causes a rippled surface, q.e. decreasing the electronic quality. Recent developments[18] have shown that replacing the SiO_2-substrate by hexagonal Boron-nitride (hBN) results in samples with much higher quality. The ultimate method however to avoid any interaction with the substrate is to fully remove the substrate underneath the graphene, or so-called suspending the graphene from the substrate.[19]

The most straight-forward way to suspend a graphene-sample from the substrate is to partially underetch the SiO_2 with buffered HF.[19] However buffered

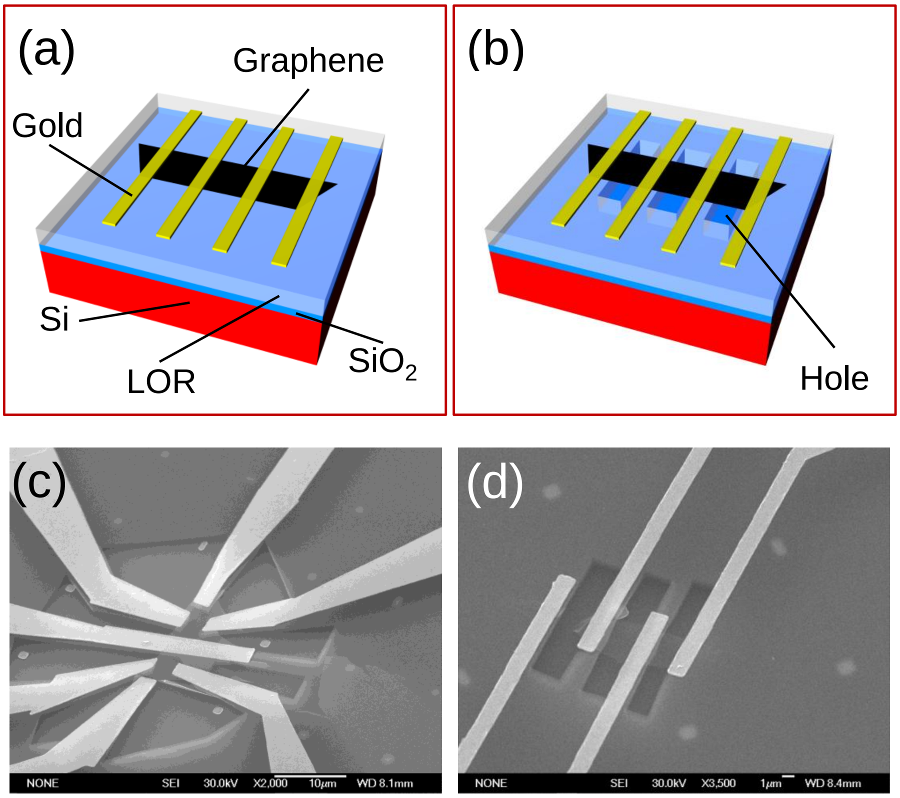

Figure 3.6: *(a) Graphene-sample on top of a Si/SiO_2/LOR-substrate. (b) Graphene-sample From Fig. 3.6a partially suspended from the substrate by writing small trenches with EBL-lithography in the underlying LOR-polymer. (c) Suspended sample in a typical four-probe configuration. A clear trench underneath the graphene is removed, while the contacts are still supported by a polymer layer. (d) A typical two-probe configuration with trenches underneath the graphene.*

HF is a very aggressive acid which makes devices very unstable during processing, which gives low yield process rate and limits the sample size. A more friendly method is to process a graphene sample on top of a Si/SiO_2/LOR-polymer substrate [Fig. 3.6(a)] and suspend the sample by an additional EBL-step (a → b) by writing trenches in the underlying polymer of LOR-resist. The SEM-pictures in Fig. 3.6(c) and 3.6(d) show SEM-pictures of a typical four-probe sample (Fig. 3.6(c)) and a two probe sample (Fig. 3.6(d)). More technical details of this procedure are described in reference 20.

The carrier density in graphene is varied by applying a dc voltage V_G between the back gate electrode n^{++} Si and the graphene flake. Based on the serial-capacitor model, the unit capacitance of the system is 7.2 aFμm^{-2}, which relates the gate voltage with the density as $n = \alpha V_G$, where α is the leverage factor of $\alpha = 0.5 \times 10^{14}$ m^{-2}V^{-1} specified in Eq. (3.3). Inhomogeneities on the surface of the sample causes the sample to be doped and scatter charge carriers in the sample. Annealing is necessary to get rid of these inhomogeneities and center the CNP around zero gate voltage. As these samples are fully suspended between the contacts the applied electric field by the gate-voltage causes a finite electrostatic force on the membrane, causing a collapse at too high applied gate voltage. A typical value of the maximum applied gate-voltage is 60 V, which corresponds to a maximum concentration of $n = 3 \cdot 10^{15}$ m^{-2}. This is about 5% of the typical maximum concentration-values for substrate-supported samples. We need to anneal the suspended sample to center the CNP around zero gate-voltage and trace the formation of QH-plateaus.
Typical heat-annealing [see section 3.5] is not applicable due to the low melting temperature of the underlying polymer ($\approx$ 100 °C) and the fragility [‡] of the sample. A more common method to anneal suspended graphene-samples is current-annealing;[21] under a cryogenic temperature of $T = 4.2$ K a dc-voltage bias is slowly applied over two of the contacts [see Fig. 3.7(a)], while the sample start to self-heat by its finite resistance value. In general the annealing in two-probe configuration is most efficient, because it is easier to keep the temperature constant over the whole sample. We expect however that the procedure would work as well in recent developed etched suspended Hall-bars.[20]

In Fig. 3.7(b) we show an example of two annealing steps of a trilayer-sample, studied in chapter 7. Without annealing the sample is heavily hole-doped (black dotted curve A_0) and the resistance R shows almost no dependence on the applied gate-voltage. After the first annealing step A1 a clear dependence on the gate-voltage appears (red dashed curve), while after the second annealing step A2 a clear CNP around V_G =3 V appeared (blue solid curve). The exact annealing procedure is worked out in Fig. 3.7(c) and (d), where we show the applied power P [Fig. 3.7(c)] and the resistance R of the sample [Fig. 3.7(d)] as a function of the time. A dc-current I is linearly increased, which results for a constant resistance to a linear increase of the applied voltage V over the

---

[‡] It is worth noting here that despite graphene is the strongest material on earth the real samples are very fragile due to their small size and thickness. Analogously, a spider web is stronger than stainless steel, but a single (thin) wire from the web is very fragile.

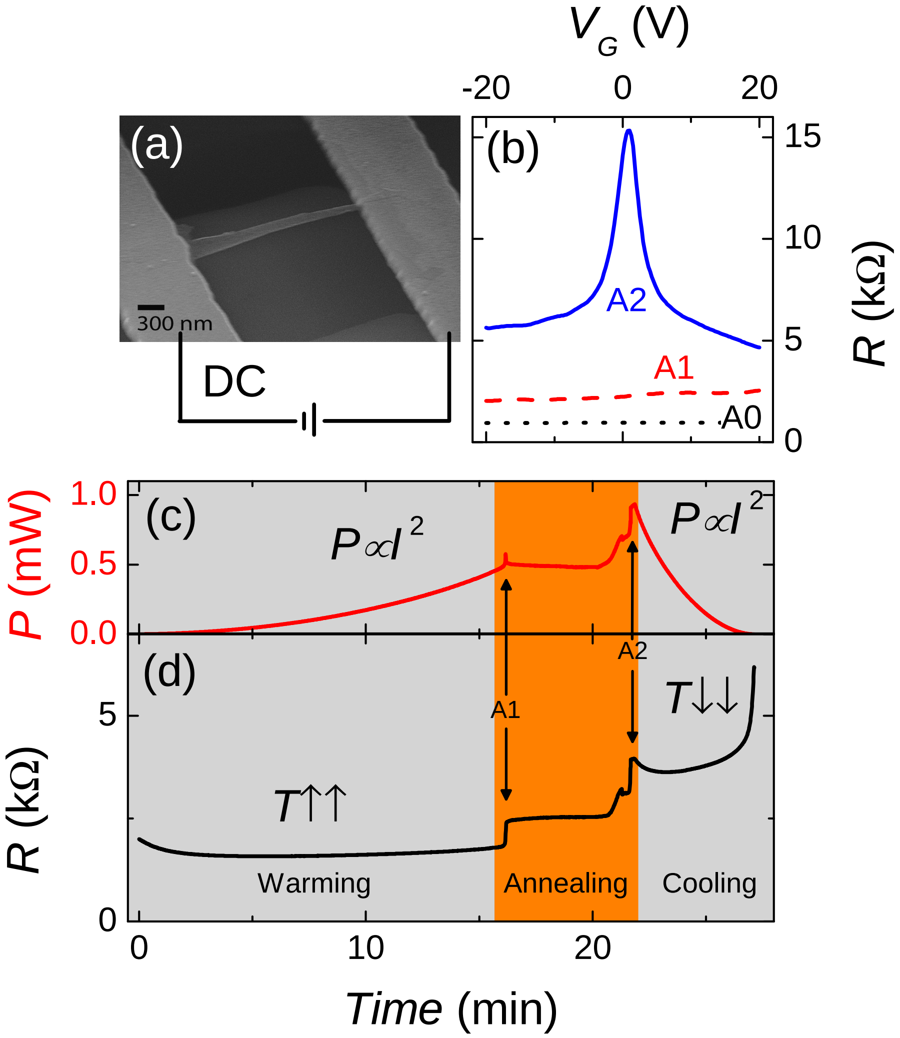

Figure 3.7: *(a) Schematic overview of current annealing over two-probe suspended sample. A dc voltage bias is slowly applied over a two-terminal device. (b) Two-step current annealing (A0 → A1 → A2) process resulting in moving the CNP closer to $V_G = 0$ V. (c) Power P applied over the sample as a function the time. (d) The resistance R by increasing the power P as in Fig. 3.7(c). Increasing of P leads to a temperature T increase (grey regions), and finally to a region in where T is high enough and the annealing is initiated (orange region).*

sample. For low dc-currents the finite voltage over the sample introduces a local gating effect, causing a decrease of R by moving even further away from the CNP. By increasing the current even further a power $P \propto I^2$ causes an increase of the local temperature. From a certain moment the temperature exceeds the value where the remaining inhomogeneities starts to evaporate. From here the process start to behave as a chain reaction: the evaporation causes the CNP to move to lower gate-voltage → the resistance R increases → the power P increases → the temperature T increases. From the moment that the resistance starts to increase rapidly the current is strongly reduced in order to keep the power P constant and avoid any further heating. In general the annealing is stabilized from here and the sample does not heat up more. Further increase of the temperature by increasing the power in step A2 is in general necessary to improve the quality of the device even more and approach $V_{CNP} = 0$ V.

3.7 Conclusion

We have presented how to process a rough flake of graphite into a working two-dimensional graphene field effect-transistor. By using different lithographic techniques we can process samples with specific properties in order to test its electronic properties. Additional we show how to increase the electronic properties by suspending the graphene membrane from the substrate and further improve the sample by using of either heat- or current annealing.

References

[1] K. S. Novoselov, A. K. Geim, S. V. Morozov, D. Jiang, Y. Zhang, S. V. Dubonos, I. V. Grigorieva, and A. A. Firsov, “Electric field effect in atomically thin carbon films”, *Science* **306**, 666–669 (2004).

[2] S. Russo, J. B. Oostinga, D. Wehenkel, H. B. Heersche, S. S. Sobhani, L. M. K. Vandersypen, and A. F. Morpurgo, “Observation of Aharonov-Bohm conductance oscillations in a graphene ring”, *Physical Review B* **77** (2008).

[3] Y. Zhao, P. Cadden-Zimansky, F. Ghahari, and P. Kim, “Magnetoresistance Measurements of Graphene at the Charge Neutrality Point”, *Physical Review Letters* **108**, 106804 (2012).

[4] J. Martin, N. Akerman, G. Ulbricht, T. Lohmann, J. H. Smet, K. von Klitzing, and A. Yacoby, “Observation of electron-hole puddles in graphene using a scanning single-electron transistor”, *Nature Physics* **4**, 144–148 (2008).

[5] http://www.graphit.de/

[6] http://www.covalent.co.jp/eng/products/semicon/carbon.html

[7] http://www.2spi.com/catalog/new/hopgsub.php

[8] R. R. Nair, P. Blake, A. N. Grigorenko, K. S. Novoselov, T. J. Booth, T. Stauber, N. M. R. Peres, and A. K. Geim, “Fine Structure Constant Defines Visual Transparency of Graphene”, *Science* **320**, 1308 (2008).

[9] P. Blake, E. W. Hill, A. H. C. Neto, K. S. Novoselov, D. Jiang, R. Yang, T. J. Booth, and A. K. Geim, “Making graphene visible”, *Applied Physics Letters* **91**, 063124 (2007).

[10] Z. H. Ni, H. M. Wang, J. Kasim, H. M. Fan, T. Yu, Y. H. Wu, Y. P. Feng, and Z. X. Shen, “Graphene Thickness Determination Using Reflection and Contrast Spectroscopy”, *Nano Letters* **7**, 2758–2763 (2007).

[11] “Handbook of optics”, McGraw Hill (2009).

[12] E. Palik, “Handbook of optical constants of solids”, New York: Academic Press (1991).

[13] A. C. Ferrari, J. C. Meyer, V. Scardaci, C. Casiraghi, M. Lazzeri, F. Mauri, S. Piscanec, D. Jiang, K. S. Novoselov, S. Roth, and A. K. Geim, "Raman Spectrum of Graphene and Graphene Layers", *Physical Review Letters* **97**, 187401 (2006).

[14] M. Ishigami, J. H. Chen, W. G. Cullen, M. S. Fuhrer, and E. D. Williams, "Atomic Structure of Graphene on SiO2", *Nano Letters* **7**, 1643–1648 (2007).

[15] A. M. Goossens, V. E. Calado, A. Barreiro, K. Watanabe, T. Taniguchi, and L. M. K. Vandersypen, "Mechanical cleaning of graphene", *Applied Physics Letters* **100**, 073110 (2012).

[16] E. Stolyarova, K. T. Rim, S. Ryu, J. Maultzsch, P. Kim, L. E. Brus, T. F. Heinz, M. S. Hybertsen, and G. W. Flynn, "High-resolution scanning tunneling microscopy imaging of mesoscopic graphene sheets on an insulating surface", *Proceedings of the National Academy of Sciences* **104**, 9209–9212 (2007).

[17] Z. H. Ni, H. M. Wang, Z. Q. Luo, Y. Y. Wang, T. Yu, Y. H. Wu, and Z. X. Shen, "The effect of vacuum annealing on graphene", *Journal of Raman Spectroscopy* **41**, 479–483 (2010).

[18] C. R. Dean, A. F. Young, I. Meric, C. Lee, L. Wang, S. Sorgenfrei, K. Watanabe, T. Taniguchi, P. Kim, K. L. Shepard, and J. Hone, "Boron nitride substrates for high-quality graphene electronics", *Nature Nanotechnology* **5**, 722–726 (2010).

[19] K. I. Bolotin, K. J. Sikes, Z. Jiang, M. Klima, G. Fudenberg, J. Hone, P. Kim, and H. L. Stormer, "Ultrahigh electron mobility in suspended graphene", *Solid State Communications* **146**, 351–355 (2008).

[20] N. Tombros, A. Veligura, J. Junesch, J. J. van den Berg, P. J. Zomer, M. Wojtaszek, I. J. V. Marun, H. T. Jonkman, and B. J. van Wees, "Large yield production of high mobility freely suspended graphene electronic devices on a polydimethylglutarimide based organic polymer", *Journal of Applied Physics* **109**, 093702 (2011).

[21] J. Moser, A. Barreiro, and A. Bachtold, "Current-induced cleaning of graphene", *Applied Physics Letters* **91**, 163513 (2007).

Chapter 4

Coexistence of electron and hole transport in graphene

Abstract

When sweeping the carrier concentration in monolayer graphene through the charge neutrality point, the experimentally measured Hall resistivity shows a smooth zero crossing. Using a two-component model of coexisting electrons and holes around the charge neutrality point, we unambiguously show that both types of carriers are simultaneously present. Furthermore the absence of a diverging Hall-resistance near the CNP points to the existence of a quantum Hall metal state at $\nu = 0$ made up by both electrons and holes.

Part of this work has been published in: S. Wiedmann, H. J. van Elferen, et al., *Coexistence of electron and hole transport in graphene*, Physical Review B **84**, 115314 (2011)

4.1 Introduction

The carrier concentration in semiconductors is commonly measured using the Hall effect based on the Lorentz force exerted on moving charged particles in a perpendicular magnetic field.[1] In conventional finite-gap semiconductors, the low-temperature Hall resistivity ρ_{xy} directly measures either the electron or the hole density. However, in compensated semiconductors, where electrons and holes coexist, the Hall resistivity is determined by *both* types of carriers and, in particular, becomes zero in a fully compensated material.
Graphene is an ideal two-dimensional zero-gap semiconductor with a linear dispersion[2] where the electron and hole concentration at $T = 0$ K go to zero when sweeping the carrier density through the charge neutrality point (CNP). However, non-perfect samples with random potential fluctuations will break up into spatially inhomogeneous conducting electron-hole puddles[3] leaving a finite number of electrons and holes directly at the CNP.

In this chapter, we present experimental results on the Hall resistivity ρ_{xy} in graphene around the CNP in magnetic fields up to 30 T and for temperatures down to 0.5 K. We demonstrate that the smooth zero-crossing of ρ_{xy} at the CNP for all magnetic fields is caused by a finite concentration of both electrons and holes below and above the CNP with an equal number of electron and hole states occupied at the CNP.
We have investigated three different graphene devices made from Kish graphite (sample A) and natural graphite (samples B and C) with mobilities between $\mu = 0.8$ m^{2}V^{-1}s^{-1} for sample A and $\mu = 1$ m^{2}V^{-1}s^{-1} for samples B and C. Single layer graphene flakes were deposited on a Si/SiO$_2$ substrate, identified optically[4] and patterned using standard techniques [see section 3.4].[2,5] The total charge-carrier concentration q in the graphene films, defined as $q \equiv n - p \simeq \alpha V_G$, can be adjusted from hole-doped ($q < 0$) to electron doped ($q > 0$) by means of a back-gate voltage V_G [see section 3.2]. Here n and p are the carrier concentrations for electrons and holes, respectively, and $\alpha = 7.2 \times 10^{14}$ m^{-2} V^{-1} for a 300 nm thick SiO$_2$ gate insulator. In order to remove surface impurities, all devices were annealed at 440 K prior to the low-temperature measurements [see section 3.5]. Admixtures of ρ_{xx} to ρ_{xy} due to contact misalignment and inhomogeneities we removed by symmetrization of all traces measured in positive and negative magnetic fields.

In section 4.2 we present our experimental results. The first part of section 4.2 shows transport measurements at low magnetic fields where the Hall resistance is not yet quantized and charge carriers can be considered as “free” (mobile).

The second part presents data up to 30 T in the quantum Hall (QH) regime. Section 4.3 develops a model for the density of states in graphene, first applied to our samples and then we discuss different splitting scenarios of the lowest Landau level.

4.2 Experimental results

We first present measurements of the Hall resistivity ρ_{xy} with increasing magnetic field in Fig. 4.1(a) for sample A as a function of total carrier concentration q for several magnetic fields at $T = 1.3$ K. The corresponding back-gate voltage V_G is displayed on the top-axis. For $B = 15$ T, ρ_{xy} exhibits Hall plateaus quantized to $\rho_{xy} = \pm h/2e^2$ at filling factors $\nu = \pm 2$ [see section 2.4.2 for theoretical/experimental review]. For all magnetic fields, the Hall resistance is not diverging at the CNP when either electron or hole states are depleted. ρ_{xy} rather moves smoothly through zero from the $\nu = -2$ plateau to the $\nu = +2$ plateau.

In order to accommodate for this simple experimental observation, we describe the inverse Hall coefficient $1/R_H = B/\rho_{xy}$ with a two carrier model for electrons and holes as known for compensated semiconductors.[6]

$$\frac{1}{R_H} = \frac{e(n\mu_n + p\mu_p)^2}{n\mu_n^2 - p\mu_p^2} \tag{4.1}$$

Here n and p are the electron and hole concentrations and μ_e and μ_h are the electron and hole mobilities, respectively. In our graphene samples the measured conductivity as a function of carrier concentration is symmetric around the CNP and we can therefore assume the same mobility for both electrons and holes, $\mu_n = \mu_p$, and Eq. (4.1) simplifies to

$$\frac{1}{R_H} = \frac{e(n+p)^2}{(n-p)} \tag{4.2}$$

It is worth emphasizing that we can apply the two carrier model despite the presence of electron-hole puddles which would result, for conventional non-relativistic charge carriers, in spatial separation and related percolation phenomena in electron and hole regions. In the two-dimensional case, the percolation over electron puddles blocks unavoidably the transport for holes, and vice versa. The case of graphene is dramatically different. The crucial point is that for graphene the borders between p and n regions are actually transparent, and electrons and holes transfer smoothly into each other, which is referred to as

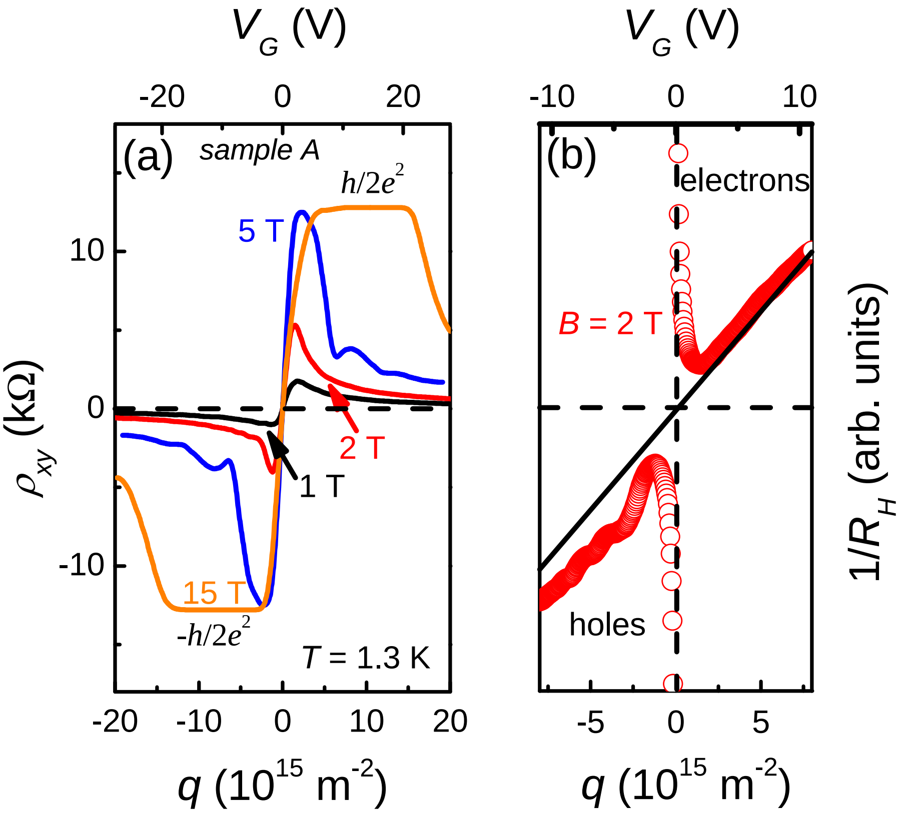

Figure 4.1: *(a) Dependence of ρ_{xy} in sample A on the carrier concentration (bottom axis) or on the back-gate voltage V_G (top axis) for several magnetic fields at $T = 1.3$ K. (b) Inverse Hall coefficient $1/R_H$ as a function of q for $B = 2$ T. The solid line shows the expected behavior of a conventional zero-gap semiconductor where electrons and holes get fully depleted at the CNP.*

Klein tunnelling.[7] At specific magic angles of incidence (including normal incidence) the transmission probability is 100% . The presence of a magnetic field does not destroy the Klein tunneling but just shifts the magic angles.[8] It can be assumed that tunneling from one electron puddle to the other electron pud-

dle always remains possible even for carriers incident to an oblique angle (the same holds for hole transport). Thus, even under a nonuniform distribution of electron-hole puddles, we can apply our two-carrier model to graphene.
Fig. 4.1(b) shows the inverse Hall coefficient $1/R_H$ as a function of q for $B = 2$ T extracted from our measurements. For high q, $1/R_H$ exhibits a linear increase due to the presence of either electrons ($q > 0$) or holes ($q < 0$). For the CNP, where $n = p$ and $q = n - p = 0$, $R_H \to 0$, which leads to divergence of $\frac{1}{R_H}$, but only provided that $n+p$ is not equal to 0. This implies that n and p both remain finite at the CNP. Therefore such a divergence of $\frac{1}{R_H}$ indicates simultaneous presence of electrons and holes at the CNP.

4.2.1 Low magnetic fields

We now present low-field data in Fig. 4.2 for sample B measured at 0.5 K and in magnetic fields where the QHE is not yet developed. Using Eq. (4.2) we extract the individual charge carrier concentrations n and p as a function of the total charge density q [see Fig. 4.2(b)].
Both charge carriers are present above and below the CNP and the electron (hole) concentration already starts to increase as the hole (electron) concentration is still decreasing. Precisely at the CNP, we extract a charge carrier concentration $n(q = 0) = p(q = 0) = 4.2 \times 10^{14}$ m^{-2} only weakly dependent on B for $0 < B < 4$ T. Away from the CNP, the system remains two-component and the minority charge carriers only disappear for $|q| > 2 \times 10^{15}$ m^{-2}. The same analysis for the other two samples qualitatively yields similar results with $n(q = 0) = p(q = 0) = 7.4 \times 10^{14}$ m^{-2} for sample A and $n(q = 0) = p(q = 0) \simeq 5 \cdot 10^{14}$ m^{-2} for sample C. The fact that the sample with the lowest mobility (sample A) reveals the highest $n(q = 0)$ qualitatively confirms a scenario of coexisting electron-hole puddles, where lower mobilities are generally associated with larger potential fluctuations.

4.2.2 Quantum Hall regime

We now move our attention to measurements in high magnetic fields. In Fig. 4.3(a/b) we present experimental data from 5 to 25 T both for longitudinal resistivity ρ_{xx} and Hall resistivity ρ_{xy}, measured in sample C at $T = 4.2$ K. ρ_{xy} is measured from $B = 5$ T up to 25 T in steps of 5 T. ρ_{xy} is now quantized at $\nu = \pm 2$ but still shows a smooth zero-crossing from $\rho_{xy} = -h/2e^2$ to $\rho_{xy} = +h/2e^2$ without any sign of divergence at the CNP. Consequently, the smooth crossing around zero gate voltage points still to a finite charge carrier concentration for electrons and holes around the CNP. Therefore, we can con-

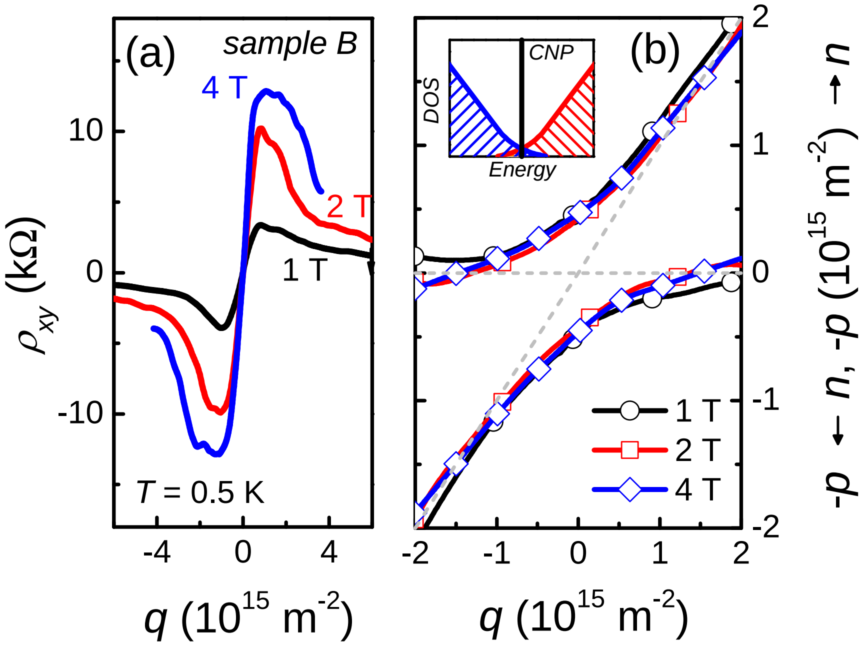

Figure 4.2: *(a) Low-field Hall resistivity ρ_{xy} and (b) extracted carrier concentration for electrons n and holes p as a function of total charge q according to Eq. (4.2) for sample B. Both types of charge carriers are present for $|q| < 2 \cdot 10^{15}$ m^{-2}. Inset: Sketch of the DOS for $B = 0$ at the CNP.*

clude that electrons still contribute to conduction below $E = 0$ and holes do so above $E = 0$.

4.3 Density of states model

4.3.1 Investigated samples

The above measurements allow us to sketch the density of states (DOS) for electrons and holes. For $B = 0$ [see inset to Fig. 4.2] the DOS in graphene $D(E) = 2|E|/\pi(\hbar v_F)^2$ (v_F is the Fermi velocity) is smeared out around the CNP due to the presence of electron-hole puddles. Applying a magnetic field leads to a quantization of the DOS, shown in Fig. 4.4(a). Electrons and holes in the center of the Landau levels are extended (shaded areas) whereas they are localized in the Landau level tails (filled areas). In that picture the Landau levels $N = 0$ and $N = 1$ are well separated, yielding quantized plateaus in ρ_{xy}

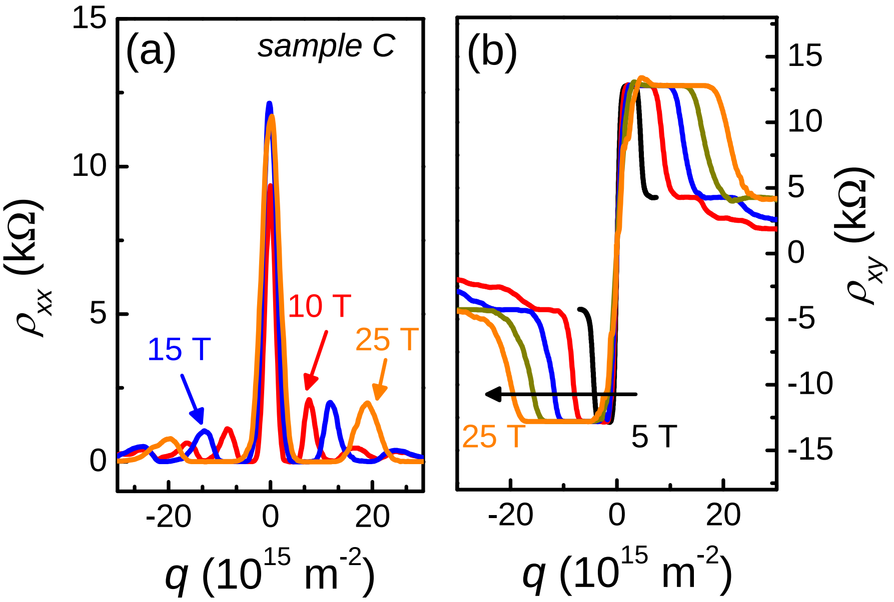

Figure 4.3: *High-field Hall resistivity ρ_{xy} (b) and longitudinal resistivity ρ_{xx} (a) of sample C at 4.2 K for different magnetic fields.*

at $\nu = \pm 2$ [Fig. 4.3(b)] when the Fermi energy is situated in the localized tails of the Landau levels.

Within this DOS model, see also Ref. 9, we can now calculate the longitudinal conductivity σ_{xx} by means of the Kubo-Greenwood formalism[10,11] and the Hall conductivity σ_{xy} summing up all states below the Fermi energy.[12] Including the presence of electrons and holes above and below the CNP indeed yields a smooth zero crossing of ρ_{xy} as measured in Fig. 4.3(b) and modeled in Fig. 4.4(b).

Our experimental observation of coexisting electrons and holes around the CNP also has a direct implication on the nature of the $\nu = 0$ QHE in graphene.[13] Neither a gap opening at the CNP[9] nor a complete lifting of spin and valley degeneracy, if we assume the spin first scenario of the zeroth Landau level,[14] fundamentally change the zero-crossing of the Hall resistance. Our experimental results up to a magnetic field 30 T do not show any evidence of broken degenerated states, e.g. showing additional quantized states apart from filling factors $\nu = \pm 2, \pm 6, \pm 10, \ldots$. Further improvement of the sample mobility leads

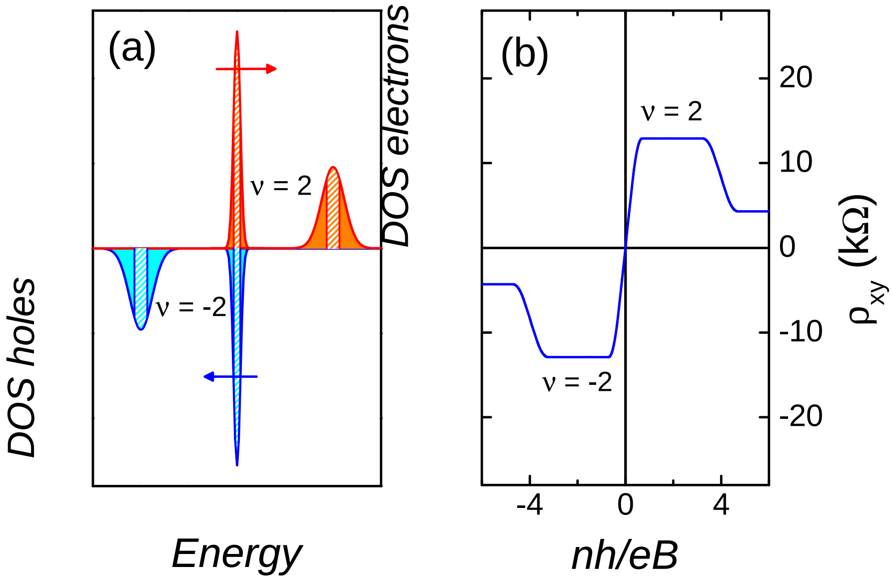

Figure 4.4: *(a) Four-fold degenerate zeroth Landau levels with coexisting electrons and holes below and above the CNP (the electron levels (red) are sketched upwards and the hole levels (blue) are sketched downwards). (b) Smooth zero-crossing of the Hall resistance from $\nu = -2$ to $\nu = 2$.*

to less scattering and therefore smaller energy level broadening. These samples[14] therefore show quantized energy-states between $\nu = \pm 2, \pm 6, \pm 10, ...$, i.e. broken spin and/or valley degeneracy. These states are in general suppressed or stimulated by different interaction phenomena, like ferromagnetic coupling of the charge carriers.[15]

4.3.2 Splitting scenarios of the lowest Landau level

For high mobility graphene samples[14, 16–19] spin and valley degeneracies are lifted. As demonstrated in Ref. 14, the Hall resistivity exhibits a smooth zero-crossing (with fluctuations) from the $\nu = -1$ plateau to the $\nu = 1$ plateau with increasing V_g. We have calculated the DOS assuming that both electrons and holes are simultaneously present above and below the CNP and find the smooth zero-crossing of the Hall resistivity.

Furthermore, we use our DOS model to directly address the question wether $\nu = 0$ is a QH-metal or a QH-insulator. Measurements of longitudinal resis-

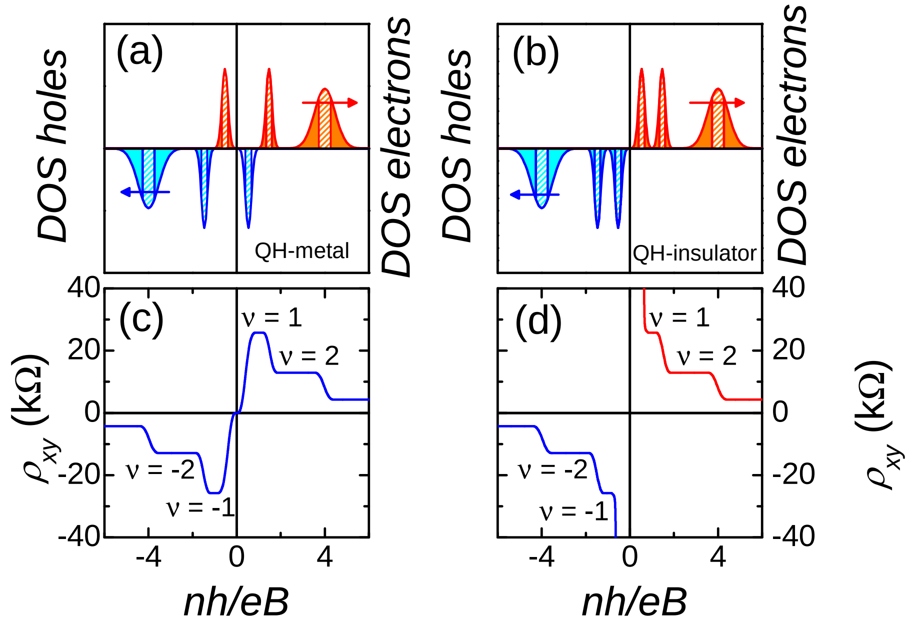

Figure 4.5: *Sketched DOS for (a) a QH-metal and (b) a QH-insulator if both spin and valley splitting is resolved. (c) Smooth zero-crossing of the Hall resistivity if both charge carriers are present above and below the CNP and (d) diverging* ρ_{xy} *due to electrons and holes being separated and residing on different sides of the CNP.*

tance have shown either finite ρ_{xx}, even subjected to high magnetic fields (QH-metal)[14, 20–22] or a steeply increase in ρ_{xx}, attributed to an insulating ground state.[23] The first observation is generally explained in the frame of edge states model.[24] According to this model, in high magnetic fields the bulk becomes insulating due to the circular motion of the charge carriers. In this case charge carriers propagate along the edges, formed by skipping orbits.[25] Both scenarios are directly related to the lifting of the degeneracy of the zeroth Landau level. Whereas in a QH-metal spin splitting is larger than valley splitting, in a QH-insulator the contrary is the case. If spin and valley degeneracy are lifted, a zero-crossing of ρ_{xy} is observed if we include the presence of electrons and holes above and below the CNP [Fig. 4.5(a) and (c)]. However, if we separate electrons and holes at the CNP, see Fig. 4.5(b) (valley first scenario), ρ_{xy} diverges [Fig. 4.5(d)]. The divergence of ρ_{xy} in the valley first scenario beyond filling factor $\nu = 1$ when approaching the CNP has indeed been recently found in high mobility graphene devices, fabricated on a single crystal boron nitride substrate[19] and thus confirm our DOS model.

4.4 Conclusion

In conclusion, we have performed measurements of the Hall resistivity in graphene in a magnetic field up to 30 T. ρ_{xy} does not diverge at the CNP but shows a smooth transition from electrons to holes. Our analysis based on mixed conduction at the CNP implies that both electrons and holes exist both below and above the CNP with as many hole states as electron states occupied at the CNP. Taking into account the presence of both charge carriers above and below the CNP contributes to a better understanding of the unique nature of electronic states at the lowest Landau level in graphene.

Finally, we have to point out that physics around the CNP, such as the behavior of ρ_{xy} from hole-dominated to electron-dominated transport becomes easier to access with high-mobility samples even though diverging ρ_{xx} directly affects the extraction of Hall resistivity under realistic experimental conditions.

References

[1] E. Hall, “On a New Action of the Magnet on Electric Currents”, *American Journal of Mathematics* **2**, 287–292 (1879).

[2] A. K. Geim and K. S. Novoselov, “The rise of graphene”, *Nature Materials* **6**, 183–191 (2007).

[3] J. Martin, N. Akerman, G. Ulbricht, T. Lohmann, J. H. Smet, K. von Klitzing, and A. Yacoby, “Observation of electron-hole puddles in graphene using a scanning single-electron transistor”, *Nature Physics* **4**, 144–148 (2008).

[4] P. Blake, E. W. Hill, A. H. C. Neto, K. S. Novoselov, D. Jiang, R. Yang, T. J. Booth, and A. K. Geim, “Making graphene visible”, *Applied Physics Letters* **91**, 063124 (2007).

[5] K. S. Novoselov, A. K. Geim, S. V. Morozov, D. Jiang, Y. Zhang, S. V. Dubonos, I. V. Grigorieva, and A. A. Firsov, “Electric field effect in atomically thin carbon films”, *Science* **306**, 666–669 (2004).

[6] K. Seeger, “Semiconductor physics, an introduction”, Berlin: Springer (1997).

[7] M. I. Katsnelson, K. S. Novoselov, and A. K. Geim, “Chiral tunnelling and the Klein paradox in graphene”, *Nature Physics* **2**, 620–625 (2006).

[8] A. F. Young and P. Kim, “Quantum interference and Klein tunnelling in graphene heterojunctions”, *Nature Physics* **5**, 222–226 (2009).

[9] A. J. M. Giesbers, L. A. Ponomarenko, K. S. Novoselov, A. K. Geim, M. I. Katsnelson, J. C. Maan, and U. Zeitler, “Gap opening in the zeroth Landau level of graphene”, *Physical Review B* **80**, 201403 (2009).

[10] R. Kubo, “A General Expression for the Conductivity Tensor”, *Canadian Journal of Physics* **34**, 1274–1277 (1956).

[11] D. A. Greenwood, “The Boltzmann Equation in the Theory of Electrical Conduction in Metals ”, *Proceedings Physical Society London* **71**, 585 (1958).

[12] P. Streda, “Quantized Hall-Effect in a Two-Dimensional Periodic Potential”, *Journal of Physics C-Solid State Physics* **15**, 1299–1303 (1982).

[13] S. Das Sarma and K. Yang, "The enigma of the quantum Hall effect in graphene", *Solid State Communications* **149**, 1502–1506 (2009).

[14] Y. Zhang, Z. Jiang, J. P. Small, M. S. Purewal, Y. W. Tan, M. Fazlollahi, J. D. Chudow, J. A. Jaszczak, H. L. Stormer, and P. Kim, "Landau-Level Splitting in Graphene in High Magnetic Fields", *Physical Review Letters* **96**, 136806 (2006).

[15] K. Nomura and A. H. MacDonald, "Quantum Hall Ferromagnetism in Graphene", *Physical Review Letters* **96**, 256602 (2006).

[16] K. I. Bolotin, F. Ghahari, M. D. Shulman, H. L. Stormer, and P. Kim, "Observation of the fractional quantum Hall effect in graphene", *Nature* **475**, 196–199 (2011).

[17] C. R. Dean, A. F. Young, I. Meric, C. Lee, L. Wang, S. Sorgenfrei, K. Watanabe, T. Taniguchi, P. Kim, K. L. Shepard, and J. Hone, "Boron nitride substrates for high-quality graphene electronics", *Nature Nanotechnology* **5**, 722–726 (2010).

[18] X. Du, I. Skachko, F. Duerr, A. Luican, and E. Y. Andrei, "Fractional quantum Hall effect and insulating phase of Dirac electrons in graphene", *Nature* **462**, 192–195 (2009).

[19] C. R. Dean, A. F. Young, P. Cadden-Zimansky, L. Wang, H. Ren, K. Watanabe, T. Taniguchi, P. Kim, J. Hone, and K. L. Shepard, "Multicomponent fractional quantum Hall effect in graphene", *Nature Physics* **7**, 693696 (2011).

[20] K. S. Novoselov, A. K. Geim, S. V. Morozov, D. Jiang, M. I. Katsnelson, I. V. Grigorieva, S. V. Dubonos, and A. A. Firsov, "Two-dimensional gas of massless Dirac fermions in graphene", *Nature* **438**, 197–200 (2005).

[21] Y. Zhang, Y.-W. Tan, H. L. Stormer, and P. Kim, "Experimental observation of the quantum Hall effect and Berry's phase in graphene", *Nature* **438**, 201–204 (2005).

[22] D. A. Abanin, K. S. Novoselov, U. Zeitler, P. A. Lee, A. K. Geim, and L. S. Levitov, "Dissipative Quantum Hall Effect in Graphene near the Dirac Point", *Physical Review Letters* **98**, 196806 (2007).

[23] J. G. Checkelsky, L. Li, and N. P. Ong, "Zero-Energy State in Graphene in a High Magnetic Field", *Physical Review Letters* **100**, 206801 (2008).

[24] E. Fawcett and J. Walsh, W. M., “Cyclotron Resonance in Tungsten”, *Physical Review Letters* **8**, 476–478 (1962).

[25] R. J. Haug, “Edge-State Transport and Its Experimental Consequences in High Magnetic-Fields”, *Semiconductor Science and Technology* **8**, 131–153 (1993).

Chapter 5

Field induced quantum-Hall ferromagnetism in suspended bilayer graphene

Abstract

We have measured the magneto-resistance of freely suspended high-mobility bilayer graphene. For magnetic fields $B \geq 1$ T we observe the opening of a field-induced gap at the charge neutrality point characterized by a diverging resistance. For higher fields the eight-fold degenerated lowest Landau level lifts completely. Both the sequence of this symmetry breaking and the strong transition of the gap-size point to a ferromagnetic nature of the insulating phase developing at the charge neutrality point.

Part of this work has been published in: H.J. van Elferen et al., *Field-induced quantum Hall ferromagnetism in suspended bilayer graphene*, Physical Review B **85**, 115408 (2012)

5.1 Introduction

The unique electronic properties of monolayer and bilayer graphene makes them promising candidates for future applications in nanotechnology. Though (bilayer) graphene on a SiO_2-substrate can show a mobility up to 2 m^2/Vs,[1] much cleaner and higher mobility samples are required in order to investigate its intrinsic properties, and, in particular, electron interaction effects. Mobilities exceeding 10 m^2/Vs can be obtained by removing the SiO_2 substrate underneath the graphene[2,3] or by depositing graphene on a boron nitride crystal.[4] These high-mobility samples display new interaction-induced phenomena such as a fractional quantum Hall effect,[5–7] broken-symmetry states,[8] a magnetic-field-induced insulating phase,[8] and quantized conductance at zero magnetic field.[9]

In the two-dimensional electron system of bilayer graphene (BLG) the application of a perpendicular magnetic field results into an unconventional integer quantum Hall effect with plateaus at filling factors $\nu = \pm 4, \pm 8, \pm 12$, ...[10] [see section 2.4.3] The lowest Landau level is eight-fold degenerate, owing to spin, valley, and layer-index degrees of freedom. In standard BLG samples deposited on SiO_2, magnetic fields above 10 T are required to observe fully quantized plateaus and the eight-fold degeneracy of the lowest Landau level is only lifted for the highest quality samples at magnetic fields exceeding 20 T.[11] At 0 T the density of states in BLG does not vanish at the charge neutrality point (CNP), in contrast to single-layer graphene. Therefore, even arbitrarily weak interaction between charge from conduction and valence band states will trigger excitonic instabilities which causes a variety of gapped states.[12–16] Recent experiments[17–19] have indicated that the nature of the gapped state at the CNP is strongly related to the exchange interaction in the sample. With use of a top-gate bilayer graphene is brought into different ground-states, from a zero field gapped state to a non-gapped state. These different ground-states have a different response in magnetic field. In this chapter and chapter 6 we study two of these different ground-states of suspended bilayer graphene which gave similar conclusions as the study in Ref. 20. In particular in this chapter we present two-terminal magnetotransport experiments in suspended BLG at temperatures ranging from 1.3 to 4.2 K and magnetic fields up to 30 T. We observe a sudden gap opening at the CNP already for $B \geq 1$ T and the appearance of broken-symmetry states at filling factors $\nu = \pm 1, \pm 2, \pm 3$ for higher fields. Detailed investigation of the energy gap at filling factor $\nu = 0$ reveals an exchange-interaction driven linear scaling at low magnetic fields, in agreement with earlier reported results.[8] At high fields we observe the cross-over to a much smaller gap. This high field transition and the appearance of broken symmetry states at $\nu = 1, 2, 3$ are consistent with the formation of a quantum Hall ferromagnetic state.[13, 21]

5.2 Experimental background

We have prepared a suspended BLG sample using an acid free method.[22] Following standard techniques,[23] we first exfoliated flakes from highly oriented pyrolytic graphite (HOPG) and deposited them on a Si/SiO$_2$ substrate covered with a 1.15 μm thick LOR-A resist layer. Bilayer flakes were then identified by their optical contrast.[24] Subsequently, two electron beam lithography steps were performed in order to contact the flakes with Ti-Au contacts and to remove part of the LOR-A below the graphene flakes. The resulting device is freely suspended across a trench formed in the LOR-A with two metallic contacts on each side, see right inset of Fig. 5.1 [section 3.6 and Ref. 9 for more details]. Charge carriers in the BLG sheet can be induced by applying a back-gate voltage V_G on the highly n-doped Si wafer. The geometrical gate capacitance is given by a combination of the vacuum gap (1.15 μm) and SiO$_2$ substrate (0.5 μm). Using a serial capacitor model we calculate a gate capacitance of 7.2 aF/μm^{-2} which directly relates the carrier concentration to V_G as $n = \alpha(V_G - V_{CNP})$ with leverage factor $\alpha = 0.5 \times 10^{14}$ m^{-2}V^{-1} and a finite voltage of the the CNP of $V_{CNP} = 1.2$ V [see section 3.2 for more experimental background]. In high magnetic fields, the geometric capacitance increases due to the formation of edge states[25] and α becomes dependent on B. Therefore, the exact values of capacitance were determined experimentally by identifying the filling factors of quantized Hall plateaus in magnetic field [details on this procedure can be found in Appendix B].

After mounting, the devices were slowly cooled down to 4.2 K and current annealed[26] by applying a dc bias current up to 3 mA [more experimental background on this annealing procedure can be found in section 3.6]. This local annealing resulted into the high quality sample with mobility $\mu \approx 10$ m^2/Vs at a charge carrier density $n = 2 \times 10^{15}$ m^{-2}. The value of the mobility is calculated based on the dimension of suspended graphene before current annealing: 0.3 μm wide and 2.1 μm long. However, in the membrane the distribution of the temperature while current annealing is non homogenous,[9] which most probably leads to the middle part of the membrane being annealed and non annealed regions close by the contacts. In this case the estimation of the mobility value based on geometrical dimensions might not be precise. We can also estimate the quality of the obtained sample from the value of the magnetic field at which the system enters the quantum Hall regime ($B > 0.5$ T). Assuming $\mu B \gg 1$ for QHE to exist,[2] the observation applies a lower bound for the mobility of 2 m^2/Vs.

Measurements were performed with standard low-frequency lock-in techniques in two-probe geometry with an excitation current of 2 nA.

5.3 Magnetotransport properties at low carrier concentration

In Fig. 5.1 we show the data for the two-point resistance R of our suspended BLG device at $B = 0$ T and $B = 1$ T as a function of V_G (top x-axis) and n (bottom x-axis), respectively. The two-probe resistance R is characterized by a magnetoresistance $\rho_{xx} = L/w \cdot R_{xx}$ with superimposed Hall-resistance $\rho_{xy} = R_{xy}$, $R = w/L \cdot \rho_{xx} + \rho_{xy}$. Here $L/w \approx 6.7$ is the aspect ratio of the device. The traces are corrected by phenomenological contact resistances (1 kΩ on the electron side and 1.7 kΩ on hole side) which were determined from a finite resistance background observed at high carrier concentrations; this background resistance increases by about a factor 2 in the range $B = 0...30$ T. These contact resistances most probably originate from in-series connected non-annealed parts of the sample,[27] contact doping,[28,29] and the finite resistance of the current leads. The sharp maximum at the CNP of the zero-field data already indicates the high electronic quality of the sample. At 1 T the resistance already exhibits fully quantized plateaus at filling factors $\nu = 4$ and a developing quantization at $\nu = 8$ and $\nu = 12$. The formation of these plateaus is caused by a quantization of $\rho_{xy} = h/\nu e^2$ and the associated zero minima in ρ_{xx} when the Fermi energy lies between two Landau levels[10] and confirms the high electronic mobility ($\mu \gg 1/B$) of our device required to observe this unconventional quantum Hall effect. Additionally, as soon as a finite magnetic field is applied, the resistance at the CNP, R_{CNP}, starts to diverge. Whereas at zero magnetic field R_{CNP} is only very weakly temperature dependent and comparable to the resistance quantum, already at 1 T it is nearly an order of magnitude higher and starts to increase strongly with decreasing temperature [see left inset in Fig. 5.1]. The nature of the gap opening at the CNP is elucidated further in Fig. 5.2(a) where we show the resistance as a function of carrier concentration n for several magnetic fields. The diverging resistance at the CNP appears at a similar magnetic field as the plateaus at filling factors -4 and 4; i. e. the eight-fold degeneracy of the zero-energy Landau level breaks directly into two four-fold degenerated Landau levels, as already predicted theoretically[30] and proven experimentally.[19] At low fields $B < 0.1$ T we observe a small decrease of the resistance maximum at

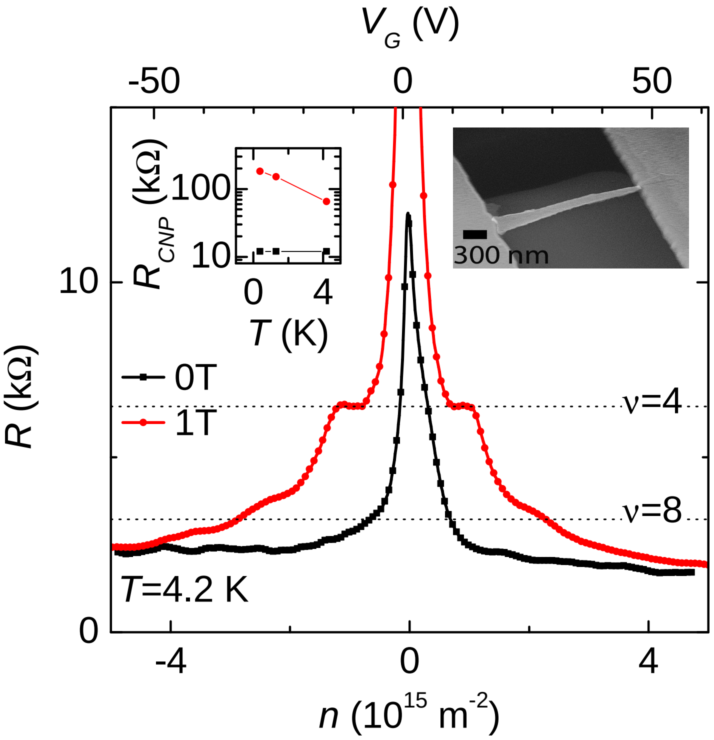

Figure 5.1: *Resistance as a function of the concentration by sweeping the backgate from -60 V to 60 V for 0 T (■) and 1 T (●). A constant contact resistance has been removed. top-left inset: Temperature dependence of the resistance at the CNP for 0 T and 1 T; top-right inset: SEM picture of our suspended device.*

the CNP (not shown in the figure). This small decrease in resistance can be explained by the presence of local inhomogeneities which give a small splitting between the valley-polarized energies; the crossover of these energy states at finite magnetic field results in a resistance minimum. When the magnetic field is above $B \geq 0.1$ T we observe a rapid increase of the resistance-maximum at the CNP, shown in Fig. 5.2(c). Before we move to the quantification of our gap-opening we briefly summarize all energy-scales in bilayer graphene in table 5.1, which gives an impression of the relative size of the different energy-scales. We interpret the rapid increase of R_{CNP} as a result of the spin-splitting (S) of the two energy levels at zero energy [see right Fig. 5.2(b)] or by a disorder

Mechanism	**Energy scale**
Nearest neighbour interaction	$\gamma_0 = 3.2$ eV
Layer coupling	$\gamma_1 = 0.4$ eV
Landau level spacing	$\Delta E \approx \hbar\omega_c = 10.9$ meV/T $\cdot B$
Zeeman splitting	$\Delta_S = g\mu_B B = 0.12$ meV/T $\cdot B$
Exchange/Interaction energy	$E_{ex} \propto e^2/l_B \approx 2...12$ meV/T$^{1/2}$ $\cdot\sqrt{B}$
Coulomb energy	$E_C = e^2/\epsilon_r l_B = 56$ meV
Lattice effects (anisotropy, etc.)	$E_{lattice} \propto a/l_B \approx 0.005$ meV/T$^{1/2}$ $\cdot\sqrt{B}$
Landau level broadening	$\Gamma \propto 0.1...5$ meV/T$^{1/2}$ $\cdot\sqrt{B}$

Table 5.1: *Energy scales in bilayer graphene with the magnetic field B in T.*

enhanced valley-splitting (V) [i.e. unevenly charged top and bottom layer, see left Fig. 5.2(b)]. The valley scenario would lead to a strong temperature dependence at zero field and ultimately for a big disorder to an insulating state at zero field, as discussed in chapter 6. The absence of a temperature influence at 0 T and the CNP centered at very low gate-voltage points to a non-disordered bilayer, therefore we interpret the rapid increase by a result of spin splitting. As we discussed briefly in the introduction the presence of inhomogeneities or a local applied electric field leads to triggering of different ground-states. Theoretically this is expected to cause a big variety of ground-states[31] which we will discuss in more detail in chapter 6.

The absence of an energy-level at $E = 0$ in the inset of Fig. 5.2(c) results in a diverging resistance at the CNP. The resistance R_{CNP} at the CNP follows a classical Ahrrenius-activation behavior $R_{xx} \propto \exp(\Delta/k_BT)$, where Δ is a scale for the size of the gap. The resistance increase scales best with $\ln(R) \propto B/T$, from which we obtain a gap $\Delta = 0.34$ meV/T $\times B$. According to table 5.1 this gap is about a factor 3 times larger than the Zeeman-splitting $g\mu_B B$, which can be explained by the dominating exchange energy.[32] Eq. (5.1) describes the total spin energy Δ_S, determined by the sum of the single electron Zeeman energy $g\mu_B B$ and the exchange energy $E_{ex} \cdot (n_\uparrow - n_\downarrow)$. Here $n_\uparrow - n_\downarrow$ is the normalized difference between spin-up and spin-down occupation.

$$\Delta_S = g\mu_B B + E_{ex} \cdot (n_\uparrow - n_\downarrow) \tag{5.1}$$

At low fields the two energy levels are still overlapping and the system is not fully spin polarized, $(n_\uparrow - n_\downarrow) < 1$. Assuming Gaussian shaped Landau levels we can approximate $(n_\uparrow - n_\downarrow) = \frac{\sqrt{2}}{\pi}\frac{\Delta_S}{\Gamma}$ which leads with help of Eq. (5.1) to the

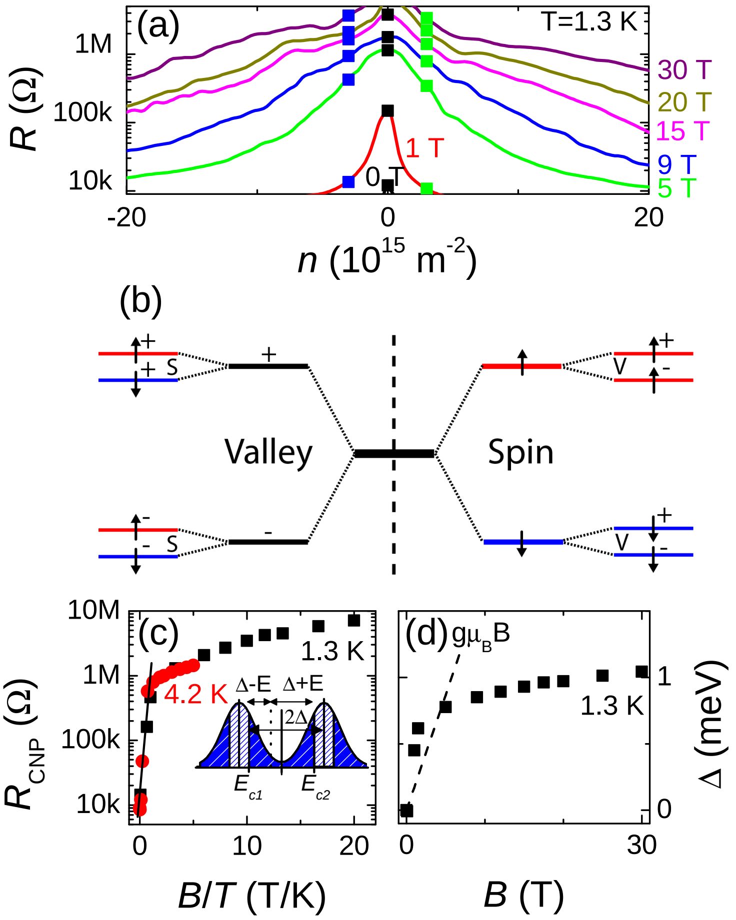

Figure 5.2: *(a) Resistive behavior of the sample near the CNP at $T = 1.3$ K. The dots mark the positions $n = 3 \times 10^{14}$ (green 🟩), 0 (black ■) and -3 $\times 10^{14}$ m^{-2} (blue 🟦) where the gap opening has been analyzed (see text for more details). (b) Splitting of the lowest Landau of bilayer graphene, taking into account spin (S) and valley (V) splitting. Filling factor $\nu = 0$ is either determined by valley-splitting V (left, marked by + and $-$) or spin-splitting S (right, marked by ↑ and ↓). (c) Resistance R_{CNP} as a function of B/T at $T = 4.2$ K (red •) and 1.3 K (black ■); inset: qualitative picture of the DOS near the CNP. The conduction at energy E is directly related to the thermal excitation of electrons to the conduction edges E_{c1} and E_{c2}. (d) Calculated gap Δ as a function of field B for $T = 1.3$ K; the dashed line represents the theoretical single electron Zeeman-energy $g\mu_B B$.*

gap $\Delta_S = \frac{g\mu_B B}{1-E_{ex}/\Gamma}$. The observed spin-enhancement by a factor 3 corresponds to a typical level width $\Gamma = 2$ meV and an exchange energy $E_{ex} = 1.3$ meV for $B = 1$ T corresponding to a value of about 2 % of the Coulomb energy $E_C = e^2/\epsilon_r l_B = 56$ meV, where l_B is the magnetic length.

The behavior at the high magnetic field is experimentally more complicated to access, because the measured resistance rapidly exceeds several MΩs and a quantitative analysis becomes difficult. However away from the CNP the measured resistances stay low enough to guarantee a reliable interpretation up to the highest magnetic fields. This situation is illustrated in the inset of Fig. 5.2(c) where we sketch the quantized density of states in the lowest Landau level around the CNP with a gap 2Δ opening at $E = 0$. When the Fermi energy is located at a finite energy $E < \Delta$ [i.e., still inside the localized parts of the DOS], conduction will occur by thermal excitation to the conductivity edges E_{c1} and E_{c2} of the extended states. The resistance $R(E)$ at this energy will then be given by

$$R(E) \propto e^{\frac{\Delta(E)+E}{k_B T}} + e^{\frac{\Delta(E)-E}{k_B T}} = \frac{1}{2} e^{\frac{\Delta(E)}{k_B T}} \cosh\left(\frac{E}{k_B T}\right) \tag{5.2}$$

For relatively small energies $E << k_B T$ the cosh-term can be approximated by a first-order Taylor expansion $\cosh\left(\frac{E}{k_B T}\right) \approx 1 + \frac{1}{2}\frac{E^2}{k_B^2 T^2} = \gamma(E)$. For small E we can interpret Eq. (5.2) as $R_{CNP} \propto \frac{1}{2} e^{\frac{\Delta(E)}{k_B T}} \gamma(E)$. At the CNP, $E = 0$, this approaches a trivial Ahrrenius-behavior, while for non-zero fixed energy $\gamma(E)$ is an energy-dependent renormalization factor which for $E << k_B T$ is independent of T.

We analyze the resistance at concentrations $n = \pm 3 \times 10^{14}$ m^{-2} [boxes marked in Fig. 5.2(a)] and multiply this data with a fixed constant to make an overlap with the low field data. All datapoints $R > 1$ MΩ in Fig. 5.2(c) are verified by this method and therefore reliable up to the highest field. This proper scaling for both low and high resistances also excludes a strong effect of the local heating due to the finite excitation voltage we apply over the sample; the power stays always in the order of picowatts.

From Fig. 5.2(c) we see that the scaling of the resistance at high magnetic fields is remarkably different from the linear field increase at low fields. This observation is visualized in Fig. 5.2(d) where we show that the calculated gap strongly bends and the slope strongly reduces. In this regime the gatesweeps are packed more densely for increasing magnetic field and the energy E gets comparable to the thermal activation $k_B T$ thus we are no longer able to calculate the gap size with a simple Arrhenius behaviour. Experimental limitations of our suspended

samples do not allow us to access much higher temperatures, therefore we can only speculate here about further gap-study.
At high enough fields we expect to fulfill the criteria of a fully spin-polarized system, $(n_\uparrow - n_\downarrow) \rightarrow 1$. The sudden strong change of the gap-size suggests that our system indeed gets fully spin-polarized, in literature also known as the cross-over to a quantum Hall ferromagnetic state.[21] Here both the magnetic field and the internal exchange causes the spins to align with the field fully. In literature an analogy is made with ferromagnetism, and therefore being a quantum Hall ferromagnetic state. Further increase of the magnetic field leads hypothetically to a dominating spin-splitting $g\mu_B B$, because $E_{ex} \propto \sqrt{B}$. Further specific research in titled magnetic fields is necessary to decouple the influence of the single electron Zeeman energy and exchange energy.

5.4 Magnetotransport properties at high carrier concentration

After detailed study at low concentrations we have a closer look at the manifestation of the QHE at higher concentration. In Fig. 5.3(a) we show the corrected two-point resistance as a function of V_G at 4.2 K for $B = 1$ T, 5 T, 12 T, 17.5 T and 30 T. Apart from the distinct $\nu = \pm 4$ plateaus which are already well pronounced at 1 T, additional plateaus at $\nu = \pm 3, \pm 2$, and ± 1 start to appear in higher fields. In Fig. 5.3(b) we show the derivative $\left|\frac{\mathrm{d}R}{\mathrm{d}V_G}\right|$ of the resistance curves, where we can already recognize distinct maxima and minima for lower fields.
In Fig. 5.3(c) we follow the position of the minima with increasing magnetic field. We see that the maximum applied gate-voltage $V_G = 60$ V (higher voltages causes an electrostatic force that bends the membrane and ultimately breaks) limits the observation of filling factors $\nu = \pm 4$ up to 9 T, while $\nu = \pm 2$ remains observable till fields of 15 - 20 T and filling factor $\nu = \pm 1$ is still observable at the highest applied field (30 T). From Fig. 5.3(c) we observe that the position of the minima strongly deviates from the linear relationship between the induced charge carrier concentration n and the applied magnetic field B, $n = \nu \frac{eB}{h}$. The equidistance of the minima for fixed magnetic fields excludes a capacitance-change due to the bending of the membrane; which can be expected by the particular big difference between the electric field induced bending (10 - 20 nm)[33] and the vacuum gap over which graphene is suspended (~ 1.5 μm). In Appendix B we discuss in more detail how to extract the exact relation between the applied field B and the induced charge carrier concentration n from this

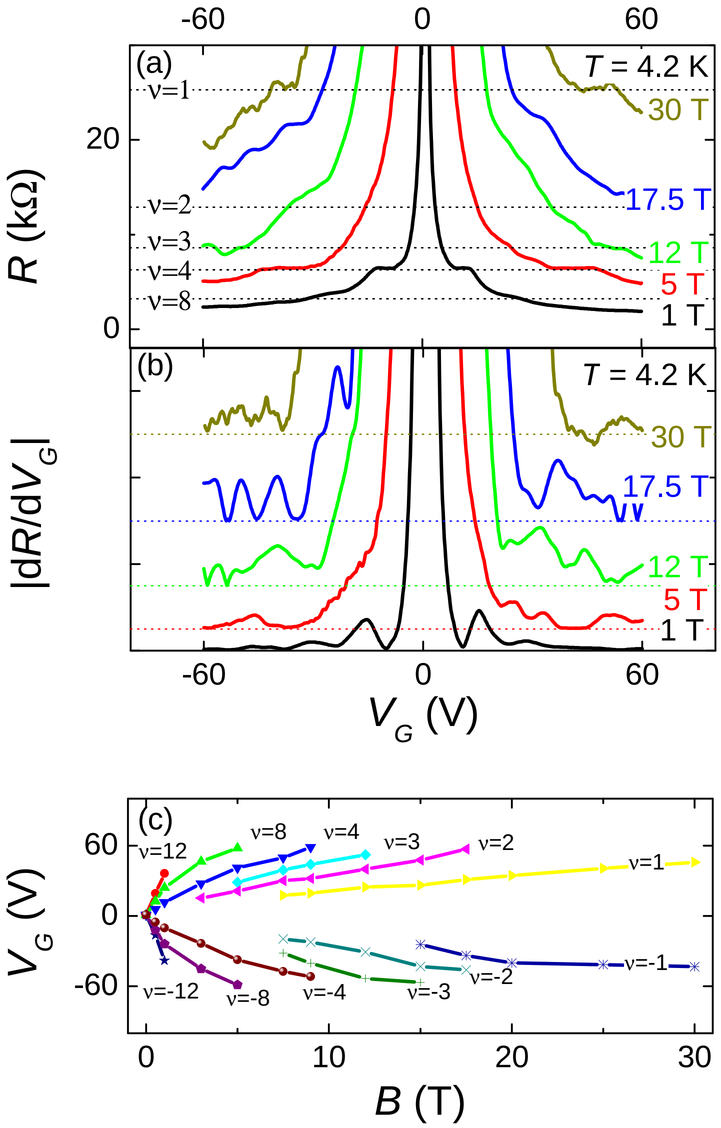

Figure 5.3: *(a) Gatesweeps $R(V_G)$ at constant magnetic fields $B = 1$ T, 5 T, 12 T, 17.5 T and 30 T for $T = 4.2$ K. (b) Derivative —dR/dV_G— for the curves in (a); the curves are shifted up for clarity. (c) Position of the minima for $\nu = \pm 12$, ± 8, ± 4, ± 3, ± 2 and ± 1 as a function of the magnetic field.*

data.

Experiments on suspended graphene-samples are mainly performed in two-probe configuration. Experimental limitations of the annealing-procedure do not allow us to obtain very homogenous samples in four-probe configuration. Therefore more effort has to be done to do a proper analysis on both the magnetoresistance and Hall-resistance. In Fig. 5.4 the appearance of the different filling factors are further elucidated; in particular at positive gate-voltages, the influence of contact-resistance is here experimentally the smallest. As shown in Fig. 5.3(b) the derivative of our data, $\left|\frac{\mathrm{d}R}{\mathrm{d}V_G}\right|$, shows already at very low field a very clear appearance of filling factors $\nu = 1$, 2, 3 and 4. A small change in the slope of R_{xy} causes a very distinct minimum in the derivative. Theoretically we can use a model that directly describes the magnetoresistance R_{xx} in terms of the Hall resistance R_{xy},[34] i.e. $R_{xx} \propto n\frac{\mathrm{d}R_{xy}}{\mathrm{d}n}$. In order to center all curves around the x-axis we remove a background in where clear oscillations are formed. In the inset of Fig. 5.4(a) we show the 12 T data (green) which is used to determine the background-line R_0 (black). In Fig. 5.4(a) we study the appearance of the filling factors by plotting the obtained magnetoresistances $R_{xx} - R_0$. We used the obtained leverage factor $\alpha(B)$ to determine the exact concentration n. Already at 3 T we observe the appearance of clear oscillations around $\nu = 2$ and $\nu = 3$ followed by the appearance of $\nu = 1$ at 5 T. The amplitude A of the oscillation is defined by the difference between the minimum and the first maximum. A single oscillation can be best analyzed by applying the Lifshitz-Kosevic equation[35] $A \cdot \cos(f(B))$, here A is the amplitude and $f(B)$ a field-dependent function that determines the frequency and phase. The Landau levels are broadened by temperature (e.g. activation gaps) and intrinsic scattering. The latter leads to an additional damping factor $\exp(\beta \cdot T_D m_c/B)$ with T_D the Dingle temperature, m_c the cyclotron mass in units of electron mass m_e, B the magnetic field, and $\beta = 14.694$ T/K. Here the Dingle temperature T_D acts as an effective temperature that describes the influence of different scattering mechanisms, e.g. different interaction scenarios. In Fig. 5.4(b) the amplitudes A for $\nu = 4$ and $\nu = 8$ are plotted as a function of $1/B$, which results in a linear decrease with slope $\beta \cdot T_D m_c$. If we assume the cyclotron mass in bilayer graphene to be $m_c \approx 0.033 \cdot m_e$ (corresponding to $\gamma_1 = 0.4$ eV, see Ref. 36 and references in there) we obtain the Dingle temperatures T_D in table 5.2. We repeat the same procedure for filling factors 1, 2 and 3 in Fig. 5.4(c).

Compared to $\nu = 4$, fully quantized at $B = 1$ T, the Dingle temperatures T_D for the degenerate filling factors are one order of magnitude larger, which means fields $B \geq 10$ T are required to observe full quantization; i.e. showing

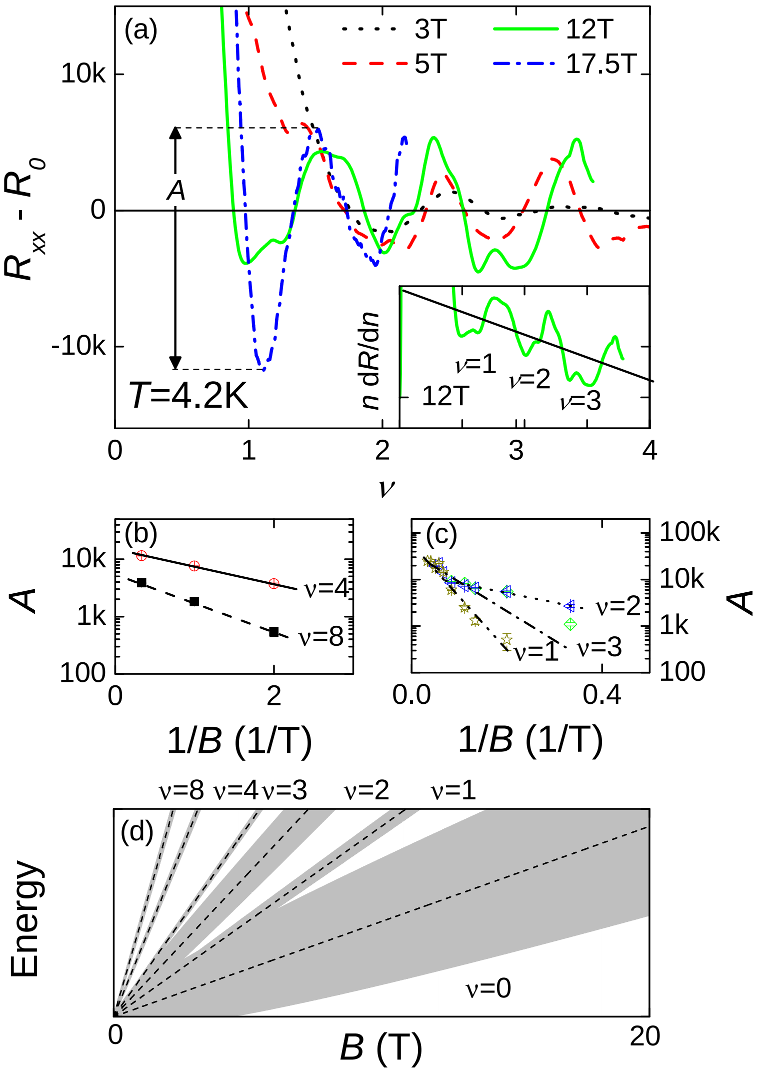

Figure 5.4: *(a) R_{xx}-oscillations after removing linear background from $n\frac{dR}{dn}$ for B = 3 T, 5 T, 12 T and 20 T at 4.2 K. (b) Dingle plot of $\nu = 8$ and $\nu = 4$: amplitude A of the oscillations as a function of the inverse field $1/B$. (c) Dingle plot for ν = 3, 2, and 1. (d) Schematic plot of the appearance of filling factors with increasing magnetic field. The dashed lines show the center of the Landau level, while the gray shaded area is the Landau level broadening determined by the Dingle temperature T_D.*

ν	8	4	3	2	1
T_D (K)	2.4 ± 0.4	1.4 ± 0.4	29.2 ± 4	9.2 ± 1.2	58 ± 8

Table 5.2: *Dingle temperatures T_D for filling factors $\nu = 8$, 4, 3, 2, and 1.*

quantized Hall resistance and a zero minimum in the magnetoresistance. In particular filling factor $\nu = 1$ shows a constant Hall resistance for fields of $B \gtrapprox 30$T [see Fig. 5.3(a), the Hall-resistance R_{xy} remains at a constant resistance-value of 25812 Ω in the range $V_G = 40...50$ V].

In Fig. 5.4(d) we illustrate qualitatively the appearance of the different Landau levels for increasing magnetic field. The corresponding gray shaded areas describe the Landau level broadening Γ, directly proportional to the Dingle temperature T_D; higher Dingle temperatures correspond to broader Landau levels. While the position of the energy moves linearly with increasing field, the Landau level broadening Γ is proportional to the square root of the applied field $\Gamma \propto \sqrt{B}$. With increasing field the overlap between the shaded areas decreases, and the plateau starts to appear. As we can see from Fig. 5.4(d) Landau levels around $\nu = 2$ and $\nu = 3$ do indeed not overlap anymore for similar magnetic field, however the shaded areas for $\nu = 1$ overlap until higher fields. Finally the overlapping of filling factors $\nu = \pm 1$ disappears at a similar magnetic field as the resistance at the CNP starts to bend strongly, supporting the idea of a cross-over to a fully spin-polarized state at $\nu = 0$.

After the appearance of the non-degenerated filling factors $\nu = 4$ and 8 a gap at $\nu = 0$ forms, followed by filling factors $\nu = 2$ and at high fields $\nu = 1$ and 3. This points to the different scattering mechanisms that belong to the formation of different quantized states. Moreover, this hierarchial sequence ($\nu = 4, 8, 12, ... \to \nu = 0 \to \nu = 2 \to \nu = 1, 3$) agrees with the proposed model of a spin exchange enhanced scenario at $\nu = 0$ (as sketched in the right side of Fig. 5.2(b)).

5.5 Conclusion

In conclusion we have performed experiments on a suspended BLG sample which shows us a field induced gap at the CNP for fields $B \geq 1$ T. The gap at $\nu = 0$ opens simultaneously with the formation of filling factors $\nu = \pm 4$, which implies the eight-fold degenerated lowest Landau breaks directly in two fourfold-degenerated spin-polarized subbands. At high magnetic fields we observe a smooth transition to a much smaller gap, this is consistent with the picture of the formation of a spin-polarized quantum Hall ferromagnetic state. Following the breaking of the lowest Landau level we observe a breaking of $\nu = 0$ in $\nu = \pm 2$ and finally in $\nu = \pm 1$ and $\nu = \pm 3$, in agreement with the theoretically proposed model of a quantum Hall ferromagnet.

References

[1] A. K. Geim and K. S. Novoselov, “The rise of graphene”, *Nature Materials* **6**, 183–191 (2007).

[2] K. I. Bolotin, K. J. Sikes, Z. Jiang, M. Klima, G. Fudenberg, J. Hone, P. Kim, and H. L. Stormer, “Ultrahigh electron mobility in suspended graphene”, *Solid State Communications* **146**, 351–355 (2008).

[3] X. Du, I. Skachko, and E. Y. Andrei, “Towards Ballistic Transport in Graphene”, *International Journal of Modern Physics B* **22**, 4579–4588 (2008).

[4] C. R. Dean, A. F. Young, I. Meric, C. Lee, L. Wang, S. Sorgenfrei, K. Watanabe, T. Taniguchi, P. Kim, K. L. Shepard, and J. Hone, “Boron nitride substrates for high-quality graphene electronics”, *Nature Nanotechnology* **5**, 722–726 (2010).

[5] C. R. Dean, A. F. Young, P. Cadden-Zimansky, L. Wang, H. Ren, K. Watanabe, T. Taniguchi, P. Kim, J. Hone, and K. L. Shepard, “Multicomponent fractional quantum Hall effect in graphene”, *Nature Physics* **7**, 693696 (2011).

[6] K. I. Bolotin, F. Ghahari, M. D. Shulman, H. L. Stormer, and P. Kim, “Observation of the fractional quantum Hall effect in graphene”, *Nature* **475**, 196–199 (2011).

[7] X. Du, I. Skachko, F. Duerr, A. Luican, and E. Y. Andrei, “Fractional quantum Hall effect and insulating phase of Dirac electrons in graphene”, *Nature* **462**, 192–195 (2009).

[8] B. E. Feldman, J. Martin, and A. Yacoby, “Broken-symmetry states and divergent resistance in suspended bilayer graphene”, *Nature Physics* **5**, 889–893 (2009).

[9] N. Tombros, A. Veligura, J. Junesch, M. H. D. Guimaraes, I. J. Vera-Marun, H. T. Jonkman, and B. J. van Wees, “Quantized conductance of a suspended graphene nanoconstriction”, *Nature Physics* **7**, 697–700 (2011).

[10] K. S. Novoselov, E. McCann, S. V. Morozov, V. I. Fal’ko, M. I. Katsnelson, U. Zeitler, D. Jiang, F. Schedin, and A. K. Geim, “Unconventional quantum Hall effect and Berry’s phase of 2π in bilayer graphene”, *Nature Physics* **2**, 177–180 (2006).

[11] Y. Zhao, P. Cadden-Zimansky, Z. Jiang, and P. Kim, “Symmetry Breaking in the Zero-Energy Landau Level in Bilayer Graphene”, *Physical Review Letters* **104**, 066801 (2010).

[12] R. Nandkishore and L. Levitov, “Dynamical Screening and Excitonic Instability in Bilayer Graphene”, *Physical Review Letters* **104**, 156803 (2010).

[13] R. Nandkishore and L. Levitov, “Electron interactions in bilayer graphene: Marginal Fermi liquid and zero-bias anomaly”, *Physical Review B* **82**, 115431 (2010).

[14] F. Zhang, J. Jung, G. A. Fiete, Q. Niu, and A. H. MacDonald, “Spontaneous Quantum Hall States in Chirally Stacked Few-Layer Graphene Systems”, *Physical Review Letters* **106**, 156801 (2011).

[15] J. Jung, F. Zhang, and A. H. MacDonald, “Lattice theory of pseudospin ferromagnetism in bilayer graphene: Competing interaction-induced quantum Hall states”, *Physical Review B* **83**, 115408 (2011).

[16] J. Martin, B. E. Feldman, R. T. Weitz, M. T. Allen, and A. Yacoby, “Local Compressibility Measurements of Correlated States in Suspended Bilayer Graphene”, *Physical Review Letters* **105**, 256806 (2010).

[17] J. Velasco, L. Jing, W. Bao, Y. Lee, P. Kratz, V. Aji, M. Bockrath, C. N. Lau, C. Varma, R. Stillwell, D. Smirnov, F. Zhang, J. Jung, and A. H. MacDonald, “Transport spectroscopy of symmetry-broken insulating states in bilayer graphene”, *Nature Nanotechnology* **7**, 156–160 (2012).

[18] R. T. Weitz, M. T. Allen, B. E. Feldman, J. Martin, and A. Yacoby, “Broken-Symmetry States in Doubly Gated Suspended Bilayer Graphene”, *Science* **330**, 812–816 (2010).

[19] S. Kim, K. Lee, and E. Tutuc, “Spin-Polarized to Valley-Polarized Transition in Graphene Bilayers at $\nu = 0$ in High Magnetic Fields”, *Physical Review Letters* **107**, 016803 (2011).

[20] F. Freitag, J. Trbovic, M. Weiss, and C. Schonenberger, “Spontaneously Gapped Ground State in Suspended Bilayer Graphene”, *Physical Review Letters* **108**, 076602 (2012).

[21] Y. Barlas, R. Cote, K. Nomura, and A. H. MacDonald, “Intra-Landau-level cyclotron resonance in bilayer graphene”, *Physical Review Letters* **101**, 097601 (2008).

[22] N. Tombros, A. Veligura, J. Junesch, J. J. van den Berg, P. J. Zomer, M. Wojtaszek, I. J. V. Marun, H. T. Jonkman, and B. J. van Wees, “Large yield production of high mobility freely suspended graphene electronic devices on a polydimethylglutarimide based organic polymer”, *Journal of Applied Physics* **109**, 093702 (2011).

[23] K. S. Novoselov, A. K. Geim, S. V. Morozov, D. Jiang, Y. Zhang, S. V. Dubonos, I. V. Grigorieva, and A. A. Firsov, “Electric field effect in atomically thin carbon films”, *Science* **306**, 666–669 (2004).

[24] P. Blake, E. W. Hill, A. H. C. Neto, K. S. Novoselov, D. Jiang, R. Yang, T. J. Booth, and A. K. Geim, “Making graphene visible”, *Applied Physics Letters* **91**, 063124 (2007).

[25] I. J. Vera-Marun, P. J. Zomer, A. Veligura, M. H. D. Guimaraes, L. Visser, N. Tombros, H. J. van Elferen, U. Zeitler, and B. J. van Wees, “Quantum Hall transport as a probe of capacitance profile at graphene edges”, *arXiv:1112.5462v1* (2011).

[26] J. Moser, A. Barreiro, and A. Bachtold, “Current-induced cleaning of graphene”, *Applied Physics Letters* **91**, 163513 (2007).

[27] D. A. Abanin and L. S. Levitov, “Conformal invariance and shape-dependent conductance of graphene samples”, *Physical Review B* **78**, 035416 (2008).

[28] B. Huard, N. Stander, J. A. Sulpizio, and D. Goldhaber-Gordon, “Evidence of the role of contacts on the observed electron-hole asymmetry in graphene”, *Physical Review B* **78**, 121402 (2008).

[29] P. Blake, R. Yang, S. V. Morozov, F. Schedin, L. A. Ponomarenko, A. A. Zhukov, R. R. Nair, I. V. Grigorieva, K. S. Novoselov, and A. K. Geim, “Influence of metal contacts and charge inhomogeneity on transport properties of graphene near the neutrality point”, *Solid State Communications* **149**, 1068–1071 (2009).

[30] E. McCann, “Asymmetry gap in the electronic band structure of bilayer graphene”, *Physical Review B* **74**, 161403 (2006).

[31] M. Kharitonov, “Canted antiferromagnetic phase of the $\nu = 0$ quantum Hall state in bilayer graphene”,

[32] E. V. Kurganova, H. J. van Elferen, A. McCollam, L. A. Ponomarenko, K. S. Novoselov, A. Veligura, B. J. van Wees, J. C. Maan, and U. Zeitler,

"Spin splitting in graphene studied by means of tilted magnetic-field experiments", *Physical Review B* **84**, 121407 (2011).

[33] Z. Wang, L. Philippe, and J. Elias, "Deflection of suspended graphene by a transverse electric field", *Physical Review B* **81**, 155405 (2010).

[34] H. L. Stormer, K. W. Baldwin, L. N. Pfeiffer, and K. W. West, "Strikingly linear magnetic field dependence of the magnetoresistivity in high quality two-dimensional electron systems", *Solid State Communications* **84**, 95–98 (1992).

[35] I. M. Lifshitz and A. M. Kosevich, "Theory of Magnetic Susceptibility in Metals at Low Temperatures", *Soviet Physics Jetp-Ussr* **2**, 636–645 (1956).

[36] E. V. Kurganova, A. J. M. Giesbers, R. V. Gorbachev, A. K. Geim, K. S. Novoselov, J. C. Maan, and U. Zeitler, "Quantum Hall activation gaps in bilayer graphene", *Solid State Communications* **150**, 2209–2211 (2010).

Chapter 6

Transport gap in suspended bilayer graphene at zero magnetic field

Abstract

We report a change of three orders of magnitude in the resistance of a suspended bilayer graphene flake which varies from a few kΩs in the high-carrier-density regime to several MΩs around the charge neutrality point (CNP). The corresponding transport gap is 8 meV at 0.3 K. The sequence of quantum Hall plateaus appearing at filling factor $\nu = 2$ followed by $\nu = 1$ suggests that the observed gap is caused by the symmetry breaking of the lowest Landau level. Investigation of the gap in a tilted magnetic field indicates that the resistance at the CNP shows a weak linear decrease for increasing total magnetic field. Those observations are in agreement with a spontaneous valley splitting at zero magnetic field followed by splitting of the spins originating from different valleys with increasing magnetic field. Both, the transport gap and magnetic field response point toward a spin polarized layer anti-ferromagnetic state as the ground state in the bilayer graphene sample. The observed non-trivial dependence of the gap value on the normal component of the magnetic field suggests possible exchange mechanisms in the system.

Part of this work has been published in: A. Veligura, H.J. van Elferen, et al., *Transport gap in suspended bilayer graphene at zero magnetic field*, Physical Review B **85**, 155412 (2012)

6.1 Introduction

Followed by the isolation of single layer graphene, the study of bilayer graphene (BLG) became a separate direction of research in the study of two-dimensional materials. Charge carriers in bilayer graphene have a parabolic dispersion with an effective mass of about 0.033 m_e,[1] but also possess a chirality. The latter manifests itself in an unconventional quantum Hall effect[2] with the lowest Landau level (LLL) being eight fold degenerate. Compared to single layer graphene, bilayer graphene has, in addition to spin and valley degrees of freedom, an additional orbital degree of freedom, where Landau levels with numbers $N = 0$ and 1 (each four fold degenerate) have the same energy.[2,3] Recent advances in obtaining suspended bilayer graphene devices with charge carrier mobility exceeding $\mu > 1$ m^{2}V^{-1}s^{-1} gave access to the investigation of many-body phenomena in clean bilayer graphene at low charge carrier concentration ($n < 10^{14}$ m^{-2}).[4–11] Due to the non vanishing density of states at the charge neutrality point (CNP), bilayer graphene is predicted to have a variety of ground states triggered by electron-electron interaction. There are two competing theories describing the ground state of BLG: a transition (i) to a gapped layer polarized state (excitonic instability)[12–17] or (ii) to a gapless nematic phase.[18–20]

External influence (e.g. electric field or dopants on the surface) causes a layer polarization. This causes the charge carriers to favorably occupy the top or bottom layer, called excitonic instability. This excitionic instability is a layer polarization in which the charge density contribution from each valley and spin spontaneously shifts to one of the two graphene layers[16,17] caused by an arbitrarily weak interaction between charge from the conduction and valence band states.[12,13] Since each bilayer flavor (spin or valley) can polarize toward either of the two layers, there are 16 possible states.[16,17] In Fig. 6.1 we show 8 of these different states, in where the other 8 are obtained by layer reversal. These states are classified by the total polarization as being *layer* ferromagnetic FM (all degrees of freedom choose the same layer), *layer* ferrimagnetic FiM (three of the four valley-spin flavors choose the same layer), or *layer* antiferromagnetic AFM (with no overall polarization). In Fig. 6.1 we demonstrate that the variety of occupation of the two layers and in addition the two-fold spin ($\uparrow$ and $\downarrow$) and two-fold valley ($+$ and $-$) results in 2 FM-states, 8 FiM-states, and 6 AFM-states. These states are considered as analogous to the biased bilayer[21] in the sense that the charge transfer can be attributed to the (wave-vector-dependent) exchange potential difference between low-energy sites on the opposite layers.[16] The total energy of the system is lowered by the gain in the exchange interaction via breaking of the inversion symmetry, i.e. introducing a gapped state. In chapter

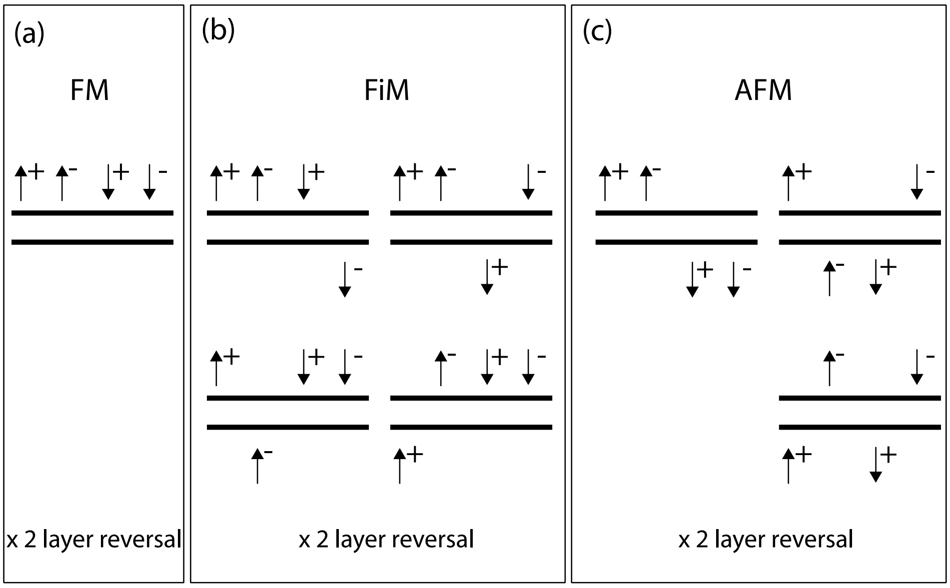

Figure 6.1: *Different groundstates for bilayer graphene samples. Here we demonstrate 8 of the 16 different states, the other 8 states are obtained by layer reversal. Different spin orientation is given by* $\uparrow$ *and* $\downarrow$*, while different valleys are given by* $+$ *and* $-$*.(a) Layer ferromagnetic state (FM), all charge carriers choose the same layer. (b) Layer ferrimagnetic state (FiM), 3 of the 4 charge carriers choose the same layer. (c) Layer antiferromagnetic state (AFM), two charge carriers in the upper layer and two charge carriers in the bottom layer. Experimental evidence is found for the first AFM-state, the layer antiferromagnet (LAF), and third state, the anomalous quantum Hall (AQH).*

5 we have discussed a ferromagnetic (FM) scenario in where all spins occupy one layer. Recent experiments have shown a big variety of results,[5–7] being prove of the evidence of the different ground states as discussed above. Theoretically the antiferromagnetic polarization is electrostatically favorable due to the absence of a net charge on both layers; however, the actual ground state is theoretically undefined.[12,16,22] However with changing number of impurities and/or external electric field one might expect different ground states. More specifically recent experiments have suggested evidence of the possible existence of two of the antiferromagnetic states — the anomalous quantum Hall (AQH) state[5,6] and the spin-polarized layer-antiferromagnetic (LAF) state.[7] To avoid possible confusion we note that in earlier literature[16] the LAF state is also called the quantum valley Hall state. The AQH state (third AFM-state in Fig. 6.1(c))

has electrons that are polarized in the same layer for both spins and in opposite layers for opposite valleys.[16, 22] The broken valley-degeneracy for zero field leads in this case to a spontaneously broken time-reversal symmetry and therefore possess a substantial orbital magnetization. This intrinsic magnetization leads to exhibiting of the quantized Hall effect at zero magnetic field.[22] Due to its magnetization the AQH state can be favored over other ground states in a perpendicular magnetic field. The LAF state has opposite spin polarization for opposite layers (first AFM-state in Fig. 6.1(c)). In contrast to the AQH state, the LAF state does not have topologically protected edge states (no counter-propagating charge carriers of opposite spins in the same layer), which brings its minimum conductance to zero. For both states the theoretical estimations of the gap Δ give the value of 1.5-30 meV.[13, 16] However, the inter-valley exchange weakly favors the LAF state.[16, 23] One of the ways to determine the character of the bilayer ground state experimentally is to investigate the response of the gap value to a magnetic field B (which couples to spin) and electrical field E (which couples to the valley degeneracy).[23] When Zeeman coupling is included, the AQH-state quasiparticles simply spin split, leaving the ground state unchanged but the charge gap reduced. It was calculated that for a 4 meV spontaneous gap at zero field, a field of $B = 35$ T drives the gap to zero. On the other hand, the gap in the LAF state is weakly B field dependent.

The second possible description for the ground state of BLG is based on a nematic phase caused by the renormalization of the low-energy spectrum.[18, 19] Detailed tight-binding model studies showed that inclusion of next-neighbor interlayer coupling changes the band structure in the bilayer, producing a Lifshitz transition in which the isoenergetic line about each valley is broken into four pockets with linear dispersion.[3, 24] At energies higher then 1 meV the four pockets merge into one pocket with the usual quadratic dispersion. Moreover, electron-electron interactions might result in further energy spectrum transformation, where the number of low energy cones can be reduced to 2 near each of the two K points.[18, 19] In this case the minimum conductance of the bilayer graphene is supposed to be increased comparing to a bilayer with parabolic dispersion ($8e^2/h$). This scenario was also supported by the experimental results on suspended bilayer graphene in which strong spectrum reconstructions and electron topological transitions were observed.[10]

In this chapter we present electric transport properties of suspended bilayer graphene determined by studying its behavior in tilted magnetic fields. At $B = 0$ T we observe the spontaneous opening of a gap by changing charge carrier density from the metallic regime ($n = \pm 3.5 \times 10^{15}$ m^{-2}) to the CNP. At a temperature of 1.3 K we measure a resistance increase from 5 kΩ up to 14 MΩ. The observation indicates a gapped ground state of the studied bilayer graphene with a gap value of 6.8 meV. Measurements in a tilted magnetic field showed that the resistance at the CNP decreases with an increase of the magnetic field. Based on this we propose a possible scenario of symmetry breaking in this bilayer graphene sample: spontaneous valley splitting at zero magnetic field followed by the splitting of the spins originating from different valleys with increase of the magnetic field. Both the gap value and its weak linear decrease with B supports the LAF state as the ground state of the studied sample.

6.2 Experimental details

A suspended bilayer graphene device was prepared using an acid free technique.[25, 26] We deposited highly ordered pyrolytic graphite on an n^{++}Si/SiO$_2$ wafer (500 nm thick) which is covered with an organic resist LOR (1.15 μm). A standard lithography procedure is performed in order to contact bilayer graphene flakes (determined by their contrast in an optical microscope) with 80 nm of Ti/Au contacts. A second electron beam lithography step is used to expose trenches over which the graphene membrane becomes suspended [see Ref. 26 and section 3.6]. To achieve high-quality devices we use the current annealing technique by sending a dc current through the membrane (up to 1.1 mA) at a temperature of 4.2 K. While ramping up the dc current, simultaneously we keep track of the sample resistance. Once the resistance reaches values on the order of 10 kΩs we stop annealing and check the gate voltage dependence. We repeat this procedure until the appearance of a sharp resistance maximum at the CNP located close to zero V_G [More details on the current annealing procedure can be found section 3.6 and Ref. 26]. The studied device was 2 μm long and 2.3 μm wide. All measurements were performed in four-probe geometry with contacts across the full width of graphene at the temperatures from 4.2 K down to 300 mK. The four-probe method allows the elimination of contact resistances. As discussed below the resistance measurements consist of a superposition of the longitudinal magnetoresistance ρ_{xx} and Hall-resistance ρ_{xy}. The carrier density n in graphene is varied by applying a dc voltage V_G between the back gate electrode n^{++} Si and the graphene flake. Based on the serial-capacitor model, the unit capacitance of the system is 7.2 aFμm^{-2}, which relates the gate voltage with the density as $n = \alpha V_G$, where α is the leverage factor of $\alpha = 0.5 \times 10^{14}$ m^{-2}V^{-1}. The resistive measurements are done by applying a 45 mV excitation voltage over an in series connected 45 MΩ pre-resistor, creating an excitation current of 1 nA. For the maximum resistance values (1-10 MΩ) this creates a power dissipation $P = I^2R \approx$ 1-10 pW, which is low enough to avoid self-heating of the sample.

6.3 Temperature dependence and quantum transport

Our pristine samples are strongly p-doped with the CNP situated beyond 60 V and a metallic resistance of a few hundreds of ohms over the entire voltage range. Therefore we perform the current annealing technique in order to obtain high-quality devices. In contrast to previous samples, in which each successive step of current annealing tended to cause a sharper change in the resistance values within the scanned region of V_G, the bilayer sample discussed here already shows after the first current annealing step a highly resistive region around the CNP (not shown). The next annealing step (1.1 mA) moves the charge neutrality point down to $V_G = 3$ V. However, surprisingly the resistance around the CNP becomes 11 MΩ and is reduced down to 5 kΩ in the metallic regime at V_G = -60 V [Fig. 6.2(a), inset]. This fact points toward the opening of a gap. The temperature dependence of the resistance of the membrane from 4.2 K to 300 mK is shown in Fig. 6.2(c). There is an essential change of about 6 MΩ in the maximum resistance R_{max} from 4.2 down to 1.3 K; however, further lowering of the temperature does not change R_{max} much. From an Arrhenius plot of the resistance at the CNP [Fig. 6.2(c)] we can extract a thermal excitation gap of 0.33 meV.[27] The flattening of the resistance at lower T can be explained by variable-range hopping with different temperature dependence.[28] We would like to point out that our excitation current value of 1 nA gave a voltage drop proportional to 10 mV at the CNP, which is much higher than the energy k_BT at measured temperatures (0.3 meV). Here we can not use a simple Ahrrenius-activation model to quantify the behavior of the resistance at the CNP, but can only qualitatively estimate the resistive response on an applied magnetic field. There might be several scenarios for the observed gap formation in the gate voltage dependence: (i) A lateral confinement in the membrane, where the energy levels are

$$E_n = \frac{\hbar^2 k^2}{2m} = \frac{\hbar^2 \pi^2}{2mW^2} l^2 \tag{6.1}$$

$W = 2.3$ μm is the width of the flake and l is an integer value. However, the first two levels have energies of $E_1 = 1.3$ μeV and $E_2 = 5.3$ μeV, which are much lower than k_BT at measured temperatures. (ii) True gap formation with zero density of states within the gap and available states at the conduction and valence bands. (iii) A transport gap, accompanied by the observation of the

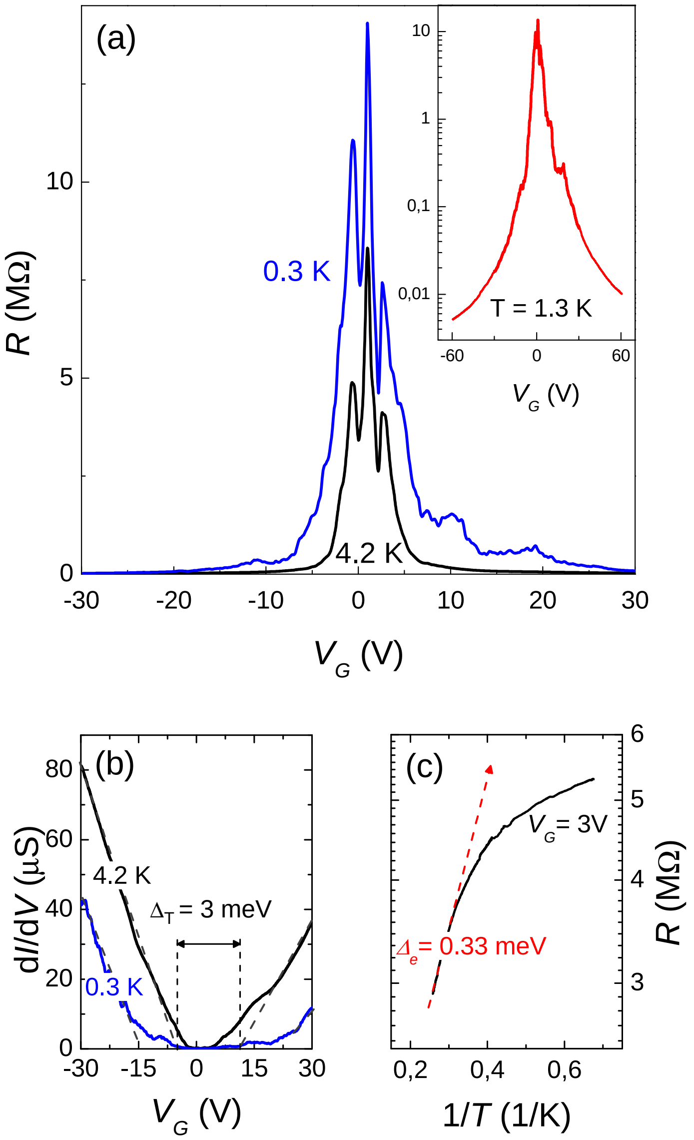

Figure 6.2: *Four-probe resistance of the suspended bilayer graphene. (a) Gate dependence of the sample at the temperatures of 4.2 K and 0.3 K. Inset: Resistance at 1.3 K on a logarithmic scale showing the dramatic change from the CNP to the metallic regime. (b) Transport gap extraction at 4.2 and 0.3 K. The energy gap in the bias direction is highlighted by the conductance crossover (fitted with dashed lines) at zero. The values of the transport gaps are 3 meV (4.2 K) and 8 meV (0.3 K). (c) An Arrhenius plot of the resistance with an extracted thermal gap of 0.33 meV.*

reproducible conductance oscillations in the region of suppressed conductance. In such a regime transport is limited by the quantum confinement effect along the width (mainly originating from the impurities).[29] (iv) A more complicated case, when the gap value depends on the charge carrier density, i.e. the energy of the levels changes while they are being filled with carriers. This situation might happen when the gap is induced by charge redistribution in between layers, which would be influenced by the applied back gate voltage. At the moment, we can not determine the exact gap type; therefore, further analysis is performed assuming a transport gap scenario, but keeping in mind that this gap value can depend on the density.

In analogy to graphene nanoribbon studies,[29,30] we extract the transport gap from the gate dependence of the sample conductance as shown in Fig. 6.2(b). From a linear approximation of conductance one gets a region of ΔV_G where the sample shows insulating behavior. This region ΔV_G over which the sample is insulating can be expressed in a Fermi wavenumber k_F. The Fermi wavenumber k_F depends on the charge carrier concentration n, as $n = k_F^2/\pi$. As explained before the charge carrier concentration depends linearly on the applied backgate-voltage, $n = \alpha V_G$. Therefore we can express the region ΔV_G in a dependence of the wavenumber $\Delta k_F = \sqrt{\pi \Delta n} = \sqrt{\pi \alpha \Delta V_G}$.

$$\Delta E_F = \frac{\hbar^2 \Delta k_F^2}{2m} = \frac{\hbar^2}{2m} \pi \alpha \Delta V_G \tag{6.2}$$

From conductance graphs at different T we find $\Delta E_F = 3$ meV at 4.2 K and $\Delta E_F = 8$ meV at 0.3 K. The values of the transport gap are comparable to the energy gap (extracted in the bias direction) values of single-layer graphene nanoribbons of 50-85 nm wide,[29,30] where in contrast to our case the gap is created by lateral confinement. The resistance value of 5 kΩ in the metallic regime, similar to that of regular graphene devices, serves as an additional justification for excluding lateral confinement as a cause of the observed transport gap. We can calculate the mobility of the charge carriers using the standard formula $\mu = 1/(eR_{sq}n)$, where R_{sq} is the square resistance of the sample and e is the elementary charge. The mobility value $\mu \propto\ 2$ m^{2}V^{-1}s^{-1} at $n = 3.5 \times 10^{15}$ m^{-2} corresponds to the value of high quality bilayer graphene devices. Due to the symmetry of resistance change around the CNP [Fig. 6.2(b)] and the fact that the CNP itself is situated around zero gate voltage ($V_G = 1.2$ V), that corresponds to the density of $n = 0.77 \times 10^{14}$ m^{-2} at 0 V, we can also exclude the low quality "p-doped" regions close to the contacts (which can form after current annealing) as the cause of the reported gap. In the meantime, we can not exclude a charge inhomogeneity in the sample bulk which might lead to the observed order of magnitude difference between electrical and transport gaps, in analogy to the nanoribbon case.

Given the fact that the resistance values reach MΩ values at the CNP, it is already hard to establish quantum Hall plateaus in our suspended bilayer device. However, we have achieved the observation of quantum Hall transport shown in Figs. 6.3(a) and 6.3(b). The first quantum Hall plateau appear at 5 T on the electron side (solid curve), which we attribute to the filling factor $\nu = 2$. This plateau is followed by the appearance of $\nu = 1$ at 7 T [Fig. 6.3(b)]. The conductance values of the observed plateaus deviate from the expected ones of $2e^2/h$ and $1e^2/h$, since they are affected by charge inhomogeneity. Therefore, we determine the exact values of the corresponding plateaus by the scaling of their positions in the graph of density ($V_{G\nu}$) vs magnetic field B [Fig. 6.3(d)]. As expected from $\nu = n/(eB/h)$ the scaling is linear with the leverage factor of $\alpha = 0.55 \times 10^{14}$ m^{-2} V^{-1} for $\nu = 2$ and 1. In order to use the same α for both filling factor sets [see Fig. 6.3(d)] the slopes of $V_{G\nu}$ versus B; and ν values respectively, have to be a factor 2 different. Therefore, we have to point out that the linear scaling will hold as well for a leverage factor of 1.1×10^{14} m^{-2} V^{-1} if we assume $\nu = 4$ and 2 as the observed sequence of plateaus. From previous studies[31] we know that the capacitance probed by the quantum Hall effect (QHE) in graphene devices (especially in suspended samples) can be higher than the geometrical value, due to the deviation from the plane capacitor model. However, we attribute the observed plateaus to the filling factors 2 and 1. As we noticed before,[8, 25] most of the time the current annealing procedure leads to the formation of high-quality annealed regions connected in series with low mobility *p*-doped regions close to the contacts. Therefore higher values of the conductance plateaus can be explained by a *p*-doped slope, which increases with magnetic field B. This might also be the reason for the absence of the resistance quantization on the electron side [Fig. 6.3(c)]. Assuming $\mu B \gg 1$ for the formation of QHE plateaus,[32] our observation implies a lower bound for the mobility of 0.2 m^2 V^{-1} s^{-1}.

To summarize our QH transport results: At this point we have shown that a zero-field gap opens at the CNP in the studied graphene bilayer. This observation points to a possible symmetry breaking of the ground state in bilayer graphene. The application of B does not restore the broken symmetry and brings the systems into the QH-regime. In Fig. 6.3(e) we show the hierarchy of the splitting of the eightfold degenerate lowest Landau level in applied B.[33] The development of the level structure with B will be specified and discussed in section 6.4. Meanwhile, if we assume that at $B = 0$ T one of the degeneracies is already lifted, then, with increasing field, one can expect quantization at the filling factors $\nu = 0$ and 4 followed by $\nu = 2$ and 1. However, if the initial symmetry breaking is strong enough and the scanned window in energy is lim-

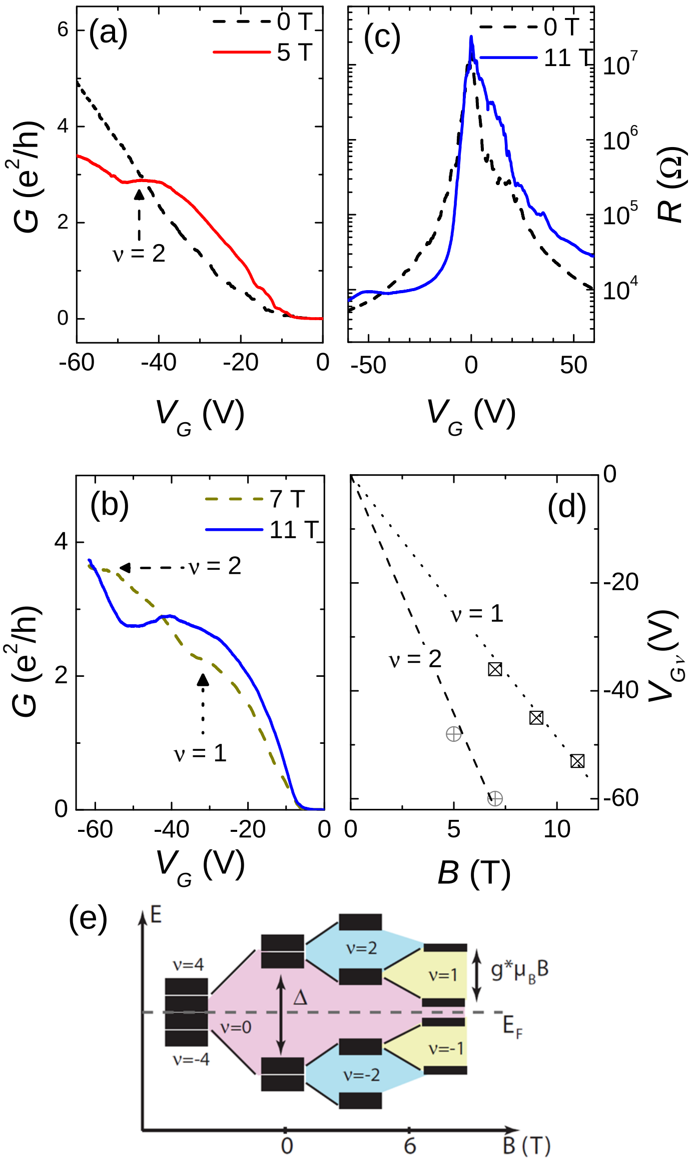

Figure 6.3: *Quantum transport at 1.3 K. (a) Quantum Hall conductance of the suspended bilayer at $B = 0$ and 5 T. (b) Quantum Hall conductance of the suspended bilayer at $B = 7$ and 11 T. The exact filling factors ν corresponding to the observed plateaus are shown. (c) Resistance of the sample in the quantum Hall regime. (d) Scaling of the filling factor positions in graph of gate voltage ($V_{G\nu}$) vs magnetic field. (e) LL hierarchy of the symmetry breaking of the lowest LL in bilayer graphene. Suggested scenario of spontaneous valley splitting followed by spin splitting at high B.*

ited (V_G), then one can expect quantization at $\nu = 2$ followed by $\nu = 1$. This described hierarchy of levels splitting and sequence of plateaus will be observed independent or either valley or spin splitting occurs first.

6.4 Resistance at the CNP in tilted magnetic field

In order to clarify the nature of the gapped ground state of bilayer graphene and its evolution in a magnetic field we perform a tilted-magnetic-field experiment. In tilted experiments the total magnetic field B_{tot} can be separated from the perpendicular field: $B_n = B_{tot}\cos(\phi)$, where ϕ is the angle between these two vectors [Fig. 6.4(c)]. This procedure allows us to distinguish between the orbital effect and bare Zeeman energy, which has to scale with the B_{tot}-value.[1,23,33]

All measurements presented below were performed at a temperature of 1.3 K. The application of the magnetic field perpendicular to the sample plane leads to an increase in the resistance at the CNP, as expected for QH transport in the case of broken-symmetry states. To distinguish between the normal (perpendicular) field B_n and total field B_{tot} we perform a series of experiments keeping B_n fixed and gradually increasing B_{tot}. As an example, in Fig. 6.4(a) we show a change in R_{max} at $B_n = 5$ T with B_{tot} increasing from 6 to 30 T for different angles ϕ. The actual maximum of the resistance consists of three peaks: highly resistive in the middle ($V_G = 1.2$ V) and two side peaks at the gate voltages at -0.5 and 3 V. The total magnetic field causes a decrease in the resistance and the middle peak starts splitting into two peaks (or developing a minimum in resistance at the CNP) when $B_{tot} > 6$ T for studied values of B_n. We observe exactly the same behavior in the experiment when $B_n = 0$ and the applied field is parallel to the graphene membrane: the maximum of the resistance goes down and develops a local minimum at the CNP [Fig. 6.4(b)]. We attribute this change to an increase of the total magnetic field. The fact that the resistance changes with B_{tot} indicates that the observed effect is not a simple quantum localization due to inhomogeneity in the sample.

All three maxima around the CNP decrease in their resistance in a parallel applied B. However, only the middle maximum at $V_G = 1.2$ V shows clear scaling with the total magnetic field B_{tot} at different tilted angles ϕ [Fig. 6.5(a)]. As one can see in the case of $B_{tot} = B_n$ [$\phi = 0$, black curve in Fig. 6.5(a)] the resistance keeps on increasing up to around 14 T; further increase in the magnetic field brings R_{max} to lower values [Fig. 6.5(a)]. Once the non zero angle is introduced the common trend for R_{max} is a decrease.

We suggest that the behavior of the middle peak is caused by a many-body effect and can be explained by the Zeeman splitting closing the spontaneous gap. The hierarchy of energy levels is depicted in Fig. 6.3(e). Once B is large enough the LLL is split into four levels, each two-fold degenerate. If we assume that the latter degeneracy is that of spin, then after the appearance of the plateau associated with filling factor $\nu = 1$ we expect the value of the ground-state gap Δ to be lowered by spin splitting coupled to B_{tot}. Here we would like to emphasize that we do observe the appearance of $\nu = 1$ and a minimum of resistance at the CNP in a similar magnetic field $B_{tot} > 7$ T. In a simplified way we describe the resistance value at the CNP point as

$$\ln\left(R_{max}\right) \propto \frac{\Delta}{kT} - \frac{g^{*}\mu_B B_{tot}}{kT} \tag{6.3}$$

where g^{*} is an effective g-factor including exchange electron interaction and a Landau level broadening.[1,8,34] The change in $\ln(R)$ versus B_{tot} at fixed B_n values is shown in Fig. 6.5(b). This dependence can be best described as linear. The slope and y intercept of the linear fit of Fig. 6.5(b) give the values of Δ and $g^{*}\mu_B$. Surprisingly, both these contributions scale with the B_n component. In Fig. 6.5(c) we show $g^{*}\mu_B$ values versus B_n. Despite the fact that the scaling appears linear, a plot of the slope as a function of $\sqrt{B_n}$ does seem to fit also (not shown), which is an indication for an interaction driven mechanism [see table 5.1, chapter 5]. Δ increases with B_n from 1.4 meV at $B_n = 1$ T up to 1.7 meV at $B_n = 25$ T (not shown). This Δ is of the same order as the measured transport gap (which can overestimate a real energy gap) and is in the order of the theoretically predicted gap of 1.5-30 meV for the excitonic instability.[13,16,23]

In summary, tilted-magnetic-field experiments show that the resistance at the CNP of the studied gapped bilayer graphene decreases linearly with increase of the total magnetic field component. This points to a many-body effect and weak reduction of the gap in an applied magnetic field. The developed minimum in the resistivity in Fig. 6.4 can be explained by the overlapping of spin-up and spin-down levels from the adjacent Landau levels due to Zeeman splitting in the applied B.[34] The fact that we stay here in the temperature-independent regime (no activated transport) makes it difficult to estimate an effective g^{*}-factor, the estimated value 0.2 is far too low for a spin splitting scenario. Therefore we can only speculate about the explanation for the experimental observations. In addition, although the resistance decreases in a parallel field, the R_{max} value does not change by an order of magnitude. This behavior in B is consistent with the layer-antiferromagnetic being the ground state of the studied bilayer sample.[23] Since in this state the top and bottom layers host spins with opposite orientations, their interaction with the applied B can not be described as a simple Zeeman splitting. In addition, our results also open an additional

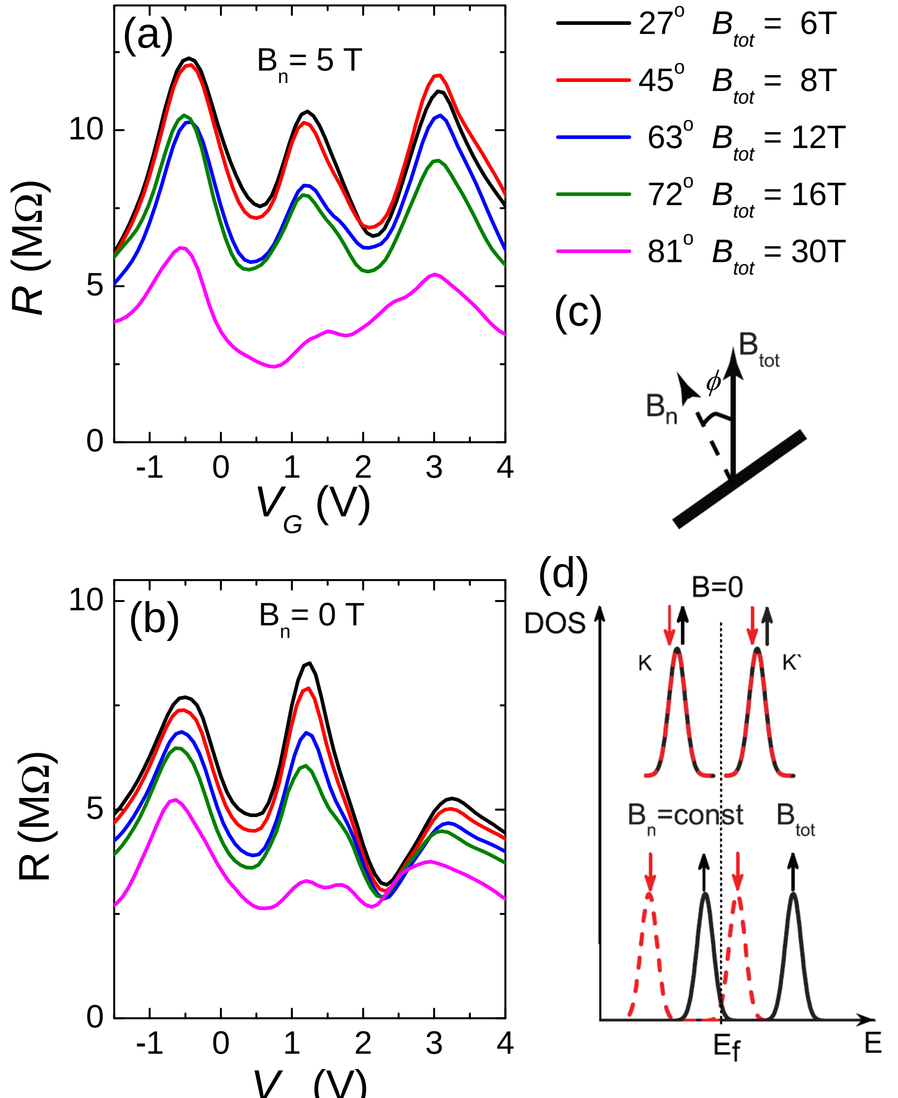

Figure 6.4: *(a) Behavior of the resistance at the charge neutrality point at fixed B_n with increasing B_{tot}. From top to bottom, angle and total field are 27° (6 T), 45° (8 T), 63° (12 T), 72° (16 T), and 81° (30 T) (b) Behavior of the resistance at the charge neutrality point when B has only the in-plane field component ($\phi = 90°$). (c) Definition of the angle ϕ between the total magnetic field B_{tot} and the perpendicular field B_n. (d) Suggested scheme of the spontaneously valley splitting followed by spin splitting induced by B.*

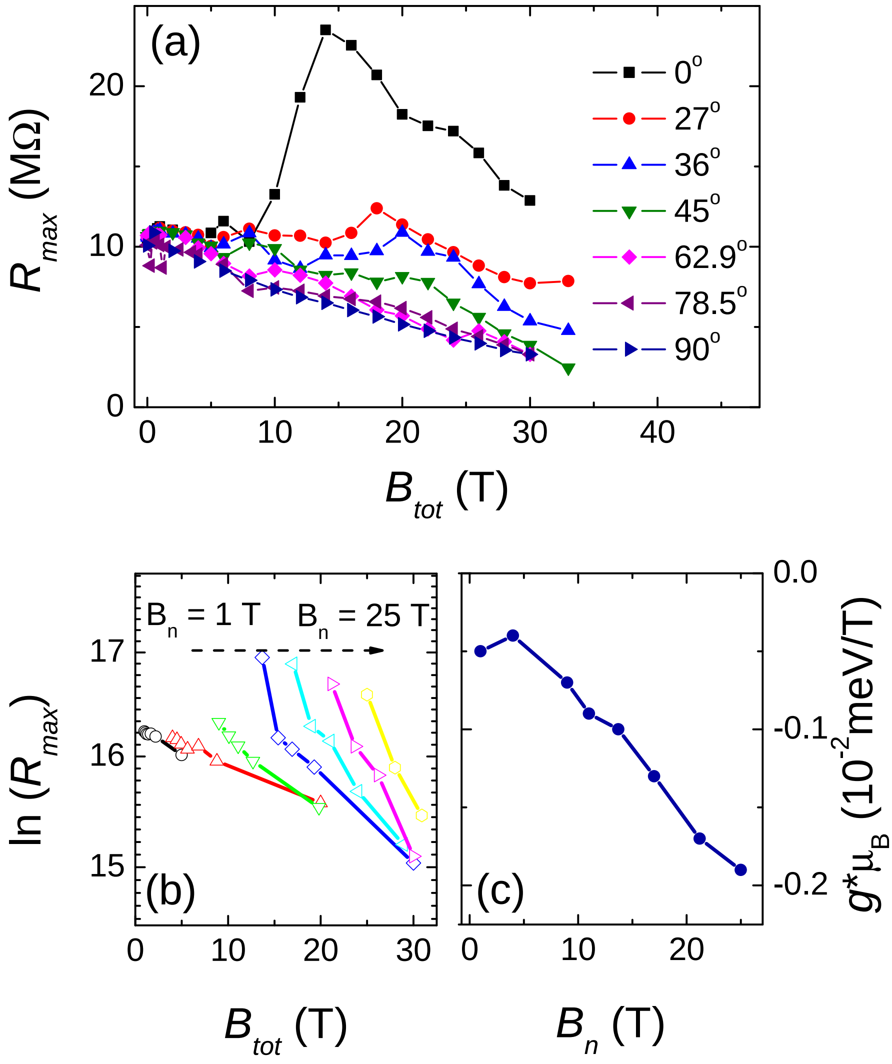

Figure 6.5: *(a) Change in the* R_{max} *of the middle peak with total magnetic field* B_{tot}*. (b)* $\ln(R_{max})$ *as a function of* B_{tot} *at different* B_n*. The values of* B_n *from left to right are 1, 4, 9, 13.7, 17, 21.2, and 25 T. (c) The slope of the linear fit from (b) as a function of the perpendicular field* B_n*.*

question: What is the role of exchange energy and level broadening Γ in the LAF state? Naively, the scaling of $g^*\mu_B$ with B_n can be understood from their dependence on the level broadening Γ. The Γ value scales with $\sqrt{B_n}$, meaning that for bigger B_n a smaller B_{tot} is needed to observe overlapping of the levels. In reality the situation can be much more complicated, including possible exchange mechanisms that we do not understand yet. This is also supported by the fact that the ground-state gap Δ depends on B_n as well.

Based on these results we suggest a possible scenario of symmetry breaking in high quality bilayer graphene [Fig. 6.3(e) and Fig. 6.4(c)]. The first splitting is caused by valley and results in the observed transport gap. Application of a magnetic field induces spin splitting of both K and K' levels. When B is high enough then the energy of the spin-up level from K will start approaching the spin-down level from K'. The overlapping of the levels will cause a decrease in the resistance at the charge neutrality point. Since we do observe a transport gap in our sample, we exclude a nematic phase transition. In addition to this, the response of the sample in tilted B fits the LAF state. The cause of the valley splitting can be a combination of two effects: electron-electron interaction (which determines the B field behavior of the middle resistance maximum) and a contamination of the sample surface with charged impurities which breaks inversion symmetry (via the introduction of an electrical field).[21]

6.5 Conclusion

We report a transport gap of 3 meV in suspended bilayer graphene at 4.2 K, which increases for decreasing temperature. The sequence of appearance of the QHE plateaus at the filling factor $\nu = 2$ followed by $\nu = 1$ supports the suggestion that the observed gap is caused by symmetry breaking. Measurements in a tilted magnetic field indicates that the resistance at the CNP shows a weak linear decrease with increase of the total magnetic field. Based on this we propose a possible scenario for the symmetry breaking in this particular sample: spontaneous valley splitting at zero magnetic field followed by the splitting of spins originating from different valleys with increasing of B. The gap value and weak response of the sample to applied magnetic field corresponds to the predicted spin-polarized layer-antiferromagnetic state as the groundstate of the sample. The observed non-trivial dependence of the gap value on the perpendicular field B_n suggests possible exchange mechanisms in the system.

References

[1] E. V. Kurganova, H. J. van Elferen, A. McCollam, L. A. Ponomarenko, K. S. Novoselov, A. Veligura, B. J. van Wees, J. C. Maan, and U. Zeitler, “Spin splitting in graphene studied by means of tilted magnetic-field experiments”, *Physical Review B* **84**, 121407 (2011).

[2] K. S. Novoselov, E. McCann, S. V. Morozov, V. I. Fal’ko, M. I. Katsnelson, U. Zeitler, D. Jiang, F. Schedin, and A. K. Geim, “Unconventional quantum Hall effect and Berry’s phase of 2π in bilayer graphene”, *Nature Physics* **2**, 177–180 (2006).

[3] E. McCann and V. I. Falko, “Landau-Level Degeneracy and Quantum Hall Effect in a Graphite Bilayer”, *Physical Review Letters* **96**, 086805 (2006).

[4] B. E. Feldman, J. Martin, and A. Yacoby, “Broken-symmetry states and divergent resistance in suspended bilayer graphene”, *Nature Physics* **5**, 889–893 (2009).

[5] R. T. Weitz, M. T. Allen, B. E. Feldman, J. Martin, and A. Yacoby, “Broken-Symmetry States in Doubly Gated Suspended Bilayer Graphene”, *Science* **330**, 812–816 (2010).

[6] J. Martin, B. E. Feldman, R. T. Weitz, M. T. Allen, and A. Yacoby, “Local Compressibility Measurements of Correlated States in Suspended Bilayer Graphene”, *Physical Review Letters* **105**, 256806 (2010).

[7] J. Velasco, L. Jing, W. Bao, Y. Lee, P. Kratz, V. Aji, M. Bockrath, C. N. Lau, C. Varma, R. Stillwell, D. Smirnov, F. Zhang, J. Jung, and A. H. MacDonald, “Transport spectroscopy of symmetry-broken insulating states in bilayer graphene”, *Nature Nanotechnology* **7**, 156–160 (2012).

[8] H. J. van Elferen, A. Veligura, E. V. Kurganova, U. Zeitler, J. C. Maan, N. Tombros, I. J. Vera-Marun, and B. J. van Wees, “Field-induced quantum Hall ferromagnetism in suspended bilayer graphene”, *Physical Review B* **85**, 115408 (2012).

[9] F. Freitag, J. Trbovic, M. Weiss, and C. Schonenberger, “Spontaneously Gapped Ground State in Suspended Bilayer Graphene”, *Physical Review Letters* **108**, 076602 (2012).

[10] A. S. Mayorov, D. C. Elias, M. Mucha-Kruczynski, R. V. Gorbachev, T. Tudorovskiy, A. Zhukov, S. V. Morozov, M. I. Katsnelson, V. I. Falko,

A. K. Geim, and K. S. Novoselov, “Interaction-Driven Spectrum Reconstruction in Bilayer Graphene”, *Science* **333**, 860–863 (2011).

[11] W. Bao, j. Velasco Jr, F. Zhang, l. Jing, B. Standley, D. Smirnov, M. Bockrath, A. MacDonald, and C. N. Lau, “Minimum Conductivity and Evidence for Phase Transitions in Ultra-clean Bilayer Graphene”, *arXiv:1202.3212v1* (2012).

[12] R. Nandkishore and L. Levitov, “Dynamical Screening and Excitonic Instability in Bilayer Graphene”, *Physical Review Letters* **104**, 156803 (2010).

[13] R. Nandkishore and L. Levitov, “Electron interactions in bilayer graphene: Marginal Fermi liquid and zero-bias anomaly”, *Physical Review B* **82**, 115431 (2010).

[14] H. Min, G. Borghi, M. Polini, and A. H. MacDonald, “Pseudospin magnetism in graphene”, *Physical Review B* **77**, 041407 (2008).

[15] F. Zhang, H. Min, M. Polini, and A. H. MacDonald, “Spontaneous inversion symmetry breaking in graphene bilayers”, *Physical Review B* **81**, 041402 (2010).

[16] J. Jung, F. Zhang, and A. H. MacDonald, “Lattice theory of pseudospin ferromagnetism in bilayer graphene: Competing interaction-induced quantum Hall states”, *Physical Review B* **83**, 115408 (2011).

[17] F. Zhang, J. Jung, G. A. Fiete, Q. Niu, and A. H. MacDonald, “Spontaneous Quantum Hall States in Chirally Stacked Few-Layer Graphene Systems”, *Physical Review Letters* **106**, 156801 (2011).

[18] O. Vafek and K. Yang, “Many-body instability of Coulomb interacting bilayer graphene: Renormalization group approach”, *Physical Review B* **81**, 041401 (2010).

[19] Y. Lemonik, I. L. Aleiner, C. Toke, and V. I. Falko, “Spontaneous symmetry breaking and Lifshitz transition in bilayer graphene”, *Physical Review B* **82**, 201408 (2010).

[20] C. Toke and V. I. Fal’ko, “The effect of the electron-electron interaction on the Lifshitz transition density in bilayer graphene”, *arXiv:0903.2435v1* (2009).

[21] E. V. Castro, K. S. Novoselov, S. V. Morozov, N. M. R. Peres, J. M. B. L. dos Santos, J. Nilsson, F. Guinea, A. K. Geim, and A. H. C. Neto, “Biased

Bilayer Graphene: Semiconductor with a Gap Tunable by the Electric Field Effect", *Physical Review Letters* **99**, 216802 (2007).

[22] F. Zhang and A. H. MacDonald, "Distinguishing Spontaneous Quantum Hall States in Bilayer Graphene", *Physical Review Letters* **108**, 186804 (2012).

[23] L. Zhang, Y. Zhang, J. Camacho, M. Khodas, and I. Zaliznyak, "The experimental observation of quantum Hall effect of l=3 chiral quasiparticles in trilayer graphene", *Nature Physics* **7**, 953–957 (2011).

[24] E. McCann, D. S. L. Abergel, and V. I. Fal'ko, "Electrons in bilayer graphene", *Solid State Communications* **143**, 110–115 (2007).

[25] N. Tombros, A. Veligura, J. Junesch, J. J. van den Berg, P. J. Zomer, M. Wojtaszek, I. J. V. Marun, H. T. Jonkman, and B. J. van Wees, "Large yield production of high mobility freely suspended graphene electronic devices on a polydimethylglutarimide based organic polymer", *Journal of Applied Physics* **109**, 093702 (2011).

[26] N. Tombros, A. Veligura, J. Junesch, M. H. D. Guimaraes, I. J. Vera-Marun, H. T. Jonkman, and B. J. van Wees, "Quantized conductance of a suspended graphene nanoconstriction", *Nature Physics* **7**, 697–700 (2011).

[27] F. Xia, D. B. Farmer, Y.-m. Lin, and P. Avouris, "Graphene Field-Effect Transistors with High On/Off Current Ratio and Large Transport Band Gap at Room Temperature", *Nano Letters* **10**, 715–718 (2010).

[28] N. F. Mott, "Conduction in Non-Crystalline Materials .3. Localized States in a Pseudogap and near Extremities of Conduction and Valence Bands", *Philosophical Magazine* **19**, 835 (1969).

[29] F. Molitor, C. Stampfer, J. Gttinger, A. Jacobsen, T. Ihn, and K. Ensslin, "Energy and transport gaps in etched graphene nanoribbons", *Semiconductor Science and Technology* **25**, 034002 (2010).

[30] C. Stampfer, J. Guttinger, S. Hellmller, F. Molitor, K. Ensslin, and T. Ihn, "Energy Gaps in Etched Graphene Nanoribbons", *Physical Review Letters* **102**, 056403 (2009).

[31] I. J. Vera-Marun, P. J. Zomer, A. Veligura, M. H. D. Guimaraes, L. Visser, N. Tombros, H. J. van Elferen, U. Zeitler, and B. J. van Wees, "Quantum Hall transport as a probe of capacitance profile at graphene edges", *arXiv:1112.5462v1* (2011).

[32] K. I. Bolotin, K. J. Sikes, Z. Jiang, M. Klima, G. Fudenberg, J. Hone, P. Kim, and H. L. Stormer, “Ultrahigh electron mobility in suspended graphene”, *Solid State Communications* **146**, 351–355 (2008).

[33] Y. Zhao, P. Cadden-Zimansky, Z. Jiang, and P. Kim, “Symmetry Breaking in the Zero-Energy Landau Level in Bilayer Graphene”, *Physical Review Letters* **104**, 066801 (2010).

[34] R. J. Nicholas, R. J. Haug, K. v. Klitzing, and G. Weimann, “Exchange enhancement of the spin splitting in a GaAs-GaAlAs heterojunction”, *Physical Review B* **37**, 1294–1302 (1988).

Chapter 7

Lifting of the degeneracy of the lowest Landau level of ABC-trilayer graphene

Abstract

We have studied the magnetotransport properties of suspended ABC-trilayer graphene in tilted magnetic fields up to 33 T. At fields B = 0..10 T we observe a full splitting of the twelve-fold degenerated lowest Landau level, and, in particular the opening of a gap at the charge neutrality point. Quantitative analysis of the derivative of the Hall resistance gives an experimental indication of the hierarchal order of the filling factors, related to the fine structure of the lowest Landau level: filling factors $\nu = 6, 4$*, and 0 are most pronounced, followed by* $\nu = 3$*, and finally* $\nu = 1, 2$*, and 5. The application of a perpendicular magnetic field drives filling factor* $\nu = 0$ *to a valley polarized state. At the highest magnetic fields the spin splitting in the neighboring energy levels causes a suppression of the gap opening at* $\nu = 0$.

Part of this work is in preparation for scientific publication.

7.1 Introduction

Since the discovery of graphene[1,2] lots of fundamental research has been done on this single layer of graphite. Specifically, magnetic fields are used to study the magnetotransport properties, showing half integer quantum Hall effect with four-fold degenerated lowest Landau level (LLL), owing two-fold spin and valley degeneracy.[3] Very quickly after the discovery of graphene, also experiments on bilayer graphene were performed,[4] showing integer quantum Hall effect with eight-fold degenerated lowest Landau level, owing two-fold spin-, valley- and layer-degeneracy. Further investigation of more coupled layers was initially limited by the quality of the samples. Typical mobilities for single layer graphene are μ = 1-1.5 $\mathrm{m^2V^{-1}s^{-1}}$, which drops for increasing number of layers[5] due to an increase in the number of surface defects. However, in pure bulk graphite mobilities up to μ = 50-100 $\mathrm{m^2V^{-1}s^{-1}}$ are obtained[6] caused by the absence of surface related scattering. This observation makes it very probable that further improvement of the quality is also possible for multilayer graphene.
As scientific accepted we know that the main limitation of the mobility is introduced by the underlying substrate.[7] Therefore the mobility can be optimized by either replacing the SiO_2-substrate by hexagonal boron nitride (hBN)[8,9] or ultimately suspending the device from the substrate.[10,11] These methods give typical mobilities approaching (or even exceeding) 100 $\mathrm{m^2V^{-1}s^{-1}}$.
The addition of extra layers to graphene changes the electronic bandstructure. This also implies a change of the magnetotransport properties for the increasing number of layers, marked by the observation of half integer quantum Hall effect for single layer graphene[3] and integer quantum Hall effect for bilayer graphene.[4] Theoretical predictions are made for the appearance quantum Hall effect for an increasing number of layers.[12–14]

The next step in further understanding of the stacking influence on the magnetotransport properties is the investigation of trilayer graphene. Recent experiments have shown new challenging physics with a big variety of results,[15–19] attributed to the two different type of stackings, ABA and ABC.[18,19] An ABA-stacking is described as a coupled bilayer and single layer in where the top layer is aligned with the bottom layer [see Fig. 7.1(a) and (c)], behaving as a superposition of a linear and parabolic dispersion [see Fig. 7.1(e)]. The quantum Hall effect is characterized by the interference of Landau levels originating from both the single as bilayer graphene.[15]
The ABC-trilayer, three coupled single layers [see Fig. 7.1(b) and (d)], has a reconstructed bandstructure which has both a linear and parabolic character [see Fig. 7.1(f)]. The QHE shows a characteristic twelve-fold degeneracy of the

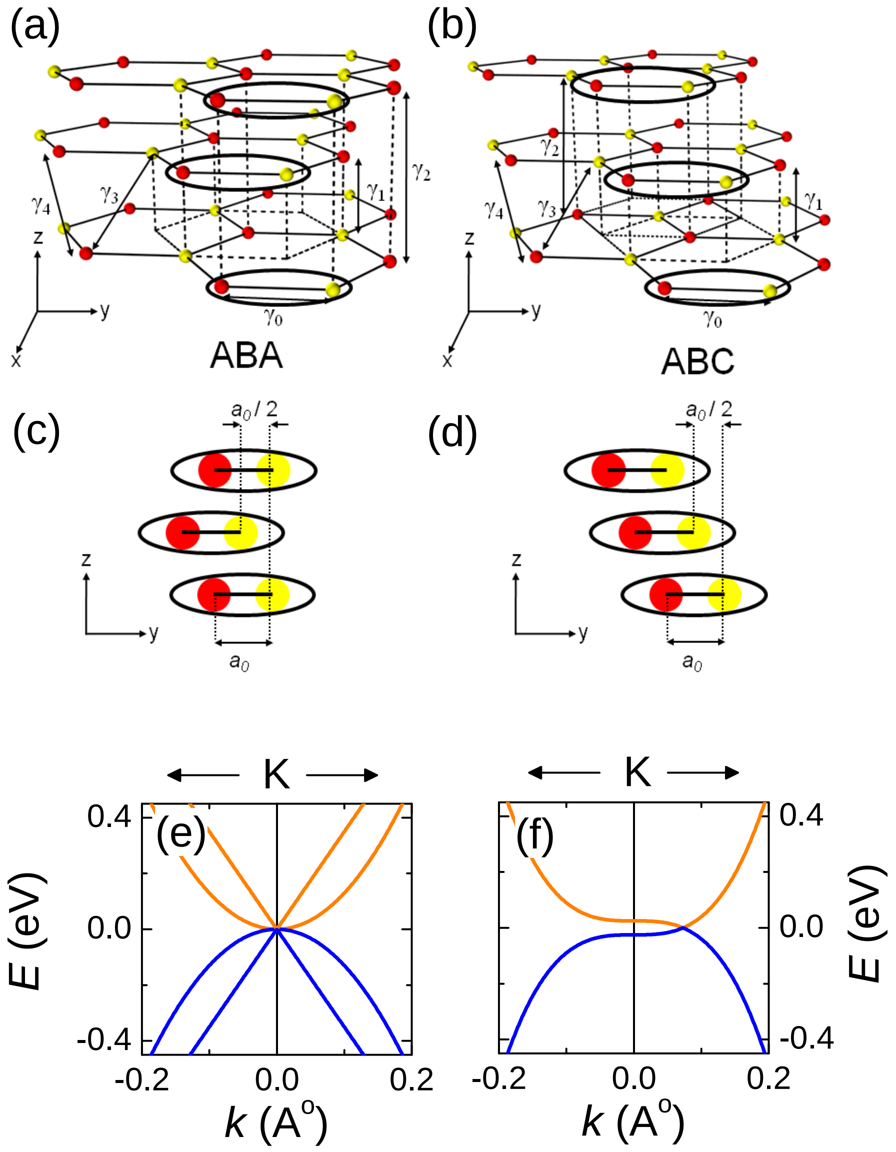

Figure 7.1: *(a, c) 3D impression (a) and a side-view (c) of an ABA-trilayer graphene. (b, d) 3D impression (b) and a side-view (d) of an ABC-trilayer graphene. (e) The bandstructure near the K(K')-points of an ABA-trilayer, formed by the superposition of a linear and a parabolic dispersion. (f) Reconstructed bandstructure near the K(K')-points for ABC-trilayer graphene.*

lowest Landau level and Berry phase 3π.[16–19] When the quality of the device is high enough we are able to study the fine structure of the samples, showing quantized energy states corresponding to spin, valley, and layer degeneracy lifting.

In this chapter we study the magnetotransport properties of the lowest Landau level in suspended ABC-trilayer graphene, in particular the lifting of the twelve-fold degenerated lowest Landau level. Quantitative analysis on the derivative of the Hall-resistance with respect to the charge carrier concentration yields typical field strengths B_0 where quantized states appear. This points to a hierarchal order of appearance: filling factors $\nu = 6, 4$, and 0 are most pronounced, followed by $\nu = 3$, and finally $\nu = 1, 2$, and 5. Finally we focus our attention on the appearance of filling factor $\nu = 0$ that remains observable up to the highest field. Using experiments in tilted magnetic field up to 33 T we show that the $\nu = 0$-state is valley polarized, and that this valley gap can be suppressed by spin-splitting in the neighboring energy levels.

7.2 Experimental background

We have prepared a suspended trilayer graphene sample (TLG) using an acid free method.[11] Following standard techniques,[1] we first exfoliated flakes from highly oriented pyrolytic graphite (HOPG) and deposited them on a Si/SiO$_2$ substrate covered with a 1.15 μm thick LOR-A resist layer. The TLG-flake was then identified on thickness by its optical contrast.[20] [see section 3.3] Subsequently, two electron beam lithography steps were performed in order to contact the flake with Ti-Au contacts and to remove part of the LOR-A below the graphene flake. The resulting device is freely suspended across a trench formed in the LOR-A with two metallic contacts on each side. [see section 3.6 and Ref. 11]

Carriers in the sample can be induced by applying a back-gate voltage V_G on the highly n-doped Si-wafer. The geometrical gate capacitance is given by a combination of the vacuum gap (1.15 μm) and SiO$_2$-substrate (0.5 μm). Using a serial capacitor model we calculate a gate capacitance of 7.2 aF/μm^{-2} which directly relates the carrier concentration to the gate voltage V_G as $n = \alpha(V_G - V_{CNP})$ with leverage factor $\alpha = 1.0 \times 10^{14}$ m^{-2}V^{-1} and the charge neutrality point (CNP) centered at $V_{CNP} = 3$ V.

After mounting, the devices were slowly cooled down to 4.2 K and current annealed[21] by applying a dc bias current up to 3 mA [this particular annealing is shown in section 3.6]. The local annealing resulted into a high quality sample where the CNP is centered around 3 V, see 0 T data in Fig. 7.2(a). The mobility μ is defined as $\mu = \frac{1}{e}\frac{w}{L}\frac{\mathrm{d}G}{\mathrm{d}n}$ in where e is the electron charge, w the width of the flake, L the length of the flake, G the conduction, and n the charge carrier concentration. In Fig. 7.2(a) we show with the dashed lines two regions in where the conductance G changes linearly with the concentration n, which gives for low concentration a mobility $\mu \approx 3$ m^2/Vs and for high concentration a mobility $\mu \approx 0.2$ m^2/Vs. These two concentration dependent mobilities are based on the dimension of the suspended graphene before current annealing: $w = 0.5$ μm wide and $L = 1.3$ μm long. However, in the membrane the distribution of the temperature while current annealing is non-homogenous,[22] which most probably leads to the middle part of the membrane being annealed and non annealed regions close to the contacts. This leads to an underestimation of the mobility since the aspect-ratio $\frac{w}{L}$ is in reality slightly bigger.

Measurements were performed with low-frequency (1.87 Hz) lock-in technique with excitation current of $I \leq 1$ nA, determined by applying an excitation voltage of 45 mV over an in series connected preresistor of 45 MΩ. For measured resistances exceeding 10 MΩ we monitor the excitation current flowing through the sample, and correct afterwards for the influence of the sample on the total excitation current. Resistances exceeding 100 MΩ are determined by calculating the total impedance of the circuit, taking into account the 100 MΩ of the preamplifier and the complex impedance of the contact-wires. Local self-heating on high resistances is avoided by the constant applied excitation voltage of 45 mV over the in series connected preresistor and sample, leading at resistances exceeding 100 MΩ to a decreasing power dissipation $P = V^2/R$ which stays in the order of picowatts.
In order to estimate the angle ϕ, the angle between the total magnetic field B_{tot} and the perpendicular component $B_n = B_{tot}\cos(\phi)$, we use the Hall-resistance of a second sample on the same substrate (connected in a Hall-bar configuration). The angle precision is mainly limited by the bending of the membrane under influence of all external forces (e.g. magnetic field, electric field, gravity, etc.). Assuming a homogenous bending of approximatively 25-50 nm[23] of a 1.3 μm long membrane gives an error in the order of 1-2 degrees.

7.3 Transport properties in the quantum Hall regime

In Fig. 7.2(a) we show the two terminal conductance $G = R^{-1}$ as a function of the applied backgate-voltage V_G of our sample in perpendicular magnetic field ($\phi = 0$). We have subtracted a constant background-resistance of 550 Ω

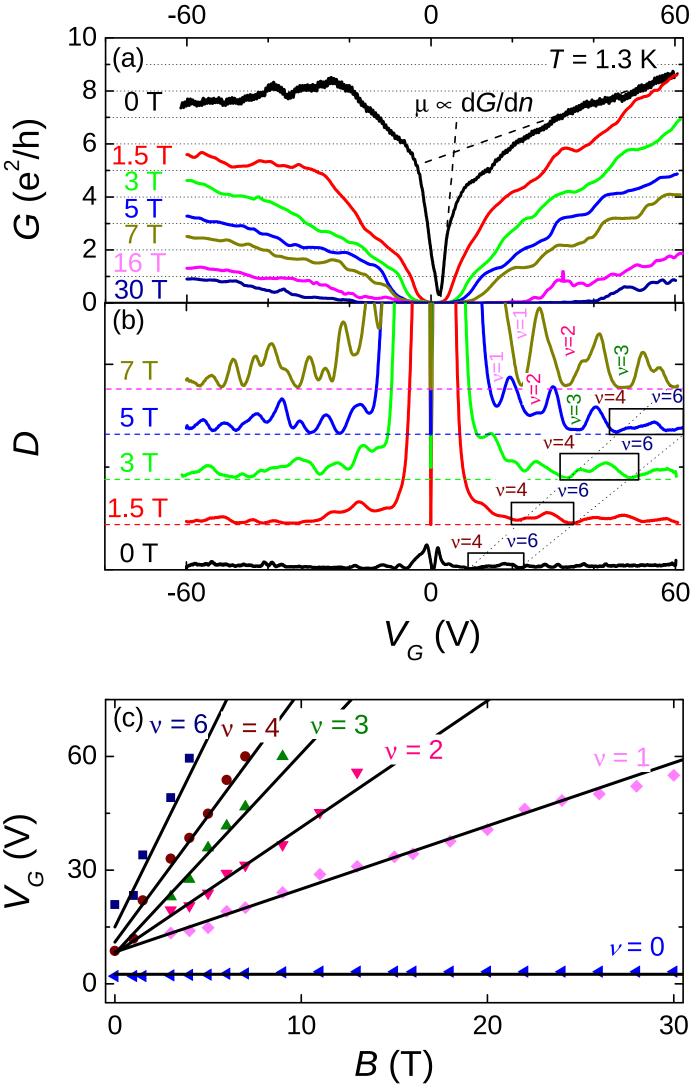

Figure 7.2: *(a) Conductance traces at $T = 1.3$ K for magnetic fields $B = 0..30$ T. Formation of R_{xy}-plateaus for increasing field. The dashed lines through the 0 T data represent the two different slopes $D = \frac{dG}{dV_G}$ which are used to estimate the upper/lower limit of the device mobility. (b) Differential resistance $V_G \frac{dR}{dV_G}$ for magnetic fields 0 T, 1.5 T, 3 T, 5 T and 7 T. Formation of distinct minima in D, corresponding to the formation of the R_{xy}-plateaus in Fig. 7.2(a). The boxes indicate the oscillations around $\nu = 6$ and $\nu = 4$ moving to higher gate-voltage for increasing magnetic field. (Curves are shifted up for clarity) (c) Position of the minima for $\nu =$ 6, 4, 3, 2 and 1 for increasing magnetic field B. The diagonal lines indicate the theoretical lines $V_G = \nu \frac{e}{\alpha h} B$ for filling factors $\nu =$ 0, 1, 2, 3, 4 and 6.*

originating from the finite wire- and lead-resistance. Already at zero magnetic field we observe a very sharp minimum in the conductance around the CNP, indicating the formation of a gap. This gap starts to grow rapidly when applying a magnetic field, which we will study in section 7.4. A closer look at non-zero concentration demonstrates that the quantum Hall plateaus at filling factors $\nu = 4$ and $\nu = 6$ start to develop for small magnetic fields in the range 0..1.5 T, see Fig. 7.2(a). Filling factors $\nu = 4$ and 6 move for increasing magnetic field linearly to higher concentration $n = \nu \frac{eB}{h}$ and leave for fields exceeding 7 T the experimental limited window, -60...60 V. A further increase of the magnetic field up to 10 T results in the complete lifting of the lowest Landau level, the formation of quantized Hall plateaus at filling factors $\nu = 5$, 3, 2 and 1.

The shown conductance G is the inverse of the resistance R, which is a superposition of the magnetoresistance R_{xx} and the Hall resistance R_{xy}, $R = R_{xx} + R_{xy}$. It appears that the total resistance R in Fig. 7.2(a) for high concentrations is characterized by a dominating Hall-resistance R_{xy}, indicated by the formation of R_{xy}-plateaus instead of R_{xx}-minima. In order to estimate the shape of the magnetoresistance we can use the proportionality between the R_{xy}-derivative and R_{xx}, i.e. $R_{xx} \propto V_G \frac{\mathrm{d}R_{xy}}{\mathrm{d}V_G}$ [see chapter 5 and reference 24].

$$D = V_G \frac{\mathrm{d}R_{xy}}{\mathrm{d}V_G} \tag{7.1}$$

For this we define a differential resistance D, which is shown in Fig. 7.2(b) for the measured data in Fig. 7.2(a) (curves are shifted for clarity). The formed R_{xy}-plateaus result in distinct minima in D, which makes it more clear to follow the development of the appearing filling factors. On the hole-doped side the background-resistance is changing for increasing field and it becomes hard to distinguish the different plateaus and corresponding minima from the background-resistance, therefore we will focus from here on the electron side only.

The indicated boxes in Fig. 7.2(b) mark the area from filling factor 4 to 6 moving for increasing magnetic field to higher applied gate-voltage. Also the indicated minima around filling factors $\nu = 1$, 2, and 3 move linearly to higher gate voltage for increasing field. In Fig. 7.2(c) we follow these minima indicated by the center of filling factors $\nu = 0, 1, 2, 3, 4, 6$. For fields $B > 1$ T the filling factors scale linearly with the relation between the applied field and the gate voltage, $V_G = \nu \frac{e}{\alpha h} B$, indicated by the solid lines in Fig. 7.2(c). For the very low fields $B < 1$ T we see the values start to deviate strongly from this linear dependence, explained by the persistence of the quantized states down to zero field.[22, 25]

We will study now in more detail the development of filling factors $\nu = 6$, 4, 3, 2, and 1 quantitatively by determining a typical magnetic field B_0 at which quantization appears. In Fig. 7.3(a) we show D for 3 T, 5 T and 7 T at 1.3 K plotted as a function of the filling factor ν. Here we show how the oscillation amplitude increases with increasing field until fully developed R_{xy}-plateaus appear. Our quantitative analysis of the amplitudes A_ν is analogue to the determination of the Dingle temperature T_D in chapter 5, which was a first attempt to quantify the order of appearance. Our model is based on the Lifshitz-Kosevic formula[26] $\Delta R = A(B) \cdot \sin\left(2\pi\left(\frac{F}{B} - \gamma\right)\right)$ in where the amplitude $A(B)$ is the product $R_T \cdot R_D$. Here R_T is the temperature activated term and R_D the B-dependent term which saturates when $\Delta(B) >> k_B T_D$, where $\Delta(B)$ is the excitation gap at the filling factor and T_D the Dingle temperature. In order to study the field character of the amplitude R_D only we performed all measurements at a constant temperature $T = 1.3$ K.

Analogue to the Dingle theory the factor R_D is exponentially proportional to $1/B$, $R_B \propto \exp\left(-\frac{B_0}{B}\right)$ and is only valid for the regime where the two neighboring Landau levels are still overlapping, i.e. $\Gamma \sim \Delta$. Filling factors that appear first have a typically low B_0, while less pronounced filling factors have a reasonably high B_0. Quantitatively B_0 describes the magnetic field value at which we reach 37 % of the maximum amplitude value.

In Fig. 7.3(b) we show how the oscillation amplitude A_ν at 5 T is defined, the distance from the oscillation minimum to the average of the two neighboring maxima. We plot these amplitudes values A_ν in Fig. 7.3(c) as a function of $1/B$. The solid lines indicate the slope of the datapoints and directly determines the values B_0 given in table 7.1.

ν	6	4	3	2	1
B_0 (T)	1 ± 0.5	2 ± 0.5	4 ± 1	14 ± 2	14 ± 2

Table 7.1: *Specific field values B_0 for filling factors $\nu = 6$, 4, 3, 2, and 1.*

We use these values of B_0 to determine qualitatively the hierarchy of the filling factors, a lower B_0-value describes a stronger appearance of the filling factor. These values indicate that for the lowest fields we observe quantized states at $\nu = 6$, followed quickly by the diverging resistance at filling factor $\nu = 0$ and the development of a plateau at filling factor $\nu = 4$. After the development of filling factors $\nu = 6$, 4, and 0 we observe the development of filling factor 3 and

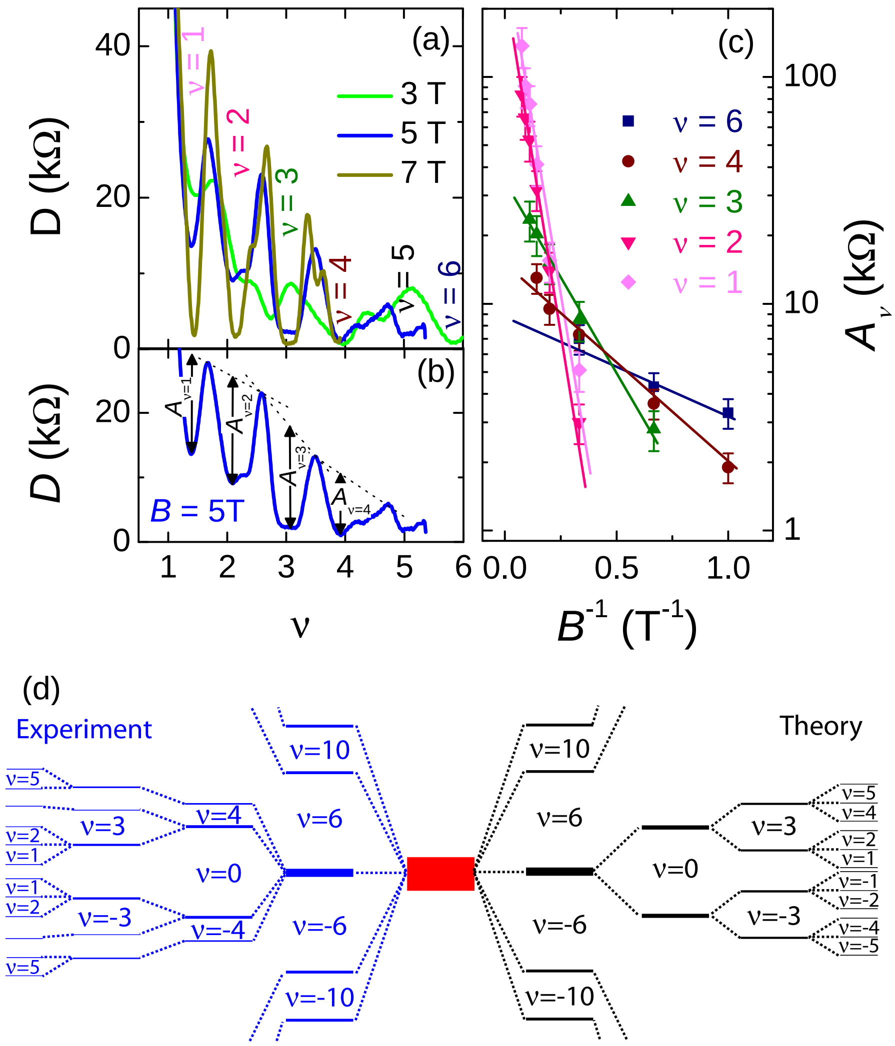

Figure 7.3: *(a) Differential resistance D as a function of the filling factor for $B = 3$ T, 5 T and 7 T. (b) Amplitudes A_ν for $\nu = 4$, 3, 2, and 1 for $B = 5$ T. (c) Oscillation amplitude A_ν as a function of $1/B$ for filling factors 6, 4, 3, 2, and 1. (d) Qualitative schematic of zero-energy Landau level in ABC-trilayer graphene. Theoretical expected hierarchy following Hunds rules (right, black) and experimental observed hierarchy (left, blue)*

finally developing quantized states at filling factors $\nu = 1$, 2 and 5. Here we qualitatively estimate the appearance of $\nu = 5$ by comparing it to the formation of plateaus and minima of other filling factors in Fig. 7.2(a/b).

In Fig. 7.3(d) we summarize on the left side these experimental observations and make a hierarchial schematic. This hierarchal schematic is compared to the theoretical hierarchial order [right side Fig. 7.3(d)] based on Hunds rules for an ABC-TLG.[27] The development of filling factor 6 from already low fields is a clear indication for TLG.[16–19] Subsequently the appearance of filling factors $\nu = 3$ and at even higher fields $\nu = 1$, 2 and 5 is in agreement with the Hunds rules of ABC-trilayer graphene.[27] The most remarkable feature for the existence of an ABC-TLG is the opening of a gap at $\nu = 0$,[27] while an ABA-TLG is expected to stay ungapped for the application of a magnetic field.[28] In section 7.4 we will focus our attention on the opening of this gap. The development of filling factor $\nu = 4$ is in contradiction with Hunds rules for ABC-trilayer graphene, which might be attributed to a layer asymmetry caused by an external electric field of the backgate or local inhomogeneities.[29]

7.4 Formation of a gap at the CNP

Now we move our attention back to the diverging resistance at the CNP, indicating the appearance of a gap at filling factor $\nu = 0$. The existence of a plateau at $\nu = 6$ and the opening of a gap at $\nu = 0$ (see section 7.3) are clear benchmarks for TLG with ABC-stacking.[16–19] In this section we will investigate the reason for the insulating phase at the CNP, which is very similar to the existence of the gap in bilayer graphene which we studied in chapters 5 and 6.[30,31] We will study the insulating phase by applying tilted magnetic fields up to 33 T.

7.4.1 Opening of a gap at zero magnetic field

In Fig. 7.4(a) we show the experimental data of the two terminal sample in zero magnetic field, plotted is the resistance R as a function of the applied backgate-voltage V_G for $T = 4.2$ K, 2.0 K, and 1.3 K. Already at zero magnetic field we observe a very sharp maximum of the resistance around the CNP, R_{CNP}, which has a strong temperature dependence.

The strong temperature dependence points to the formation of a gap Δ_0, indicating the valence band and conduction band do not touch each other near the K(K')-points. In Fig. 7.4(b) this temperature dependence is elucidated more where we show the measured resistance R_{CNP} for decreasing temperature T

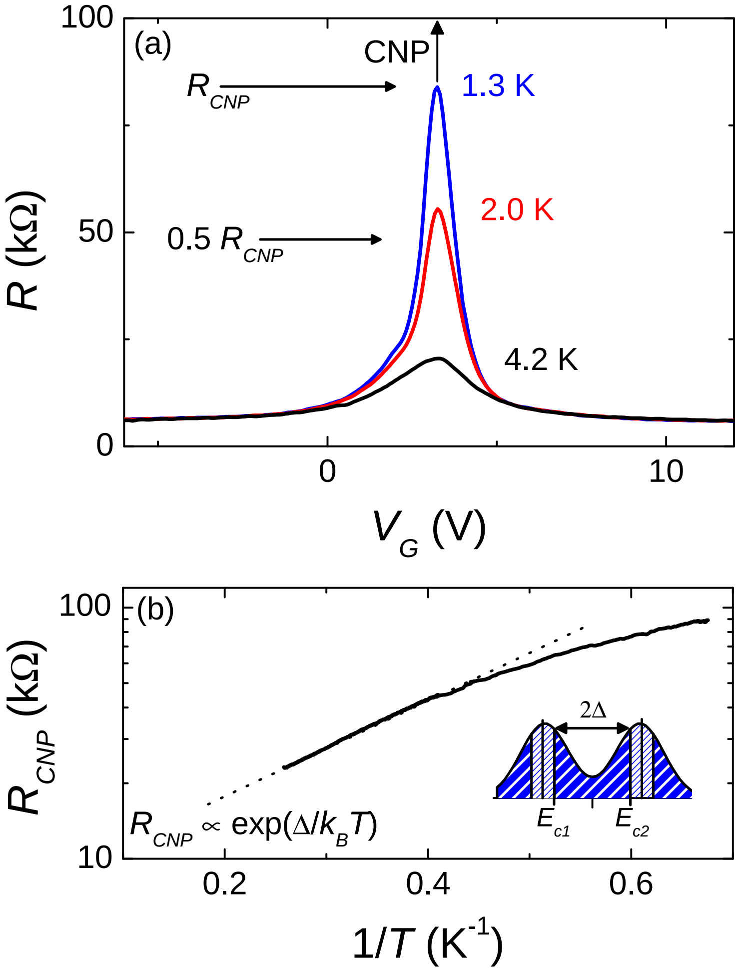

Figure 7.4: *(a) The resistive behavior of the TLG-sample around the CNP for T = 4.2 K, 2.0 K and 1.3 K. (b) Resistance at the CNP, R_{CNP}, (on log-scale) plotted as a function of the inverse temperature T^{-1}, following for high temperatures an Arrhenius activated transport-behavior (right inset).*

in the range 4.2..1.3 K and plot R_{CNP} at logarithmic scale as a function of the inverse temperature T^{-1}. For temperatures $T > 2.0$ K the transport at the CNP is dominated by thermal excitations [see right inset Fig. 7.4(b)]. In this case the resistance increase can be described best by Arrhenius activated transport following Eq. (7.2).

$$R_{CNP} \propto \exp\left(\frac{\Delta}{k_B T}\right) \tag{7.2}$$

The slope of the indicated dotted line represents the size of the gap, $\Delta_0 = 0.38$ meV. Below 2.0 K the transport starts to deviate slowly from an Arrhenius-type model and transport is best described by a variable range hopping-model.[32]

7.4.2 Gap-evolution in low magnetic fields

The developed gap at zero magnetic field has also implications for the formation of the Landau levels in a magnetic field. The non-degenerated energy levels at zero field will break up individually in separate Landau levels, while for a zero-gap at 0 T all Landau levels have an extra degree of degeneracy. Fig. 7.5(a) shows how the resistance R_{CNP} evolves as a function of B/T for $T = 1.3$ K, 2.0 K and 4.2 K. Here we assume Ahrrenius-type dominated transport, i.e. $R \propto \exp(\Delta/k_B T)$ with a gap $\Delta \propto B$. We see that the gap Δ from Eq. (7.2) grows up to $B/T = 0.5$ T/K linearly with the magnetic field B with 1.09 meV/T and scales inversely with the temperature, $1/T$. This gap is about one order of magnitude larger than the bare Zeeman gap $\Delta = g\mu_B B_{tot} = 0.116$ meV/T $\cdot B_{tot}$. This means that the gap is either enhanced by exchange interactions or the underlying nature is different than Zeeman-spin.

In order to elucidate the nature of the insulating phase more we tilt the sample in the magnetic field and change by this the ratio between the perpendicular and the total field, $B_n/B_{tot} = \cos(\phi)$. In Fig. 7.5(b) we show the resistive behavior of the CNP as a function of the perpendicular magnetic field, B_n, for angles $\phi = 0°$, 52° and 78.5°. Here we see that the resistive behavior scales up to $B_n = 2$ T almost perfectly with the perpendicular field. The absence of a total field dependence and the size of the gap points towards a non-spin related mechanism which drives the sample to an insulating phase, a quantum Hall insulator, also proposed for both single-layer and bilayer graphene.[33,34]

By tilting the sample to higher angles we reduce the effect of both the exchange interaction and the non-spin dependent mechanisms. Already at a moderate angle of $\phi = 70°$ we see that the resistance up to 0.1 T drops before it follows the

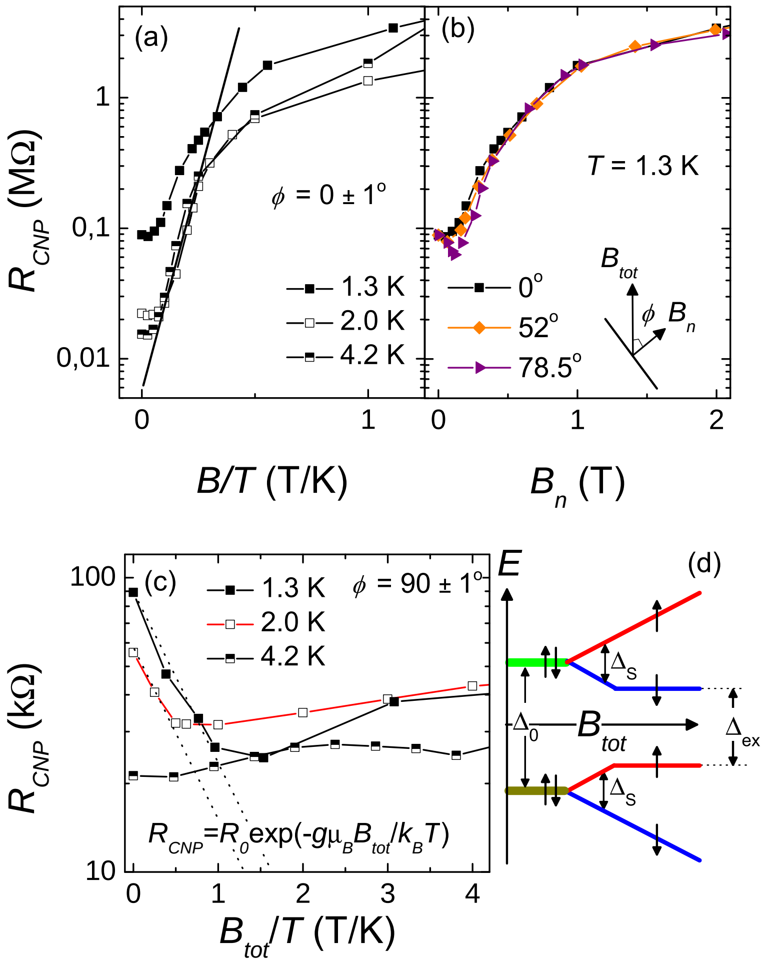

Figure 7.5: *(a) Resistance R_{CNP} plotted as a function of B/T for temperatures T = 4.2 K, 2.0 K and 1.3 K. The data follows one curve and points to a linear B-dependence for fields up to 1.5 T. (b) Resistance R_{CNP} plotted as a function of the perpendicular magnetic field B_n for angles ϕ = 0°, 52°, and 78.5° for T = 1.3 K. R_{CNP} scales with the perpendicular field. inset: the angle ϕ is specified as the angle between the perpendicular magnetic field B_n and the total magnetic field B_{tot}. (c) R_{CNP} plotted as a function of the total magnetic field B_{tot} for $\phi = 90 \pm 1°$. Closing of the zero field gap Δ_0 by application of a parallel field only, scaling with the bare Zeeman-energy $g\mu_B B_{tot}$. For fields exceeding 2 T the resistance remains constant. (d) Theoretical model for the behavior in parallel magnetic field: gap Δ_0 for 0 T closes due to the breaking of the spin-degeneracy in both energy levels. An exchange mechanism prevents further decrease of the gap for parallel fields above 2 T, a finite gap Δ_{ex} = 0.25 meV remains.*

strong perpendicular field dependence [see Fig. 7.5(b)]. In Fig. 7.5(c) we show that for $\phi = 90 \pm 1^\circ$ this decrease becomes even more clear and the resistance drops almost one order of magnitude from 90 kΩ to 20 kΩ and is from here magnetic field independent. The resistance decrease scales exactly with an Arrhenius type of transport $R \propto \exp(-\Delta_S/k_BT)$ with $\Delta_S = g\mu_B B_{tot}$ the bare Zeeman-gap. This suggests that breaking of the spin-degeneracy in the two distinct energies closes the gap Δ_0, qualitatively illustrated in Fig. 7.5(d). From a certain moment the resistance remains constant and an exchange mechanism prevents the two energy levels to approach even more. The exchange energy Δ_{ex} at which the energy levels stay apart is in the order of 0.25 meV. These results are in agreement with a recent work on suspended bilayer graphene [see ref. 35 and chapter 6]: also here at zero field the gap in bilayer graphene is opened and the application of a parallel field causes a strong decrease of the resistance R_{CNP}.

7.4.3 Gap-evolution in high magnetic fields

By increasing the magnetic field further R_{CNP} bends strongly and starts to get temperature independent [see Fig. 7.6(a)]. The temperature independence implies that the system does not scale anymore with a standard Ahrrenius type of transport; Landau levels are moved so much apart that they do not overlap anymore and the transport is described by a variable range hopping model.[32] Besides the strong bending of the resistance-value R_{CNP} for $B_n > 2$ T we observe a strong decrease of the width of the peak around the CNP. We characterize this change in the width by the halfwidth HW, the fullwidth of the peak around the CNP at halfmaximum $R_{CNP}/2$ [see inset Fig. 7.6(a)]. In Fig. 7.6(b) we show that up to $B_n = 2$ T the HW increases rapidly, followed by a rapid decrease in the region $2\text{T} < B_n < 10$ T, and a moderate increase for $B_n > 10$ T. In order to qualitatively explain the behavior of HW we have a closer look at the density of states (DOS) around zero energy (CNP). The DOS $D(E)$ is characterized by two Gaussian shaped Landau levels spaced by a gap 2Δ and broadened by Γ.

$$D(E) = A \cdot \left[\exp\left(-\frac{(E-\Delta)^2}{2\Gamma^2}\right) + \exp\left(-\frac{(E+\Delta)^2}{2\Gamma^2}\right)\right] \tag{7.3}$$

In order to relate this theoretical formulation of the DOS to the experimental behavior of the conductivity we use the Kubo Greenwood formalism.[36, 37]

$$\sigma_{xx} \propto e \int_{-\infty}^{\infty} \mu(E) D(E) \frac{\partial f(E)}{\partial E} dE \tag{7.4}$$

Here $f(E)=\left(\exp\left(\frac{(E-E_F)}{k_BT}\right)+1\right)^{-1}$ is the Fermi-distribution function, $D(E)$ the density of states, and $\mu(E)$ the mobility. For zero temperature we can approach $\frac{\partial f(E)}{\partial E}\approx\delta(E-E_F)$, which simplifies the integral to $\sigma_{xx}=e\mu(E_F)D(E_F)$. Around the CNP we have $\sigma_{xx}=G=R^{-1}$ and thus we can simulate the resistive behavior in the most simple form as $R(E)=\frac{1}{\mu e}\frac{1}{D(E)}$. The resistance at the CNP, R_{CNP}, is equal to $R(E=0)=\frac{1}{Ae\mu}\exp\left(\frac{\Delta^2}{2\Gamma^2}\right)$. In order to explain the behavior of the halfwidth HW we calculate the energy $E_{1/2}$ at which the resistance $R(E)$ reaches half maximum $\frac{R(E)}{2}$.

$$\begin{aligned}\frac{R(E=0)}{2}&=\frac{1}{Ae\mu}\left[\exp\left(-\frac{(E-\Delta)^2}{2\Gamma^2}\right)+\exp\left(-\frac{(E+\Delta)^2}{2\Gamma^2}\right)\right]^{-1}\\&=R(E=0)\exp\left(\frac{E^2}{2\Gamma^2}\right)\frac{1}{2}\frac{1}{\cosh\left(\frac{E\Delta}{\Gamma^2}\right)}\end{aligned}\tag{7.5}$$

This leads to an equation for the energy $E_{1/2}$ where the resistance is at half maximum, Eq. (7.6).

$$\exp\left(\frac{E^2}{2\Gamma^2}\right)=\cosh\left(\frac{E\Delta}{\Gamma^2}\right)\tag{7.6}$$

We solve this equation in the low field regime where the Landau levels still overlap a lot, $E\Delta<<\Gamma^2$, and in the high fields regime where the Landau levels are moved far apart, $E\Delta>>\Gamma^2$. We approximate now $\ln(\cosh(x))\approx\frac{x^2}{2}$ for $x<<1$ and $\ln(\cosh(x))\approx x-\ln(2)$ for $x>>1$. In both the low and high field regime this leads to two solutions E_+ and E_- used to determine the halfwidth $HW\propto E_{1/2}=E_+-E_-$.

$$HW\propto\left\{\begin{array}{cl}2\Gamma & \text{for}\quad E\Delta<<\Gamma^2\\ 2\sqrt{\Delta^2-\Gamma^2\ln(2)} & \text{for}\quad E\Delta>>\Gamma^2\end{array}\right.\tag{7.7}$$

By increasing the magnetic field the Landau levels move apart and therefore HW increases for $E\Delta<<\Gamma^2$ with Γ proportional to the square root of the field $\Gamma\propto\sqrt{B}$ [the low field regime ($B<2$ T) in Fig. 7.6(b), situation sketched by the left inset]. The proportionality $HW\propto\Gamma$ for low fields ($B<2$ T) is also observable in our measurements of the HW and is marked in Fig. 7.6(b) by the dashed line.

For higher fields (2 T $<B<$ 10 T) the Landau levels move further apart and we enter the regime where $E\Delta\approx\Gamma^2$, here Eq. (7.6) do not have an exact solution, i.e. increasing with $\sqrt{\Delta^2-\Gamma^2\ln(2)}$ [see Eq. (7.7)]. In this intermediate regime $E\Delta\approx\Gamma^2$ this leads to a broadening Γ reducing with HW, which explains the strong reduction of HW in our data. When we enter the high field regime ($B>$ 10 T) we reach the point where $\Delta>>\Gamma$ and HW is proportional to

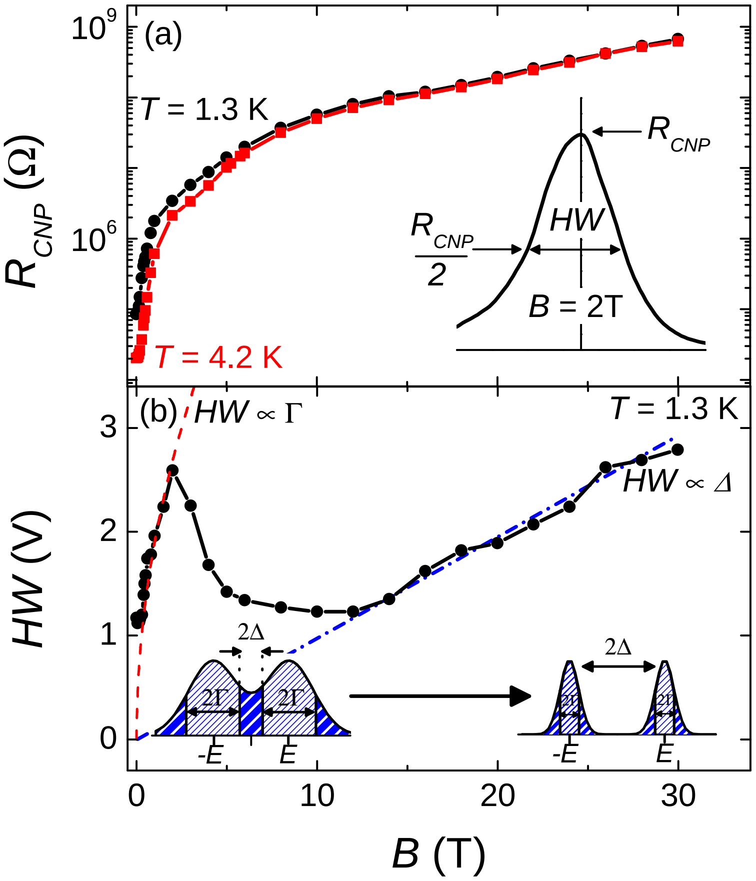

Figure 7.6: *(a) Resistance R_{CNP} plotted as a function of the applied magnetic field B for 1.3 K and 4.2 K. Rapid increase of the resistance for $B < 2$ T, and a smooth transition to a much slower resistance increase for $B > 2$ T. inset: definition of the maximum resistance R_{CNP} and the halfwidth HW, the fullwidth of the CNP at halfmaximum $R_{CNP}/2$. (b) The halfwidth HW of the CNP for the field-range 0-30 T. HW shows a typical Landau level broadening $\Gamma \propto \sqrt{B_n}$ for low fields ($B < 2$ T, dashed line), followed by a rapid decrease of HW (2 T $< B <$ 10 T) and showing a typical linear increase for two distancing fully separated Landau levels ($B >$ 10 T, dash-dotted line). inset: the energy spacing is dominated for low fields by the Landau level broadening Γ (left) and for high fields by the energy spacing Δ (right).*

Δ. In this situation HW is dominated by the distance between the two energy levels, while Γ plays a much smaller role [situation sketched in the right inset of Fig. 7.6(b)]. The linear proportionality $HW \propto 2\Delta$ is marked in Fig. 7.6(b) by the blue dash-dotted line.

7.5 Gap-evolution in tilted high magnetic fields

In order to understand the behavior of the insulating phase at the highest magnetic fields we move now our attention to the resistive behavior in tilted magnetic fields. In Fig. 7.7(a) we show the resistance for various angles $\phi = 0..90°$ in the field range 0..33 T scaled as a function of the perpendicular field. In continuation to the perpendicular field scaling at low fields we observe that after the strong bending of the resistance (B_n = 1-2 T) the scaling with perpendicular field continues up to $B_n = 5$ T. The smooth transition points at the transition from activated transport to a variable range hopping-model and data cannot anymore quantitatively analyzed with an Ahrenius activated transport; therefore we only qualitatively interpret the data from here and makes this a speculative interpretation of the data.

As we have discussed quantitatively already in section 7.4.2 the gap at the CNP indicates no spin-origin. The strongly temperature activated behavior of the CNP at zero field suggests a model in where the valley-degeneracy is already broken from zero field. If we explain the gap-opening in the range 0-1 T as a result of a field induced valley gap Δ_V we can describe the gap at the CNP by the bare valley gap Δ_V and the corresponding exchange energy E_{ex}.[38]

$$\Delta = \Delta_V + E_{ex} \cdot (n_+ - n_-) \tag{7.8}$$

Here Δ_V is the bare valley gap, E_{ex} the exchange energy, and $(n_+ - n_-)$ the normalized difference between the valley-up and the valley-down state. In the low field regime (B_n = 0-1 T) the Landau levels are still overlapping at the CNP, thus $0 > (n_+ - n_-) > 1$. However in the high field regime the Landau levels move far apart, $(n_+ - n_-) \rightarrow 1$. Eq. (7.8) changes in this regime to $\Delta = \Delta_V + E_{ex}$ and thus the strong square root type bending can be explained by a dominating exchange energy E_{ex} which is proportional to the square root of the magnetic field $\sqrt{B_n}$.

Subsequently for fields exceeding 5 T a clear suppression of the resistance R_{CNP} appears for increasing B_{tot}/B_n-ratio. This total field dependence becomes more

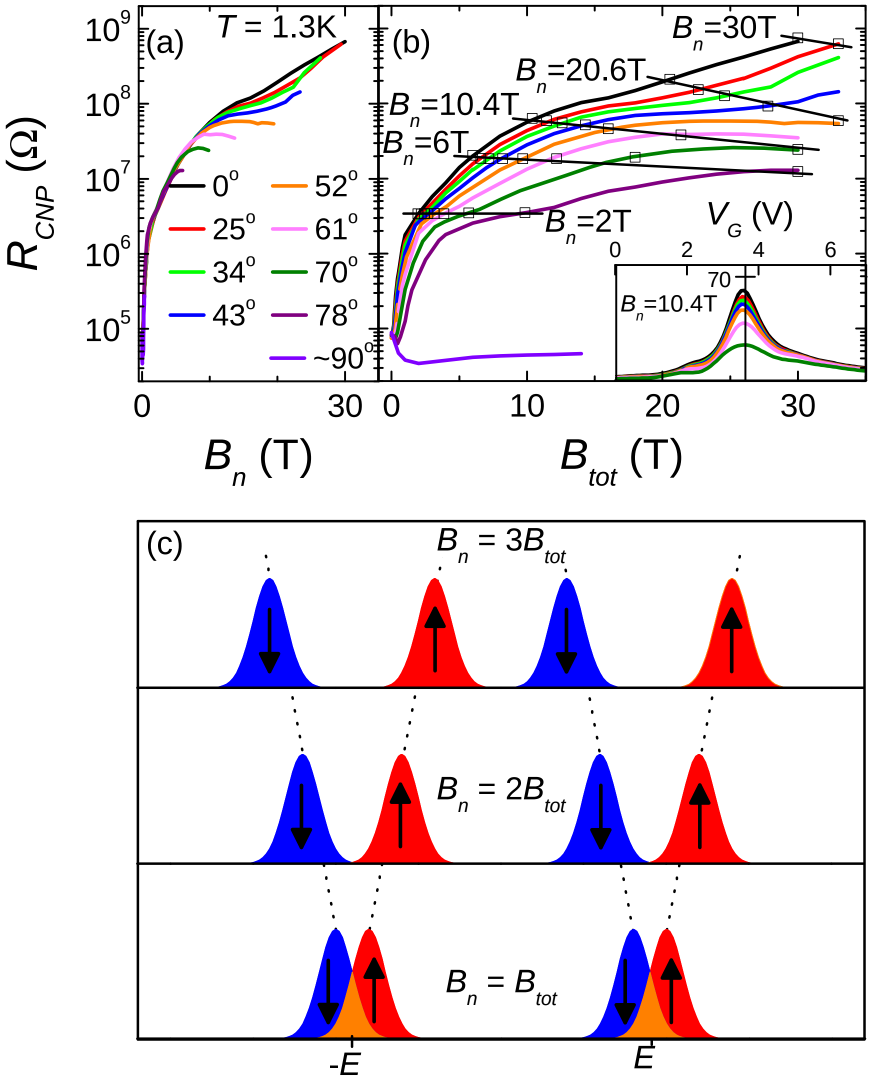

Figure 7.7: *(a) Resistance R_{CNP} plotted as a function of the perpendicular magnetic field B_n for various angles $\phi = 0..90°$. Strong perpendicular field dependence for low fields, crossing over to a total field-dependence. (b) R_{CNP} plotted as a function of the total magnetic field B_{tot} for various angles $\phi = 0..79°$. The squares indicate fixed perpendicular fields 2 T, 6 T, 10.4 T, 20.6 T and 30 T. Decreasing R_{CNP} for fixed B_n and increasing B_{tot}. inset: CNP for $B_n = 10.4$ T for $\phi = 0..70.5°$. (c) Splitting-scenario in fixed perpendicular magnetic field B_n; individual spins originating from the two separated energy levels $\pm E$ move for increasing B_{tot}/B_n-ratio closer to the CNP.*

clear if we focus our attention at a fixed perpendicular field $B_n = 10$ T where the maximum resistance around the CNP is decreased by a factor 2-3 when increasing the total magnetic field [see Fig. 7.7(b)]. This decreasing resistance at constant perpendicular magnetic field is further elucidated in Fig. 7.7(b). Here we plot the data from Fig. 7.7(a) as a function of the total applied magnetic field B_{tot}. We mark data at fixed perpendicular fields 2 T, 6 T, 10.4 T, 20.6 T and 30 T by the square-symbols (□). We observe a linear decreasing trend, very similar to the experiment in a fully parallel magnetic field [Fig. 7.5(c) in section 7.4.2]. However the decrease is here only ≈10 % of the bare spin gap, $\Delta_S = g\mu_B B_{tot}$.

In Fig. 7.7(c) we propose a possible scenario for the decreasing resistance R_{CNP} for increasing B_{tot}/B_n-ratio. The spin-degenerated energy levels at $\pm E$ (bottom Fig. 7.7(c)) consist of a spin-down (blue, $\downarrow$) and a spin-up (red, $\uparrow$). For increasing B_{tot}/B_n-ratio we further split these spin-states and the energy levels move linearly with B_{tot} apart (middle and up). The two approaching energy levels causes an increase of the density of states near zero energy, corresponding to a resistance decrease at the CNP. The change in magnitude of this resistance-decrease for different perpendicular magnetic fields might originate from changing exchange-coupling. Further quantitative measurements are necessary to improve better understanding of this data.

7.6 Conclusion

We have performed magnetotransport experiments on a two-probe suspended ABC-trilayer graphene sample in tilted magnetic field. Experiments in the range 0..10 T show the full breaking of the twelve-fold degenerated lowest Landau level. Quantitative analysis on the derivative of the Hall resistance yields an hierarchal order of appearance: $\nu = 6, 4, 0 \to \nu = 3 \to \nu = 1, 2, 5$. Additionally we have studied the opening of a gap at the CNP. Already at zero magnetic field we observe a gap $\Delta_0 = 0.38$ meV, which in completely parallel field can be closed by the spins originating from both energy levels. The gap at $\nu = 0$ increases linearly with the perpendicular magnetic field and is about one order of magnitude larger than the bare Zeeman gap, which points to a valley polarized state. For high magnetic fields we observe a total field dependence which we explain by the spin-splitting in the two neighboring energy levels, i.e. at fixed perpendicular fields the two inner lying spin-energies approach the CNP and causes a decrease of the resistance.

References

[1] K. S. Novoselov, A. K. Geim, S. V. Morozov, D. Jiang, Y. Zhang, S. V. Dubonos, I. V. Grigorieva, and A. A. Firsov, "Electric field effect in atomically thin carbon films", *Science* **306**, 666–669 (2004).

[2] A. K. Geim and K. S. Novoselov, "The rise of graphene", *Nature Materials* **6**, 183–191 (2007).

[3] Y. Zhang, Y.-W. Tan, H. L. Stormer, and P. Kim, "Experimental observation of the quantum Hall effect and Berry's phase in graphene", *Nature* **438**, 201–204 (2005).

[4] K. S. Novoselov, E. McCann, S. V. Morozov, V. I. Fal'ko, M. I. Katsnelson, U. Zeitler, D. Jiang, F. Schedin, and A. K. Geim, "Unconventional quantum Hall effect and Berry's phase of 2π in bilayer graphene", *Nature Physics* **2**, 177–180 (2006).

[5] K. Nagashio, T. Nishimura, K. Kita, and A. Toriumi, "Mobility Variations in Mono- and Multi-Layer Graphene Films", *Applied Physics Express* **2** (2009).

[6] K. Sugihara, K. Kawamura, and T. Tsuzuku, "Temperature-Dependence of the Average Mobility in Graphite", *Journal of the Physical Society of Japan* **47**, 1210–1215 (1979).

[7] J.-H. Chen, C. Jang, S. Xiao, M. Ishigami, and M. S. Fuhrer, "Intrinsic and extrinsic performance limits of graphene devices on SiO_2", *Nature Nanotechnology* **3**, 206–209 (2008).

[8] C. R. Dean, A. F. Young, I. Meric, C. Lee, L. Wang, S. Sorgenfrei, K. Watanabe, T. Taniguchi, P. Kim, K. L. Shepard, and J. Hone, "Boron nitride substrates for high-quality graphene electronics", *Nature Nanotechnology* **5**, 722–726 (2010).

[9] C. R. Dean, A. F. Young, P. Cadden-Zimansky, L. Wang, H. Ren, K. Watanabe, T. Taniguchi, P. Kim, J. Hone, and K. L. Shepard, "Multicomponent fractional quantum Hall effect in graphene", *Nature Physics* **7**, 693696 (2011).

[10] K. I. Bolotin, K. J. Sikes, Z. Jiang, M. Klima, G. Fudenberg, J. Hone, P. Kim, and H. L. Stormer, "Ultrahigh electron mobility in suspended graphene", *Solid State Communications* **146**, 351–355 (2008).

[11] N. Tombros, A. Veligura, J. Junesch, J. J. van den Berg, P. J. Zomer, M. Wojtaszek, I. J. V. Marun, H. T. Jonkman, and B. J. van Wees, “Large yield production of high mobility freely suspended graphene electronic devices on a polydimethylglutarimide based organic polymer”, *Journal of Applied Physics* **109**, 093702 (2011).

[12] E. McCann and V. I. Falko, “Landau-Level Degeneracy and Quantum Hall Effect in a Graphite Bilayer”, *Physical Review Letters* **96**, 086805 (2006).

[13] F. Guinea, A. H. Castro Neto, and N. M. R. Peres, “Electronic states and Landau levels in graphene stacks”, *Physical Review B* **73**, 245426 (2006).

[14] M. Koshino and E. McCann, “Landau level spectra and the quantum Hall effect of multilayer graphene”, *Physical Review B* **83**, 165443 (2011).

[15] T. Taychatanapat, K. Watanabe, T. Taniguchi, and P. Jarillo-Herrero, “Quantum Hall effect and Landau-level crossing of Dirac fermions in trilayer graphene”, *Nature Physics* **7**, 621–625 (2011).

[16] F. Zhang, H. Min, M. Polini, and A. H. MacDonald, “Spontaneous inversion symmetry breaking in graphene bilayers”, *Physical Review B* **81**, 041402 (2010).

[17] W. Bao, L. Jing, J. Velasco, Y. Lee, G. Liu, D. Tran, B. Standley, M. Aykol, S. B. Cronin, D. Smirnov, M. Koshino, E. McCann, M. Bockrath, and C. N. Lau, “Stacking-dependent band gap and quantum transport in trilayer graphene”, *Nature Physics* **7**, 948–952 (2011).

[18] A. Kumar, W. Escoffier, J. M. Poumirol, C. Faugeras, D. P. Arovas, M. M. Fogler, F. Guinea, S. Roche, M. Goiran, and B. Raquet, “Integer Quantum Hall Effect in Trilayer Graphene”, *Physical Review Letters* **107**, 126806 (2011).

[19] S. H. Jhang, M. F. Craciun, S. Schmidmeier, S. Tokumitsu, S. Russo, M. Yamamoto, Y. Skourski, J. Wosnitza, S. Tarucha, J. Eroms, and C. Strunk, “Stacking-order dependent transport properties of trilayer graphene”, *Physical Review B* **84**, 161408 (2011).

[20] P. Blake, E. W. Hill, A. H. C. Neto, K. S. Novoselov, D. Jiang, R. Yang, T. J. Booth, and A. K. Geim, “Making graphene visible”, *Applied Physics Letters* **91**, 063124 (2007).

[21] J. Moser, A. Barreiro, and A. Bachtold, “Current-induced cleaning of graphene”, *Applied Physics Letters* **91**, 163513 (2007).

[22] N. Tombros, A. Veligura, J. Junesch, M. H. D. Guimaraes, I. J. Vera-Marun, H. T. Jonkman, and B. J. van Wees, "Quantized conductance of a suspended graphene nanoconstriction", *Nature Physics* **7**, 697–700 (2011).

[23] N. Lindahl, D. Midtvedt, J. Svensson, O. A. Nerushev, N. Lindvall, A. Isacsson, and E. E. B. Campbell, "Determination of the Bending Rigidity of Graphene via Electrostatic Actuation of Buckled Membranes", *Nano Letters* **12**, 3526–3531 (2012).

[24] H. J. van Elferen, A. Veligura, E. V. Kurganova, U. Zeitler, J. C. Maan, N. Tombros, I. J. Vera-Marun, and B. J. van Wees, "Field-induced quantum Hall ferromagnetism in suspended bilayer graphene", *Physical Review B* **85**, 115408 (2012).

[25] F. Freitag, J. Trbovic, M. Weiss, and C. Schonenberger, "Spontaneously Gapped Ground State in Suspended Bilayer Graphene", *Physical Review Letters* **108**, 076602 (2012).

[26] I. M. Lifshitz and A. M. Kosevich, "Theory of Magnetic Susceptibility in Metals at Low Temperatures", *Soviet Physics Jetp-Ussr* **2**, 636–645 (1956).

[27] F. Zhang, D. Tilahun, and A. H. MacDonald, "Hund's Rules for the N=0 Landau Levels of Trilayer Graphene", *arXiv:1201.5437v1* (2012).

[28] M. Koshino and E. McCann, "Gate-induced interlayer asymmetry in ABA-stacked trilayer graphene", *Physical Review B* **79**, 125443 (2009).

[29] S. Yuan, R. Roldn, and M. I. Katsnelson, "Landau level spectrum of ABA- and ABC-stacked trilayer graphene", *Physical Review B* **84**, 125455 (2011).

[30] Y. Zhao, P. Cadden-Zimansky, Z. Jiang, and P. Kim, "Symmetry Breaking in the Zero-Energy Landau Level in Bilayer Graphene", *Physical Review Letters* **104**, 066801 (2010).

[31] B. E. Feldman, J. Martin, and A. Yacoby, "Broken-symmetry states and divergent resistance in suspended bilayer graphene", *Nature Physics* **5**, 889–893 (2009).

[32] N. F. Mott, "Conduction in Non-Crystalline Materials .3. Localized States in a Pseudogap and near Extremities of Conduction and Valence Bands", *Philosophical Magazine* **19**, 835 (1969).

[33] Z. Jiang, Y. Zhang, H. L. Stormer, and P. Kim, "Quantum Hall States near the Charge-Neutral Dirac Point in Graphene", *Physical Review Letters* **99**, 106802 (2007).

[34] J. G. Checkelsky, L. Li, and N. P. Ong, "Zero-Energy State in Graphene in a High Magnetic Field", *Physical Review Letters* **100**, 206801 (2008).

[35] A. Veligura, H. J. van Elferen, N. Tombros, J. C. Maan, U. Zeitler, and B. J. van Wees, "Transport gap in suspended bilayer graphene at zero magnetic field", *Physical Review B* **85**, 155412 (2012).

[36] R. Kubo, "A General Expression for the Conductivity Tensor", *Canadian Journal of Physics* **34**, 1274–1277 (1956).

[37] D. A. Greenwood, "The Boltzmann Equation in the Theory of Electrical Conduction in Metals ", *Proceedings Physical Society London* **71**, 585 (1958).

[38] E. V. Kurganova, H. J. van Elferen, A. McCollam, L. A. Ponomarenko, K. S. Novoselov, A. Veligura, B. J. van Wees, J. C. Maan, and U. Zeitler, "Spin splitting in graphene studied by means of tilted magnetic-field experiments", *Physical Review B* **84**, 121407 (2011).

Appendix A

Lithography-recipes

In chapter 3 we described the general procedure how to process graphene-flakes with use of lithography to build a field effect transistor. In this appendix we present in more detail the exact recipe used to make the substrate supported samples presented in this thesis. In section A.1 we describe the method how to cleave the largest and most homogenous flakes of a bulk piece of graphite. Subsequently followed by the the recipes how to process electrical contacts with either EBL-lithography* [section A.2.1] or photolithography [A.2.2].

A.1 Cleavage of graphene-flakes

Graphite is used in many applications, the most rough form we know is used in pencils; graphite is easy to cleave and therefore easy to use as a way to write. By cleaving graphite with a piece of Scotch tape we isolate a single layer of graphite, graphene. Recent developed technics[1,2] to grow single layers of graphene are very useful for industrial applications, however for fundamental understanding we need graphene-layers with highest possible purity. Highest quality flakes are obtained from three types of graphite, natural graphite, kish graphite and HOPG (discussed in section 3.3).

In Fig. A.1 we show how to isolate from a bulk piece of natural graphite a single layer of graphene. We start the procedure by using graphite flakes which are by preference very flat, the flatter the graphite the higher the probability that the graphite-flakes on the surface are nicely homogenous and finally break of in one piece. We place this piece of graphite on a piece of Scotch-tape (a) and try to stick it as good as possible to the sticky side of the tape. After this we remove the bulk piece of graphite gently from the tape (b). A good cleaved

---

*we have used the cleanroom facilities of the university of Groningen

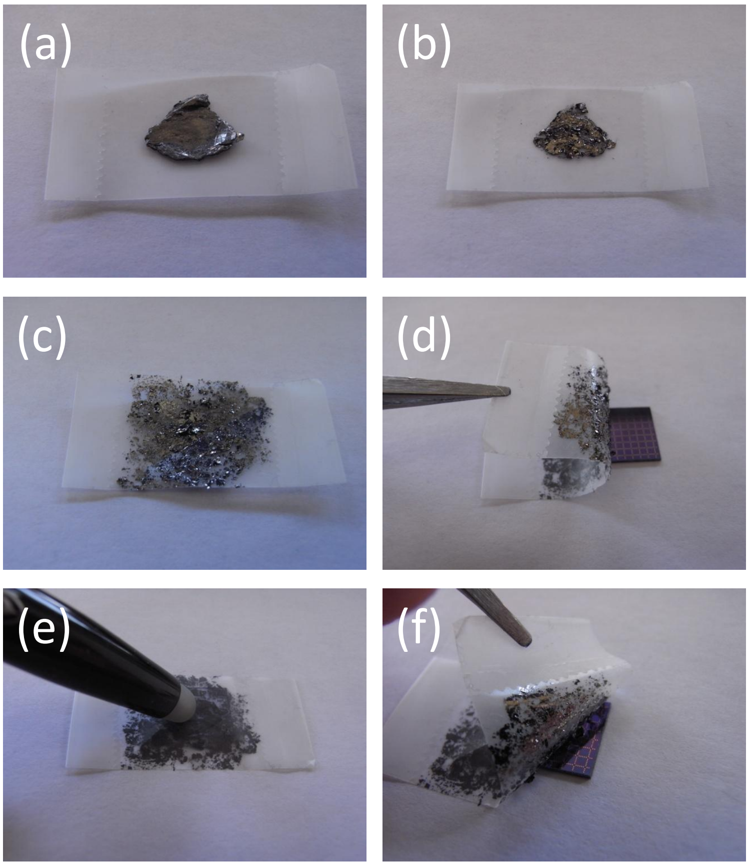

Figure A.1: *General cleaving procedure to obtain single layer graphene-flakes from a bulk piece of graphite. (a) Piece of natural graphite stuck on a piece of Scotch-tape. (b) The graphite flake is gently removed from the tape, much tinner layers of graphite are remaining on the tape. (c) graphite is spread around the tape by folding it several times. (d) The Scotch-tape is moved above a Si/SiO$_2$. (e) The Scotch-tape with graphite is gently pressed on the Si/SiO$_2$, to increase the probability of leaving graphene flakes we can help it a bit with a wiper. (f) The tape is gently removed from the substrate.*

piece of graphite can be recognized by the shiny graphite-flakes on the surface of the tape, which are already clearly lift-off on one side. In some cases it helps to spread the graphite a little bit around the tape (c) by folding it 3-4 times in different orientations. Due to this we make a higher coverage of the graphene on the tape and decrease the layer thickness. After this we move the tape above a piece of Si/SiO_2 (d) and gently press on the surface with a wiper (e). After striking this in different orientations for 3-4 minutes the tape can be removed slowly (f); a typical time to take of the tape is 30 seconds.
Now the surface needs to be inspected for graphene-flakes [this identification process is described in section 3.3]. In general besides the graphene-flakes we leave a lot of graphite flakes and glue-remains on the surface. The glue can be soluted by putting the wafer for approximately 1 minute in pure MIBK (Methyl IsoButyl Keton), followed by drying the substrate with a nitrogen flow. This procedure in general is also good to remove thick layers of graphite which can blockade a decent design of the current leads.

A.2 Lithography on graphene sheet

In section 3.4 and Fig. 3.4 we have described the general process-steps to make electrical contact to a graphene-sheet. We have used two methods to process these steps, electron beam lithography (EBL) and photolithography. In the following two subsections we give the two recipes for these two procedures.

A.2.1 Electron beam lithography

1. Graphene flakes on the substrate are defined and the exact coordinates with respect to several markers are determined [see Fig. A.2.1(a)].
2. We spin with 4000 RPM a 300 nm thick PMMA 950K layer (4% in ethyllactat-n-Butylacetat). Subsequently we do a pre-exposure bake of 1 hour at 170 °C to evaporate all remaining solvents in the polymer layer.
3. A contact-pattern is designed based on the shape of the sample and the surrounding graphite-impurities.
4. The sample is loaded in the EBL and pumped down to $p \approx 1 \cdot 10^{-6}$ mbar. We write the pattern with a dose of 450 C cm^{-2} at 30 kV. After writing the pattern the system is pressurized and the sample can be taken out of the EBL.
5. The sample is developed for 1 minute in a 1:3 solution of MIBK:IPA, followed by a two-fold rinse of 1 minute in IPA. To proper dry out the

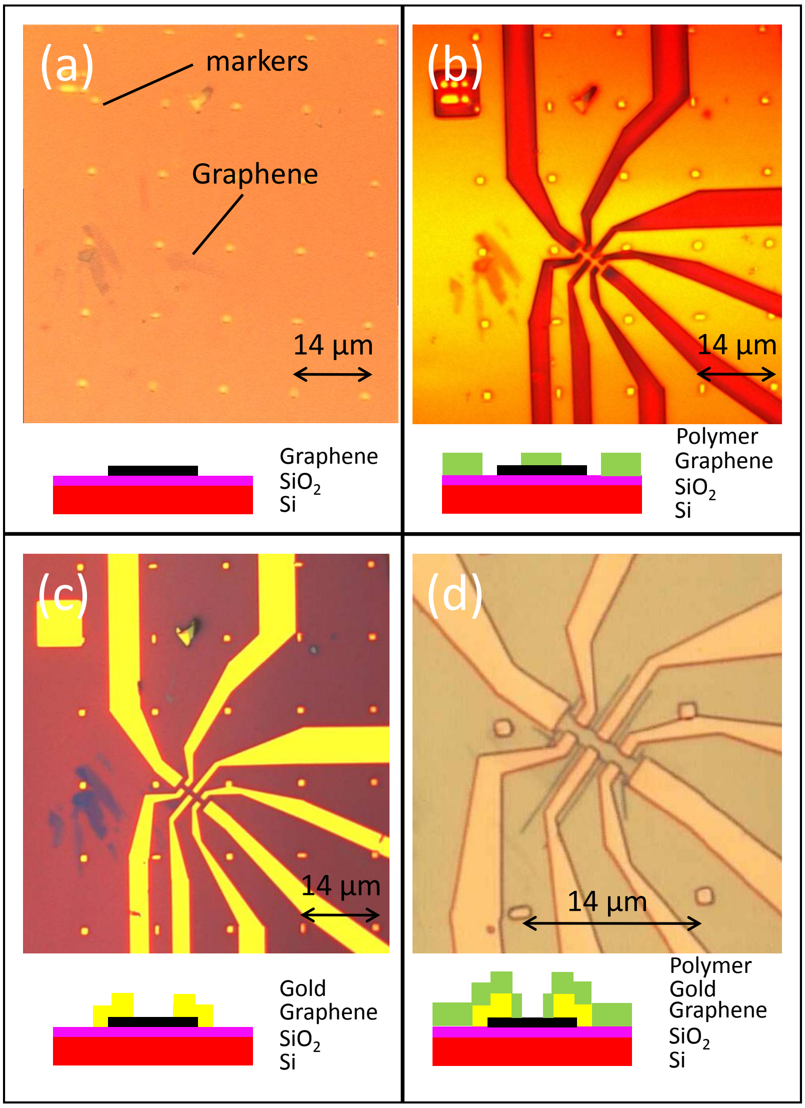

Figure A.2: *Example of the lithography process steps with use of EBL-lithography. (a) Graphene-flake on a Si/SiO$_2$-wafer, surrounded by gold-markers which specify the exact position of the graphene flake. (b) EBL has been used to write a trench in a spincoated layer of PMMA. (c) After evaporation of 3 nm Ti/37 nm Au we have performed the lift-off. (d) A second EBL-step has been performed to write a pattern in the polymer for etching the device with oxygen plasma to a Hall-bar.*

solvent-remains we flush with nitrogen-gas. A typical result after the development is in Fig. A.2.1(b).

6. The sample is mounted in the evaporater and pumped down to $p \approx 5 \cdot 10^{-7}$ mbar. After this, 3 nm of Ti is evaporated on a rate of 0.2 nm/sec, followed by 37 nm Au on 1 nm/sec. After cooling down the sample we can release the pressure and take out the sample.

7. The whole surface is now covered with 3 nm Ti/37 nm Au. By soluting the remaining polymer underneath Ti/Au in Aceton on 55 °C we leave only small contacts on the sample [see Fig. A.2.1(c)].

8. Optionally we perform a second lithography-step to write a pattern in the graphene-itself and define the edges, to make for example a Hall-bar. In Fig A.2.1(d) we show an example of a sample in where we repeat steps 3-6 to write a pattern that defines the edge of the sample. After this we load the sample in a Oxygen-plasma chamber and pump it down to $p \approx 1 \cdot 10^{-6}$ mbar. An oxygen flow of 40 W and with 9 sccm gas flow and a pressure of 2 mbar is exposed for 2 minutes. After this we etched all graphene-layers which were not covered with polymer.

A.2.2 Photolithography

1. Graphene flakes on the substrate are defined and the position is defined with markers to find it more quickly back. In this case we will process the bilayer sample of Fig. A.2.2(a).

2. We spin with 4000 RPM a 1 μm thick diluted nlof 2070 layer (3:10 AZ EBR:AZ nlof 2070). Subsequently we do a pre-exposure bake of 1 minute at 110 °C at a heatplate to evaporate all remaining solvents in the polymer layer.

3. We select a contact-configuration for the sample from a home-made photolithography mask with 300-400 different contact-configurations. We align this configuration above the sample and bring it in hard-contact mode. Subsequently we expose the sample with UV 400 (= 360 nm), 350 W-lamp for 4.5 s.[†]

4. Post-exposure bake at 105 °C for 60 s on a hotplate.

[†] The exposure time can deviate strongly for contact-configurations with spaces smaller than 2 μm, because of the increase of reflected light.

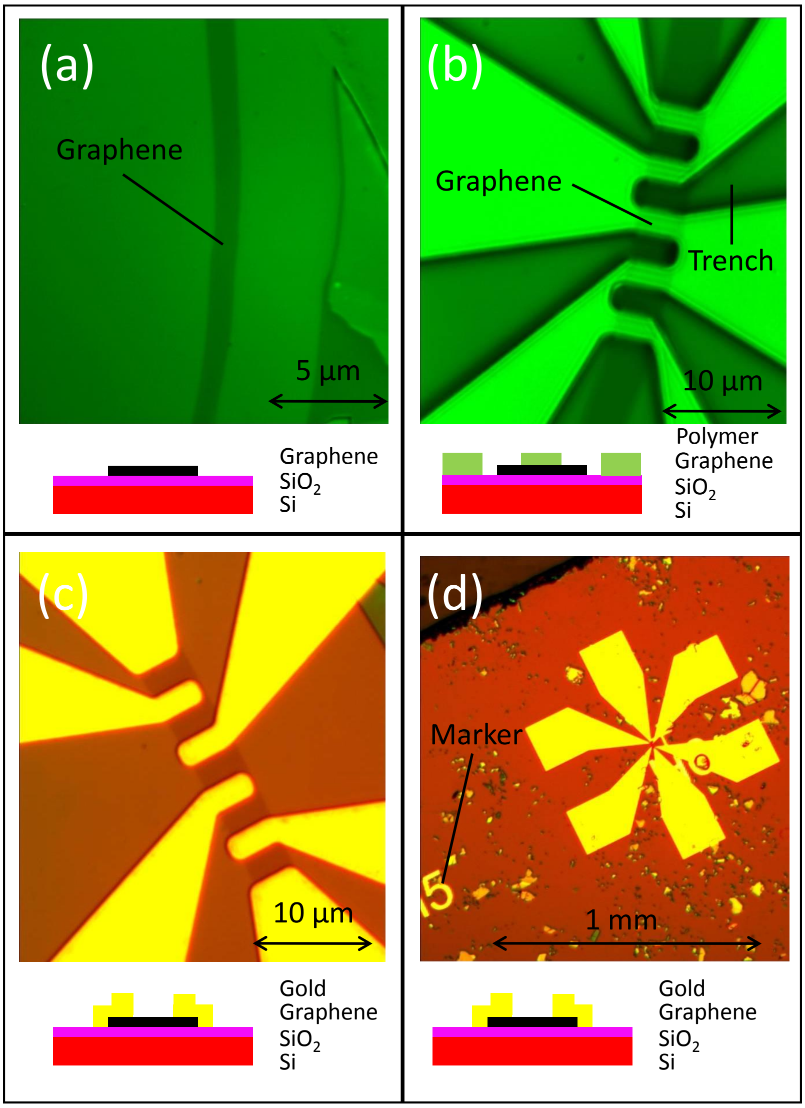

Figure A.3: *Example of the lithography process steps with use of photolithography. (a) Graphene-flake on a Si/SiO_2-wafer. (b) Photolithography has been used to project a predefined pattern on the surface and write a trench in a spincoated layer of nLOF. (c) After evaporation of 3 nm Ti/32 nm Au we have performed lift-off. (d) Overview picture of the predefined structured that is projected on the substrate.*

5. Development for 120 seconds in AZ 276 MIF to dissolve the unexposed regions and subsequently rinsed for 60 s in demineralized water and dried with a nitrogen flow [see Fig. A.2.2(b)]

6. The sample is mounted into the evaporator (UNIVEX 350) and pumped down to 10^{-6} mbar. We evaporate 3 nm Ti at 0.01 nm/s and 32 nm Au at 0.1 nm/s.

7. After evaporation we perform the lift-off of the metal on the remaining polymer by solving the remaining polymer in a bath of N-Methylpyrrolidone.[‡] Optionally the bath of N-Methylpyrrolidone can be warmed up to 80 °C to speed up the lift-off process. Sometimes it is necessary to speed up the lift-off by performing lift-off for 0.1 s in a ultrasonic bath, however this step can be harmful for the sample contacts! In Fig. A.2.2(c/d) is shown the result close to the sample and the overall look on the contact-pattern.

[‡] Be aware that this solvent is toxic

References

[1] S. Bae, H. Kim, Y. Lee, X. Xu, J.-S. Park, Y. Zheng, J. Balakrishnan, T. Lei, H. Ri Kim, Y. I. Song, Y.-J. Kim, K. S. Kim, B. Ozyilmaz, J.-H. Ahn, B. H. Hong, and S. Iijima, “Roll-to-roll production of 30-inch graphene films for transparent electrodes”, *Nature Nanotechnology* **5**, 574–578 (2010).

[2] X. Li, W. Cai, J. An, S. Kim, J. Nah, D. Yang, R. Piner, A. Velamakanni, I. Jung, E. Tutuc, S. K. Banerjee, L. Colombo, and R. S. Ruoff, “Large-Area Synthesis of High-Quality and Uniform Graphene Films on Copper Foils”, *Science* **324**, 1312–1314 (2009).

Appendix B

Field dependence of the leverage factor

This is a summary of Ref. 1 which explains the changing leverage factor α for the suspended bilayer graphene of chapter 5 and Ref. 2. In Fig. B.1 we show the relation between α and the applied magnetic field. We have obtained from Fig. 5.3 the minima for the the filling factors ν and calculated the leverage factor by calculating $\alpha = \nu \cdot \frac{eB}{h}$ (see inset figure B.1). The leverage factor of the sample increases from the geometrical value 0.5 $\times 10^{14}$ m^{-2} V $^{-1}$ up to 1.8 $\times 10^{14}$ m^{-2} V $^{-1}$ at 9 T and saturates at this value for the highest fields. This effect is also observed implicitly in recent publications[3,4] on high quality suspended bilayer devices, but not mentioned by authors in the text.

As discussed in Ref. 1 the increase in capacitance of the system under the applied magnetic field could be understood from the deviation from the flat-plate capacitor model. At the point when the width of the graphene flake is smaller or comparable to the distance to the back gate the flat-plate capacitor model can no longer be applied. The charge carrier distribution in graphene becomes non homogenous and increases at the edges. Since the classical cyclotron radius d_p of the charge carrier depends inversely on the magnetic field, the increase of B will cause edge channels in the quantum Hall regime to propagate closer to the edge, where the density can be a few times higher than in bulk graphene; this leads to an increase of the capacitance value. In figure B.2 we show the calculated α_p for the minima of all filling factors for fixed fields in the range 1..30 T as a function of the cyclotron radius d_p. In case of a homogenous charge distribution it would follow the fixed value α_0, while for our suspended sample it follows the model described in Ref. 1 (represented by the dashed line).

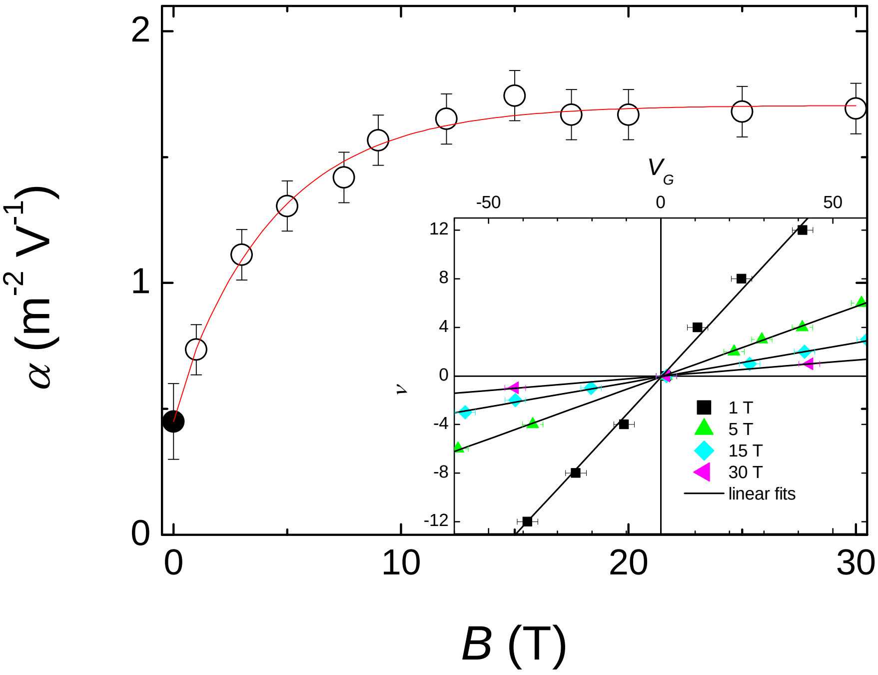

Figure B.1: *Relation between the induced charge carrier concentration per applied magnetic field $\alpha(B) = n/B$ and the applied magnetic field B for B=0 (●) and $B \neq 0$ (○). The plotted line shows the interpolated $\alpha(B)$ from which we determined a reliable value of the concentration n. inset: the position of the minima in V_G as a function of the filling factor ν for fixed fields. The linear line corresponds to the extracted leverage factor α.*

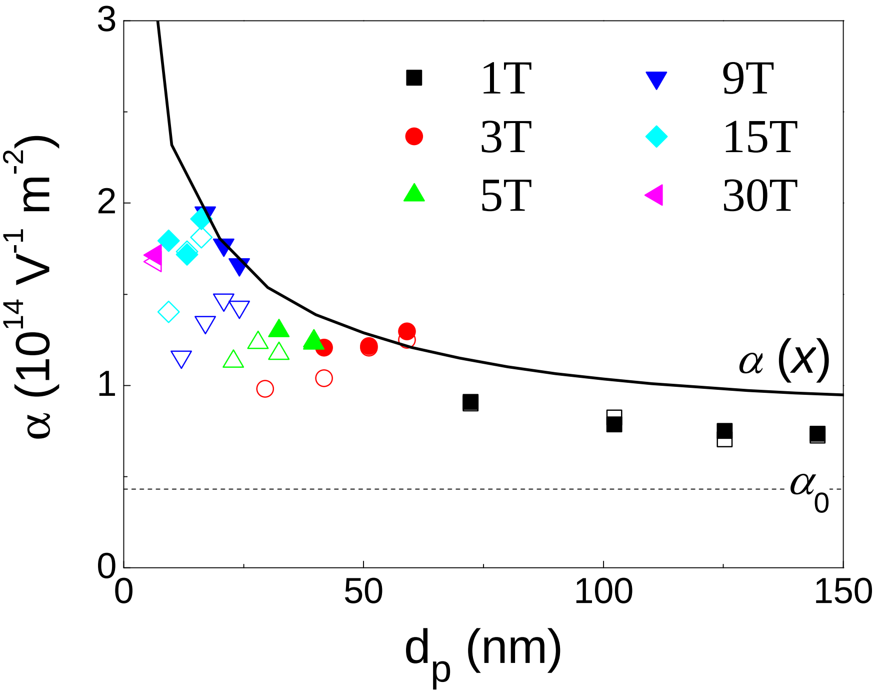

Figure B.2: *Capacitance profile near the edges of a high quality suspended bilayer graphene 2.6 μm long, 0.4 μm wide, with a gate dielectric of 500 nm SiO_2 plus 1.15 μm vacuum. Symbols correspond to the experimental capacitance of the individual plateaus α_P versus d_P. Filled symbols are for hole transport, open symbols are for electron transport. The dashed line shows α_0, the leverage factor for a simple parallel plate capacitor. The solid line shows the calculated $\alpha_P(x)$ from a three-dimensional electrostatic model, averaged along the length of the graphene.*

References

[1] I. J. Vera-Marun, P. J. Zomer, A. Veligura, M. H. D. Guimaraes, L. Visser, N. Tombros, H. J. van Elferen, U. Zeitler, and B. J. van Wees, "Quantum Hall transport as a probe of capacitance profile at graphene edges", *arXiv:1112.5462v1* (2011).

[2] H. J. van Elferen, A. Veligura, E. V. Kurganova, U. Zeitler, J. C. Maan, N. Tombros, I. J. Vera-Marun, and B. J. van Wees, "Field-induced quantum Hall ferromagnetism in suspended bilayer graphene", *Physical Review B* **85**, 115408 (2012).

[3] B. E. Feldman, J. Martin, and A. Yacoby, "Broken-symmetry states and divergent resistance in suspended bilayer graphene", *Nature Physics* **5**, 889–893 (2009).

[4] F. Freitag, J. Trbovic, M. Weiss, and C. Schonenberger, "Spontaneously Gapped Ground State in Suspended Bilayer Graphene", *Physical Review Letters* **108**, 076602 (2012).

Summary

This thesis presents magneto-transport experiments on mono-, bi-, and tri-layer graphene. In particular the peculiar properties of the lowest, zero-energy, Landau level are addressed.

This thesis begins with an introductory chapter 2 to the electronic properties of mono-, and bi-layer graphene. In particular we have shown that electrons in graphene behave as massless particles and obey relativistic physics. Additional to that we have shown that for the addition of a second layer, forming bilayer graphene, the electrons become massive. In both mono-, and bi-layer graphene the application of a magnetic field leads to the formation of discrete energies, the Landau levels. For the electrical transport this means that both materials exhibit a quantum Hall effect. For monolayer graphene we find a quantum Hall effect that shows four-fold degenerated lowest Landau level, while the extra degree of freedom in bilayer graphene (the extra layer) leads to an eight-fold degenerated lowest Landau level.

Subsequently in chapter 3 we have shown the general procedure for our sample preparation. We describe all lithography steps to connect electrically graphene-samples and subsequently test its electronic quality. With use of the backgate we induce capacitively charge carriers, i.e. for a positive (negative) voltage we induce electrons (holes) in the graphene. We show a decreasing resistance for increasing charge carrier concentration where the resistance decrease strongly depends on the electronic quality, i.e. the change of the resistance is directly proportional to the mobility of the charge carriers. This sample mobility is limited by the scattering of the charge carriers caused by substrate defects, surface impurities, etc. We describe techniques for further improvement of the sample mobility, e.g. reducing the number of surface impurities, and fully suspend the sample between the contacts by removing partially the substrate underneath the sample.

In chapter 4 we investigate the behavior of the Hall resistivity ρ_{xy} of monolayer graphene in the classical regime. Here ρ_{xy} makes a smooth zero crossing near zero charge carrier concentration, the charge neutrality point (CNP). This smooth transition is attributed to the co-existence of both holes and electrons near the CNP, meaning that below (above) the CNP there is still a finite amount of electrons (holes) participating in the transport. Taking into account the presence of both charge carriers above and below the CNP contributes to a better understanding of the unique nature of electronic states at zero energy level in graphene.

In chapters 5 and 6 we draw our attention to the lowest Landau level of bilayer graphene. In particular we explore the nature of the eight-fold degenerated lowest Landau level by applying high magnetic fields to high quality suspended bilayer graphene samples. We have shown that we can trigger different groundstates in bilayer graphene, showing either an ungapped groundstate (chapter 5), or a gapped groundstate (chapter 6).
In particular we have shown in chapter 5 that the eight-fold degenerated lowest Landau level breaks up into two four-fold degenerated energy levels, and displays a field-induced insulating character at the CNP. We attribute the field induced gap to an exchange driven mechanism of the bare Zeeman-gap.
In chapter 6 we investigate a bilayer graphene sample which shows a gap already for zero magnetic field, indicating two separated energy-levels at non-zero charge carrier concentration. The application of a magnetic field leads to the formation of Landau levels in the two separated energy levels. Breaking of the spin-degeneracy in the two individual energy levels leads to a reduction the gap at the CNP.

Finally in chapter 7 we present experiments on trilayer graphene. The experiments have shown a twelve-fold degenerated zero energy level, which break up in twelve individual energy levels by applying high magnetic fields. We do detailed study on the oscillatory behavior of the magnetoresistance in order to determine the hierarchial order of the degenerated energy levels. Additionally, we discuss the field-induced insulating character of the resistance at the CNP; experiments in tilted magnetic fields are used to decouple the effect of bare spin-effects and interaction driven mechanisms.

Samenvatting

Dit proefschrift presenteert magneto-transport experimenten aan enkel-, dubbel-, en drie-laags grafeen. In het bijzonder wordt de aandacht gevestigd op het laagste, nul-energie, Landau niveau.

Dit proefschrift begint met een introducerend hoofdstuk 2 met een beschouwing van de elektronische eigenschappen van enkel- en dubbellaags grafeen. In het bijzonder tonen we aan dat de ladingsdragers in grafeen zich gedragen als massaloze deeltjes die in het framework van de relativistische fysica worden beschreven. Daarnaast laten we zien dat als we twee grafeenlagen stapelen, dubbellaags grafeen, de ladingsdragers een eindige massa hebben. In zowel enkel- als dubbellaags grafeen zorgt een aangelegd magnetisch veld voor vorming van discrete energie-niveaus, de zogenaamde Landau niveaus. Het gevolg is dat elektronische geleiding wordt gekwantiseerd, het zogenaamde quantum Hall effect. Voor enkellaags grafeen is het laagste Landau niveau viervoudig ontaard, terwijl de extra vrijheidsgraad voor dubbellaags grafeen (de extra laag) leidt tot een achtvoudige ontaarding van het laagste Landau niveau.

Vervolgens beschrijven we in hoofdstuk 3 het algemene proces hoe we onze samples hebben geprepareerd. We beschrijven alle lithografische stappen om samples elektrisch te contacteren en deze samples vervolgens te testen op hun elektronische kwaliteit. Met behulp van een backgate induceren we capacitief ladingsdragers in het grafeen, d.w.z. met een positieve (negatieve) gate-spanning induceren we extra elektronen (gaten) in het grafeen. We laten zien dat de weerstand afneemt als de concentratie van ladingsdragers wordt vergroot, dit betekent dat er een directe relatie is tussen de weerstand en de mobiliteit van de ladingsdragers. De sample mobiliteit is gelimiteerd bij verstrooiing van de ladingsdragers, veroorzaakt door oneffenheden in het oppervlak, verontreinigingen aan het oppervlak, etc. We beschrijven technieken voor de verdere verbetering van de sample mobiliteit, d.w.z. een vermindering van het aantal verontreinigingen, en het volledig vrij hangen van het grafeen tussen twee contacten door middel van het gedeeltelijk verwijderen van het substraat onder het sample.

In hoofdstuk 4 onderzoeken we het gedrag van de soortelijke Hall weerstand ρ_{xy} in enkellaags grafeen in het klassieke regime. Hier doorkruist ρ_{xy} de nul-waarde nabij nul concentratie, het charge neutrality point (CNP). Deze geleidelijke overgang is uitgelegd met de gelijktijdige aanwezigheid van elektronen en gaten nabij het CNP, wat betekent dat onder (boven) het CNP er nog een eindige hoeveelheid elektronen (gaten) bijdraagt aan de elektronische geleiding. De beschrijving van de gelijktijdige aanwezigheid van beide ladingsdragers boven en onder het CNP geeft een beter begrip van de unieke elektronische toestanden in het laagste Landau niveau van grafeen.

In hoofdstukken 5 en 6 vestigen we onze aandacht op het laagste landau niveau in dubbellaags grafeen. In het bijzonder gebruiken we hoge magneetvelden om een beter begrip te krijgen van de achtvoudige ontaarding in het laagste Landau niveau. We hebben laten zien dat dubbellaags grafeen verschillende grondtoestanden heeft bij nul magneetveld; een toestand zonder gap (hoofdstuk 5) en een toestand met gap tussen de valentie- en geleidingsband (hoofdstuk 6).
In het bijzonder hebben we in hoofdstuk 5 laten zien dat in een aangelegd magnetisch veld de achtvoudige ontaarding in het laagste Landau niveau splitst in twee viervoudige ontaarde niveaus. Deze opsplitsing hebben we uitgelegd met behulp van de Zeeman-splitting versterkt door uitwisseling-energie tussen de elektronen.
In hoofdstuk 6 hebben we een dubbellaags grafeen sample onderzocht dat al bij nul magneetveld een gap heeft, ofwel twee gesplitste energieniveaus nabij het CNP. Het aanleggen van een magnetisch veld leidt tot de vorming van Landau niveaus, en in het bijzonder leidt dit tot een situatie waarin de Zeeman-splitsing in beide energieniveaus zorgt voor een verkleining van het gap op het CNP.

Ten slotte presenteren we in hoofdstuk 7 experimenten aan drie-laags grafeen. De experimenten tonen aan dat het laagste Landau niveau van drielaags grafeen twaalfvoudig is ontaard. Het aanleggen van hoge magneetvelden leidt tot de opsplitsing in twaalf individuele energieniveaus. We hebben gedetailleerd onderzoek gedaan naar de magneto-weerstand oscillaties om een hierarchie van deze opsplitsing te bepalen. Daarnaast hebben we in meer detail gekeken naar het isolerende karakter nabij het CNP. Experimenten in gedraaide magneetvelden zijn gebruikt om de effecten van pure spin- en interactie-effecten te onderscheiden.

List of Publications

1. H. J. van Elferen, A. Veligura et al., *Lifting of the degeneracy of the lowest Landau level of ABC-trilayer graphene* (in preparation).

2. A. Veligura, H. J. van Elferen, N. Tombros, J. C. Maan, U. Zeitler, B. J. van Wees, *Transport gap in suspended bilayer graphene at zero magnetic field*, Phys. Rev. B **85**, 155412 (2012).

3. H. J. van Elferen, A. Veligura, E. V. Kurganova, U. Zeitler, J. C. Maan, N. Tombros, I. J. Vera-Marun, B. J. van Wees, *Field induced quantum Hall ferromagnetism in bilayer graphene*, Phys. Rev. B **85**, 115408 (2012).

4. E. Kampert, H.J. van Elferen, F.F.B.J. Janssen, A.J.M. Giesbers, H. Engelkamp, P.C.M. Christianen, U. Zeitler, A.E. Rowan, J.C. Maan, *Discrete magnetization steps in an antiferromagnetically coupled Mn4 cluster* (submitted).

5. I. J. Vera-Marun, P. J. Zomer, A. Veligura, M. H. D. Guimares, L. Visser, N. Tombros, H. J. van Elferen, U. Zeitler, B. J. van Wees, *Quantum Hall transport as a probe of capacitance profile at graphene edges*, arXiv:1112.5462 (2011).

6. S. Wiedmann, H. J. van Elferen, E. V. Kurganova, M. I. Katsnelson, A. J .M. Giesbers, A. Veligura, B. J. van Wees, R. V. Gorbachev, K. S. Novoselov, J. C. Maan, U. Zeitler, *Coexistence of electron and hole transport in graphene*, Phys. Rev. B **84**, 115314 (2011).

7. E. V. Kurganova, H. J. van Elferen, A. McCollam, L. A. Ponomarenko, K. S. Novoselov, A. Veligura, B. J. van Wees, J. C. Maan, U. Zeitler, *Spin splitting in graphene studied by means of tilted magnetic-field experiments*, Phys. Rev. B **84**, 121407(R) (2011).

8. U. Zeitler, A. J. M. Giesbers, H. J. van Elferen, E. V. Kurganova, A. McCollam and J. C. Maan, *Magneto-transport in the zero-energy Landau*

level of single-layer and bilayer graphene, J. Phys.: Conf. Ser. **334**, 012035 (2011).

9. U. Zeitler, A. J. M. Giesbers, A. McCollam, E. V. Kurganova, H. J. van Elferen, and J .C. Maan, *High-field electronic properties of graphene*, J. Low. Temp. Phys. **159**, 238 (2010).

Curriculum Vitae

Henricus Johannes van Elferen, calling name: Erik, was born on the 2th of April 1985 in Nijmegen. He attended the secondary school Over Betuwe College in Bemmel, where he graduated with the profiles Nature&Health and Nature&Technology from the VWO in June 2003.
He studied physics at the Radboud University Nijmegen from 2003-2008. After graduating his propedeuse in August 2004, he successfully finished his Bachelor in August 2006 and his Master in Physics and Astronomy in August 2008. During the Master he did his graduation project on "Cantilever torque magnetometry" at the High Field Magnet Laboratory, in the group of Prof. dr. Ir. J.C. Maan.
After the graduation in August 2008, Erik started as a PhD researcher for FOM, settled at the High Field Magnet Laboratory. The main topic of research was on the magnetotransport properties of both substrate supported and suspended (multilayer) graphene at low temperatures and high magnetic fields. The results of this PhD are presented in this thesis.